



ISSN 1650-674X  
TRITA-ETS-2005-4  
ISRN KTH/R-0504-SE  
ISBN 91-7178-057-2

**KTH Electrical Engineering**

# **The Four-Quadrant Transducer System**

*for Hybrid Electric Vehicles*

**Erik Nordlund**

Div. of Electrical Machines and Power Electronics

Department of Electrical Engineering

KTH, Royal Institute of Technology

Stockholm 2005

Submitted to the School of Computer Science, Electrical Engineering and Engineering Physics, KTH, Royal Institute of Technology, in partial fulfilment of the requirements for the degree of Doctor of Technology

---

---

KTH, Royal Institute of Technology  
Department of Electrical Engineering  
Division of Electrical Machines and Power Electronics

KTH/ETS/EME  
Teknikringen 33  
SE-10044 Stockholm  
Sweden

© 2005, Erik Nordlund

---

---

## Sammanfattning

I denna doktorsavhandling presenteras ett nytt elhybridsystem för vägfordon benämnt fyrkvadrant omvandlare, "Four Quadrant Transducer (4QT)". Detta system har simulerats under körcykler som t ex FTP75 för att kunna bilda sig en uppfattning om bränsleförbrukningen för hybridsystemet och för att kunna dimensionera elmaskinerna till systemet. En elmaskinprototyp för hybridsystemet har konstruerats och provats i momentvåg.

Enligt utförda simuleringar blir besparingen i bränsleförbrukning ca 30% för en tolv tons distributionslastbil utrustad med en 100kW dieselmotor under körcykeln FTP75. Denna minskning av bränsleförbrukning kommer främst från en mera optimal kontroll av förbränningsmotorn samt regenerativ bromsning av fordonet.

Den konstruerade prototypen är avsedd för en medelstor bil. Anledningen till att prototypen inte byggdes i en storlek passande för distributionslastbilen var att prototypen skulle passa i testutrustningen i elmaskinlaboratoriet.

Prototypen provades i momentvåg för att undersöka verkningsgrad, förluster och termiska prestanda. Resultaten är enligt förväntningarna.

---



---

## **Abstract**

In this thesis a hybrid electrical powertrain called the Four Quadrant Transducer (4QT) has been evaluated through different driving simulations, which later resulted in the manufacture of a prototype.

The simulation of a 12 metric ton distribution truck showed that the 4QT system can reduce the fuel consumption by approximately 30 % during the FTP75 drive cycle. The reduction in fuel consumption is due to a more optimal control of the combustion engine and regenerative braking of the vehicle.

The prototype 4QT has been down scaled from the distribution truck size used in the simulations to a size suitable for a medium sized passenger car. This was done to fit the test rig in the electric machine laboratory.

The prototype was tested in the test bench to analyse performances such as efficiency, losses and thermal behaviour. These factors were investigated using both analytical models and the finite element method and later by measurements. The measured results were according to expectations.

---



---

## Acknowledgments

I would first like to thank my supervisor Chandur Sadarangani for making it possible for me to do my PhD at the department of Electrical Engineering.

During the years I had two different project leaders Dr. Thomas Bäckström and Dr. Peter Thelin and I would like to thank them for all the help given. I also thank Professor Sture Eriksson for his involvement in the project.

Thanks to Sven Karlsson, for help with the construction of the prototype, and to Karl-Erik Abrahamsson, Bertil Larsson, and Gösta Nilson for help with repairs and modifications of the prototype.

Thanks to Dr. Freddy Magnussen for the work presented in the thesis essential ideas and comments, and to Dr. Waqas Arshad, Maddalena Cirani (Tech. Lic.) and Mr Sylvain Châtelet my former colleagues that formed the hybrid group at EME for their contribution in creating a positive work environment.

I would like to thank my office mate Björn Allebrand for sharing the office with me for more than five years and for his participation in many discussions that covered a wide range of topics. I also extend thanks to the two "apprentices" Jörgen Hansson and Samer Shisha who have shared a small corner in the office for their daily contributions of entertainment.

Mr Jan Olov Brännvall and Mr Jan Timmerman are gratefully acknowledged for their help with everything concerning the workshop and lab, I am also grateful to Mrs. Eva Pettersson for her ability to always remember the project number.

Lic. Tech. Robert Chin is thanked for everything from training in the "KTH-Hallen" to the deep discussions in everything from the amazing technology of electrical machines to even more important issues, not mentioned here.

I would like to thank Lic. Tech. (probably Dr.) Karsten Kretshmar and Dr. Remy Kolessar for disco in the car and much more things not to be specified here.

I also would like to thank all the personal at the division of Electrical Machines and Power Electronics for their contribution in all forms.

Thank you to my brother in law Crafton Caruth for reading through the thesis and given valuable suggestions.

I would like to thank Dr. Micheal Lamperth, Mr. Alan Walker, Lic. Tech. Peethamparam Anpalahan, Mr. Sebastian Tsakok, Mr. Malte Jaensch and everyone else at the Imperial College for making my time there memorable.

I would finally like to thank my parents Alf and Kristina for support and my sisters Susanna and Elinor for everything they have done during the years. And my nephew Morgan for pooping on the floor of the lab.

*Erik Nordlund  
Stockholm, May 2005*

---





---

## Table of Contents

1. Introduction .....	5
1.1 <i>Outline of the Thesis</i> .....	5
1.2 <i>Published papers</i> .....	7
2. Vehicle drive train systems .....	9
2.1 <i>Conventional ICE engine vehicle</i> .....	9
2.2 <i>Series hybrid</i> .....	9
2.3 <i>Parallel Hybrid</i> .....	10
2.4 <i>Integrated Starter Generator (ISG)</i> .....	11
2.5 <i>The Integrated Energy Transducer</i> .....	12
2.6 <i>Fuel cell vehicles</i> .....	12
2.7 <i>Electric vehicles</i> .....	13
3. The 4QT System .....	15
3.1 <i>Operation of the 4QT</i> .....	17
3.2 <i>Output power of the 4QT</i> .....	20
3.3 <i>Different driving modes</i> .....	21
3.3.1 <i>Increased speed and torque</i> .....	21
3.3.2 <i>Decreased speed and increased torque</i> .....	22
3.3.3 <i>Decreased speed and torque</i> .....	22
3.3.4 <i>Increased speed and decreased torque</i> .....	23
3.3.5 <i>Pure electric mode</i> .....	24
3.4 <i>Different 4QT system layouts</i> .....	24
3.4.1 <i>Only final gear</i> .....	25
3.4.2 <i>Gear box between the 4QT and the final gear</i> .....	26
3.4.3 <i>Gear between the ICE and 4QT</i> .....	26
3.4.4 <i>Using the 4QT as a retarder</i> .....	27
3.5 <i>Conclusions</i> .....	28
4. Drive cycle simulations .....	29
4.1 <i>The target vehicle</i> .....	29
4.2 <i>The simulation program</i> .....	31
4.3 <i>The used drive cycle</i> .....	32
4.4 <i>Simulation results</i> .....	34
4.4.1 <i>Startability at 16% slope</i> .....	34
4.4.2 <i>Gradeability, 75km/h at 1.5% slope</i> .....	35
4.4.3 <i>Maximum speed 100km/h</i> .....	36
4.5 <i>FTP75 drive cycle analysis</i> .....	38
4.5.1 <i>Power demand during the FTP75/72 drive cycle</i> .....	39
4.5.2 <i>Fuel consumption simulations</i> .....	43
4.6 <i>Battery size versus ICE operation</i> .....	45
4.6.1 <i>The importance of recovering the braking energy</i> .....	46

---

---

4.7 Conclusion and results	48
5. The 4QT prototype design .....	49
5.1 Pole number	50
5.2 Analytic design	51
5.2.1 Basic design of the DRM	51
5.2.2 Calculation of the “DRM” magnet thickness	53
5.2.3 Basic design of the Stator	54
5.2.4 Calculation of the “Stator” magnet thickness	55
5.3 FEM investigation of the design	56
5.3.1 Magnetic airgap flux density	56
5.3.2 Back EMF	58
5.3.3 Cogging	61
5.3.4 Torque ripple	63
5.4 Inductances	65
5.5 Field weakening	67
5.6 Mechanical design	69
5.6.1 Bandage	69
5.7 Redesign after inner rotor failure	70
5.8 Cooling	71
5.9 Prototype layout	74
5.10 Conclusions from the prototype design	76
6. Prototype testing .....	77
6.1 Test setup for generator test	77
6.2 Placement of the measurement sensors	78
6.2.1 Water temperature sensors	78
6.2.2 Sensors in the 4QT	80
6.3 Generator tests	82
6.3.1 Stator test	82
6.3.2 DRM test	85
6.3.3 Combined tests Stator and DRM	87
6.4 No-load losses	89
6.4.1 Stator no-load losses	89
6.4.2 DRM no-load losses	90
6.5 Friction losses in the slipring units	90
6.6 Efficiency tests	91
6.6.1 Stator efficiency test	92
6.6.2 DRM efficiency test	93
6.7 Calorimetric measurements	95
6.8 Accuracy of the efficiency results	97
6.8.1 Calorimetric efficiency accuracy	98
6.9 Prototype parameters	99
6.9.1 Inductance measurements	99
6.9.2 Resistance measurements	100

---

---

6.10 Test of the new rotor winding	101
6.11 Conclusions	106
7. Thermal modelling .....	107
7.1 Lumped circuit modelling, steady-state	107
7.2 Results from the lumped circuit modelling	113
7.3 Different cooling options	114
7.3.1 New water cooling channels	115
7.3.2 Fluid cooling in the shaft	116
7.3.3 Air cooling of the rotor slot	117
7.3.4 Forced air cooling of the inner rotor	118
7.4 Thermal FE modelling	120
7.5 Conclusion	122
8. Losses in the 4QT .....	123
8.1 Resistive losses	123
8.2 Iron losses	124
8.2.1 Iron losses from an analytical model	124
8.2.2 Iron losses using FEM	125
8.3 Mechanical losses	127
8.4 Stray losses	130
8.5 Circulating currents in the windings	130
8.6 Measured and calculated losses	134
8.6.1 No Load	134
8.6.2 Load	135
8.7 Conclusions	136
9. Conclusion and future work .....	137
9.1 Conclusions	137
9.2 Future work	138
9.2.1 Drive system simulation of the 4QT system	138
9.2.2 The slipring-less double rotor machine	138
References .....	143
List of symbols and abbreviations .....	147
Index .....	149

---



# 1 Introduction

A combustion engine in a conventional vehicle operates rarely at optimum efficiency. The optimum efficiency is about 30–40 % and can only be obtained in a small speed-torque region. The mean efficiency is much lower because of the small maximum efficiency region. To operate a combustion engine at optimum efficiency during all driving conditions, full control of the torque and speed is required. In a series hybrid vehicle such control is achieved but the electric machines must be dimensioned for the maximum power and all energy has to be converted from mechanical to electric and back to mechanical with losses at every conversion stage. The parallel hybrid vehicle has a smaller electric motor that is mechanically connected to the gears, which limits the control of the internal combustion engine (ICE) to only the torque. In the novel four-quadrant transducer (4QT) concept [6], which is a further development of the work on the integrated energy transducer [3], the advantages of the series and parallel hybrid systems are combined. This gives possibilities to operate the ICE independent of the road load.

The 4QT system has been investigated with the help of simulations in Matlab/Simulink environment. The simulations showed a decrease of the fuel consumption of a twelve ton vehicle by 30 % running the FTP75 drive cycle. This decrease is due to the more efficient use of the ICE and the use of regenerative braking.

A prototype 4QT has been designed, manufactured and tested as a proof of the concept. The prototype was dimensioned for a small passenger car with a total power of approximately 60kW.

The main aspects of the 4QT prototype testing were the thermal issues and losses in the machine. Efficiency maps have been measured for the prototype to be used in further tests/simulations of the machine and to verify the calculations.

## 1.1 Outline of the Thesis

In this thesis the novel Four-Quadrant Transducer system is presented. Simulations of the system during different driving conditions have been carried out. The results of the simulations show the demands that must be made on the system in order to get the right performance. They also give important data that are required to dimension a 4QT system for a hybrid vehicle. A description of the 4QT prototype is also given.

The presented work has the following outline:

**Chapter 2:** Describes different hybrid vehicle topologies. Presents the series and

parallel hybrid systems, the integrated starter generator, the integrated energy transducer, fuel cell and electric vehicles. The basic operation principles, the advantages and disadvantages of the systems are presented.

**Chapter 3:** Gives an introduction to the Four Quadrant Transducer (4QT) system. The chapter presents the main idea of the system, the operation principles and the possibilities and limitations of the 4QT system.

**Chapter 4:** Presents details about the simulations of the 4QT system. Gives details about the simulation program used for the simulation, introduces the vehicle data for the target vehicle, presents the different driving demands for the vehicle and introduces the drive cycle used for the simulations. The results of the different simulations are presented as fuel consumption of the vehicle and torque and speed requirements of the 4QT machines.

**Chapter 5:** Deals with the design of the 4QT prototype. The design starts with a basic analytical design, which later is confirmed via FEM simulations. Magnetic air gap flux density, back EMF, cogging, torque ripple, inductances and the field weakening region are investigated with FEM for the prototype. The effect of skewing on the cogging and the torque ripple in the machine are investigated. The mechanical design and the cooling methods for the prototype are presented.

**Chapter 6:** Presents the measurements on the 4QT prototype. The test setup is presented for the different tests. The different parts of the 4QT such as the Stator machine (SM) and the Double Rotor Machine (DRM) has been investigated separately and together. The measurements present the thermal capabilities, losses and the efficiency of the 4QT prototype. The parameters such as inductance and resistance of the windings are measured and presented. The effect of the different design changes that has been performed during the work are analysed in the chapter.

**Chapter 7:** Presents the thermal modelling of the 4QT machine. The thermal modelling where done both with lumped circuit modelling and with FEM. The two different methods are presented and compared with measured results for steady-state operation. Different innovative cooling techniques are investigated and proposed for the 4QT system.

**Chapter 8.** Investigates the different losses in the 4QT prototype both analytically and with FEM. The losses has been compared to measured values and separated into different components, such as copper, iron and mechanical losses.

**Chapter 9.** Contains conclusions of the presented work and presents some possible future work. The chapter contains the main results from both the simulations and the prototype design, manufacturing and testing.

## 1.2 Published papers

The following papers have been published at international conferences as a part of this work. Paper 1 to 3 and 8 to 10 focus on the 4QT system. Paper 1-3 have the author of this thesis as main author. Paper 1 and 3 present the 4QT prototype design and manufacturing while paper 2 contributes with system simulations of the 4QT system. In paper 8-10 the thesis author has been lightly involved. These papers present the winding current distribution, how the skewed slot influences the performance, and inductance measurements and calculations of the 4QT prototype.

Paper 4 and 5 deal with sliprings and their operation, since they are an important part of the 4QT system. The papers contribute with slip ring operation at high speeds, high current densities and high inverter fed frequencies.

Paper 6 and 11 describe thermal modelling of electrical machines, Paper 6 describes the thermal modelling of an radial flux permanent magnet machine and paper 11 deals with the thermal modelling of an axial flux motor. This paper contributes with the modelling method used in chapter 7 for the 4QT prototype.

Paper 7 describes the two novel hybrid systems the Free-Piston Generator [47] and the 4QT system.

### 1. Four-quadrant Energy Transducer for Hybrid Electric Vehicles

E. Nordlund, C. Sadarangani and P. Thelin, Published in the Proceedings of the International Conference on Electrical Machines, ICEM 2002, Brugge, Belgium, August 2002

### 2. Four-quadrant Energy Transducer for Hybrid Electrical Vehicles Simulations and System Description

E. Nordlund and C. Sadarangani, Published in the Proceedings of the International Battery, Hybrid and Fuel Cell Electric Vehicle Symposium & Exhibition, EVS-19, Busan, Korea, October 2002

### 3. Four-quadrant Energy Transducer

E. Nordlund and C. Sadarangani, Published in the Proceedings of the 37th Industrial Application Society Meeting, IAS 2002, Pittsburgh, USA, October 2002

### 4. Testing of Silver-, Copper- and Electro-Graphite Brush Materials for Slip Ring Units

E. Nordlund, F. Magnussen, G. Bassilious and P. Thelin, Published in the Proceedings of the Nordic Workshop on Power and Industrial Electronics (NORpie), Trondheim, Norway, June 12-14, 2004

- 5. Measurements on Slip Ring Units for Characterization of Performance**  
F. Magnussen, E. Nordlund, S. Chatelet and C. Sadarangani, The Sixth International Power Engineering Conference (IPEC2003), Singapore, November 27 - 29, 2003
- 6. Thermal Analysis - Lumped Circuit Model and Finite Element Analysis**  
Y.K. Chin, E. Nordlund and D.A. Staton, The Sixth International Power Engineering Conference (IPEC2003), pp. 952 - 957, Singapore, November 27 - 29, 2003
- 7. New Drive Topologies for Hybrid Electric Vehicles**  
W. M. Arshad, E. Nordlund and P. Thelin, Published in the Proceedings of the ICEET03 International Conference on Electrical Engineering and Technology, Dar Es Salam, Tanzania, August 2003
- 8. Investigation of the Winding Current Distribution in a 4-Quadrant-Transducer Prototype Machine**  
P. Zheng, E. Nordlund, P. Thelin and C. Sadarangani Published in the Proceedings of the The Eleventh Biennial IEEE Conference on Electromagnetic Field Computation (CEFC2004), June 2004, Seoul, Korea
- 9. Consideration of Skewed Slots in the Performance Calculations of a Four-Quadrant Transducer**  
P. Zheng, P. Thelin, E. Nordlund, S. Eriksson and C. Sadarangani, Published in Proceedings of the IEEE Vehicular Power and Propulsion Symposium, VPP 04, Paris, France, October 6-8, 2004
- 10. Measurements and Calculations of Inductances of a 4QT Hybrid Electric Vehicle Prototype Machine**  
P. Zheng, P. Thelin, A. Chen and E. Nordlund, Published in Proceedings of the IEEE Vehicular Power and Propulsion Symposium, VPP 04, Paris, France, October 6-8, 2004
- 11. Lumped Circuit Model of an Axial Flux Motor**  
E. Nordlund, S. Tsakok, Published in the Proceedings of the 21st Worldwide Battery, Hybrid and Fuel Cell Electric Vehicle Symposium & Exhibition, EVS-21, Monaco, April 2-6, 2005



## 2 Vehicle drive train systems

A number of different hybrid and electric drive train systems are proposed and used worldwide. Some of them are presented in this chapter together with a brief introduction to the conventional combustion engine vehicle.

### 2.1 Conventional ICE engine vehicle

In a conventional vehicle the internal combustion engine (ICE) is directly connected to the wheels via the clutch and the gearbox shown in Figure 2.1. This means that for each gear the ICE has to follow the road load with both the torque and speed. Because of the small maximum efficiency region of a combustion engine, the operation is rarely at the maximum point; this gives a low efficiency of the complete drive train particularly in urban traffic.

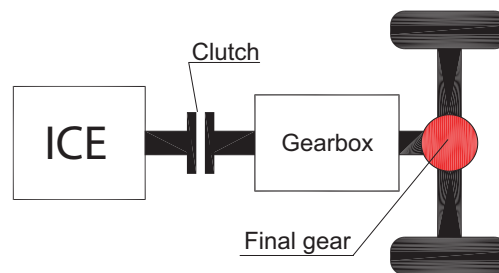


*Fig. 2.1 Conventional drive train with ICE, clutch, gearbox and final gear.*

### 2.2 Series hybrid

The series hybrid system consists of an ICE, a generator, two inverters, energy storage (for example a battery or capacitors) and a traction motor, as shown in Figure 2.2. In the series hybrid system the ICE is not mechanically coupled to the final gear, thereby making it possible to operate the ICE at optimal efficiency independent of the road load. The size of the battery is of great importance to the control flexibility of the ICE, a small battery requires a combustion engine control that follows the output power of the vehicle. If a large battery is used the combustion engine can operate more independently of the road load, because the battery acts as an energy storage that is used for transient power demands.

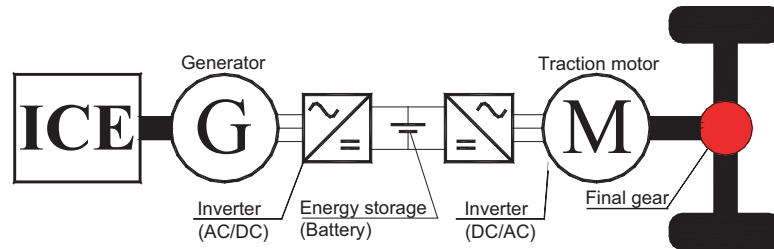


Fig. 2.2 The series hybrid system.

Some advantages and disadvantages of the series hybrid system are given below:

Advantages:

- Optimal control of the ICE.
- The ICE and the electric traction motor can be distributed in the vehicle which enable new vehicle layouts.
- The ICE does not have to be dimensioned for the maximum power.

Disadvantages:

- Several stages of energy conversions, result in more losses.
- The electrical drive system has to be dimensioned for maximum power.

## 2.3 Parallel Hybrid

A parallel hybrid system can be outlined in different ways. In the parallel system shown in Figure 2.3, the ICE is mechanically connected to the gearbox and thus to the wheels; this gives the possibility to control the torque but not the speed of the ICE independent of the road load. The electric power is fed in to the gearbox by a motor and drawn out of the gearbox by a separate generator. It is also possible to use only one electrical machine working as motor/generator and one inverter. There are a number of different ways to arrange the power split of the parallel hybrid vehicle, the case in Figure 2.3 uses a gearbox with three separate shafts. It can also be arranged with the motor/generator directly in line with the ICE as in Figure 2.4 where the ISG system is presented.

A list of the advantages and disadvantages of this system are given below:

Advantages:

- The electrical components are dimensioned for the power difference between the ICE and the final gear.
- Usually higher efficiency due to fewer energy conversions.

Disadvantages:

- The ICE can not work at an optimal operation point regarding both speed and torque.

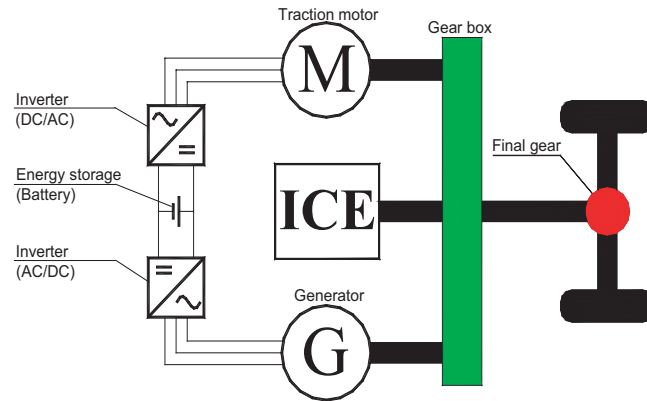


Fig. 2.3 The parallel hybrid system.

## 2.4 Integrated Starter Generator (ISG)

In the ISG system shown in Figure 2.4, the electric machine is small and only operates as a starter, generator and to boost the torque during acceleration. It is also possible to use the electric motor for regenerative braking. When the vehicle is at standstill the ICE is shut off. At take off the vehicle is moved from standstill by the electric motor and at certain speed or load demand, the ICE is started by the electrical motor. At higher speeds the vehicle performs as a conventional vehicle, with the electric machine working as generator. This system uses light electric components and a small battery.

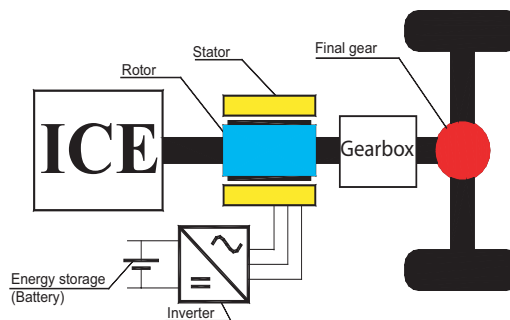


Fig. 2.4 The ISG system.

## 2.5 The Integrated Energy Transducer

In the integrated energy transducer (IET) system, [3], shown in Figure 2.5, the ICE is connected to a double rotor machine (DRM) that changes the speed to the optimal speed of the ICE while the torque is controlled with a continuous variable transmission (CVT). The combination of these two components opens up for an optimal control of the ICE. In the IET system the three-phase winding is rotating and sliprings are required to feed electric power to the windings. The DRM is dimensioned for the speed difference between the required output speed from the IET and the optimal speed of the ICE, and for the maximum ICE torque.

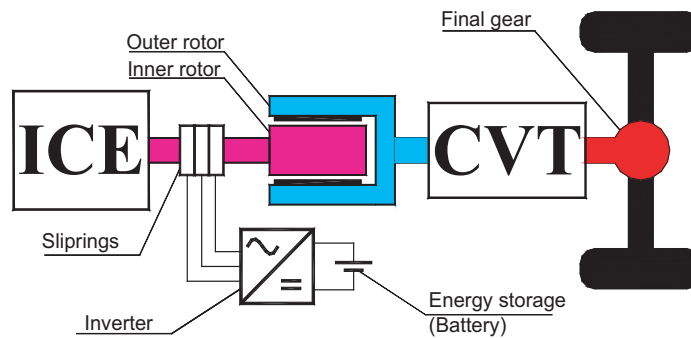


Fig. 2.5 The IET system.

## 2.6 Fuel cell vehicles

A fuel cell (FC) vehicle uses fuel cells and not a combustion engine as the primary energy source. The fuel cell uses for example hydrogen or methanol as fuel and produces electricity through a chemical conversion of the fuel. This is a clean process, in the case of hydrogen fuel the only emission from the FC is water. Even though the production of the hydrogen is not always a clean process. The challenges lie in cost reduction and the method to store hydrogen in a safe and a compact way. To avoid the latter, a reformer that refines the hydrogen from the methanol before it is used in the FC can be used.

In the real FC system a battery or some other energy storage device, e.g. a super capacitor, is often included to enable the vehicle to start faster and to achieve a higher peak power and better transient performance.

The FC is more efficient than the ICE. As a comparison the tank to wheel efficiency of a FC-vehicle is almost 50%, whereas the same efficiency for an ICE vehicle is about 15% [5].

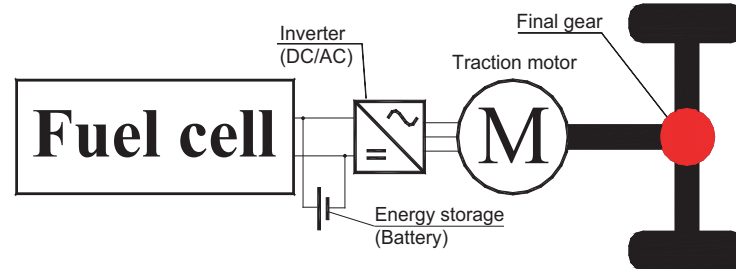


Fig. 2.6 The fuel cell system.

## 2.7 Electric vehicles

The electric vehicle (EV), Figure 2.7, has an electric machine that operates mostly as a traction motor but in some cases as a generator when utilizing regenerative braking. The energy to the electric machine comes in most cases from batteries that have to be charged from an external source. However, the emissions from the electric vehicle is zero. It must be remembered that the electricity required for charging of the vehicle can be produced in different ways with different levels of emissions. A serious problem with electric vehicles is the battery performance, both the power and the energy of the battery limit the vehicle performance and the driving range. Presently there are many different batteries on the market with varied power and energy capability.

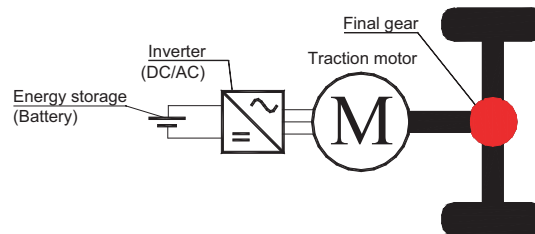


Fig. 2.7 Electric vehicle drive train.

Table 2.1 shows the energy density of different battery types and of gasoline and diesel. The huge difference between the liquid fuels and the batteries shows that the battery powered vehicles have a much lower driving range compared to a conventional vehicle. As can be seen from the Table 2.1 the energy density is about 80 times higher for gasoline than for the best battery, the Li-ion battery. The efficiency of the battery drive is higher than for a combustion engine, but if one for example assumes that the combustion engine drive has an efficiency of

20% and the battery drive 100%, the battery still has to be 16times heavier than the gasoline tank. In a conventional car the fuel tank is about 50litres which is approximately 37kg of fuel. A Li-ion battery then has to be 16times heavier, i.e. 590kg to have the same driving range as a conventional car with a 50litre fuel tank. This is for a conventional car that weighs about 1500kg. If one then adds 590kg of battery, the weight and consequently the energy consumption of the car will increase. Another aspect is the charging of the battery. To fuel 50litres of gasoline takes some minutes whereas to fully charge a battery of 590kg requires 307MJ of energy, which means that a power of 1MW would be required to fully charge the battery in 5 minutes.

However, in the most common cases a driver does not drive more than about 50km a day, e.g. to and from work. In this case an electric car that is charged during night could be a suitable alternative.

*Table 2.1 Energy density of different energy sources.*

Type of energy storage	Energy density [MJ/kg]	Reference
Lead-acid	0.144	[2]
Metal hydrid	0.28	[2]
Li-ion	0.52	Saft corporation data sheet
Diesel	42.5	[2]
Premium Gasoline	43.5	[2]

### 3 The 4QT System

The 4QT system [6] consists of, as shown in Figure 3.1, one ICE, two inverters, a battery and the four-quadrant transducer (4QT) which includes the sliprings. The 4QT transducer is an electric machine made up of two combined electric machines, in this case radial flux permanent magnet synchronous machines. The 4QT consists of one double rotor machine (DRM) and one conventional machine (Stator). The 4QT can replace the gearbox, clutch, and the flywheel in the vehicle but instead it needs a battery, two inverters and some control equipment. The DRM consists of the inner rotor with windings fed through the sliprings and the outer rotor with magnets. The Stator is a conventional stator with windings that interacts with the outer rotor of the DRM. The magnets on the outer rotor are separated into one inner layer for the DRM and one outer layer for the Stator as shown in Figure 3.1.

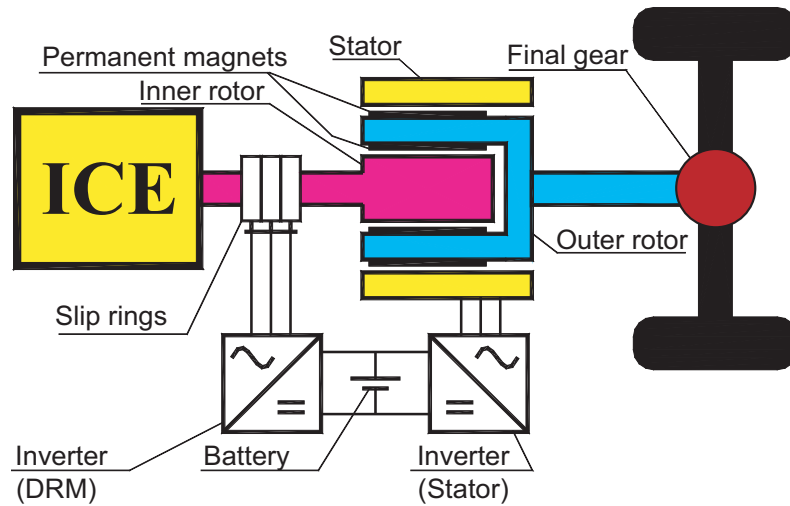


Fig. 3.1 The 4QT system.

Both machines are supposed to work both as motors and as generators. The 4QT is mounted between the combustion engine and the final gear in a hybrid electric vehicle (Figure 3.1). The function of the 4QT system is to keep the operation of the ICE at maximum efficiency (Figure 3.2) during all driving conditions to minimize fuel consumption. The 4QT changes both the speed and torque produced by the ICE at the optimal operation point to the required speed and torque at the final gear. The DRM either increases or decreases the speed from the ICE to the speed required at the final gear. The Stator increases or decreases the torque produced by the ICE to match the demanded torque at the final gear. This enables operation at maximum efficiency and/or minimum emission of the ICE at all speeds and loads of the vehicle. It is also possible to drive the 4QT-equipped vehicle in a pure electric mode.

During this mode the driving range is then limited by the energy content of the battery. If the battery is removed the 4QT system can be operated as an electrical variable transmission system [42].

As shown in Figure 3.2 the ICE efficiency is highest at high torques and at mid range speeds (2000-3000rpm) for this specific diesel engine. The optimal operation line (OOL) is the operation line where the ICE operates at optimal efficiency for a required power, and it is almost the same as the maximum torque limit for all speeds. The maximum torque and the OOL are shown in Figure 3.2 as a solid line for the maximum torque and a dotted line for the OOL. The OOL is used to obtain the maximum efficiency of the ICE. To obtain the lowest possible emissions the transient behaviour of the ICE must also be considered. An estimation of the emissions has not been made since no reliable emission data for the combustion engine was available.

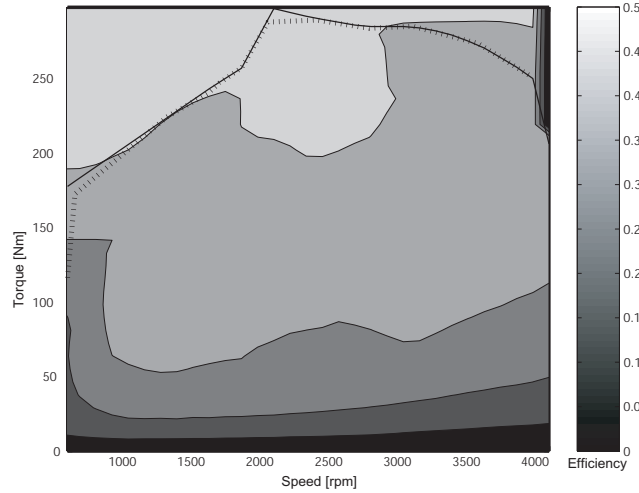


Fig. 3.2 ICE efficiency versus speed and torque. The solid line is the maximum torque and the dotted is the optimal efficiency line used in the simulations.

To keep the ICE operation along the OOL the 4QT changes the speed and torque required at the final gear to the speed and torque along the OOL for the ICE. an example of how the 4QT moves the operation point is shown in Figure 3.3. The required speed and torque at the final gear can be higher or lower than the OOL. In Figure 3.3 point A is the required torque and speed at the final gear. Point B is the equivalent operation point on the OOL of the ICE that produces the same power as required at point A plus the losses in the system, battery charging/discharging and the auxiliary power load of the vehicle. The DRM changes the speed by  $\Delta n$  from the speed required at the final gear to the optimal speed of the ICE. In the same



manner the torque is changed by  $\Delta T$  with the Stator to the optimal torque for the required power. This movement of the operation point maintains the operation of the ICE at the OOL during all driving conditions. The 4QT is dimensioned for the difference in speed and torque between the ICE and the final gear, which gives smaller electrical machines than in a series hybrid vehicle, meanwhile a full control of the ICE operation is possible. It is also possible to use a smaller ICE than in a conventional vehicle, this because of that the highest peak powers can be supplied by the electrical machines via the battery instead of directly from the ICE. This gives a ICE dimensioned after the highest continuous power, usually the top speed of the vehicle, instead of the highest peak power, usually during hard accelerations.

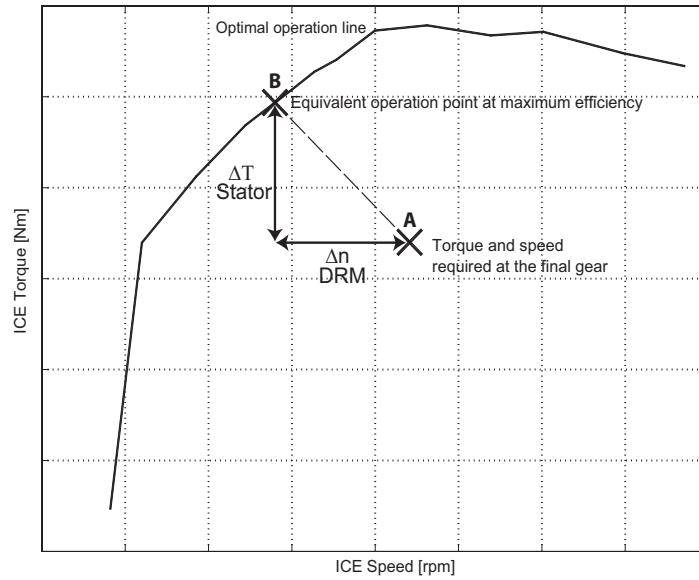


Fig. 3.3 The 4QT torque and speed changing strategy.

### 3.1 Operation of the 4QT

Simulating a twelve-ton truck during the first 140 seconds of the FTP75 drive cycle clearly demonstrates the operation of the 4QT. Figure 3.4 shows the vehicle speed and the speed and torque required at the final gear during the first 140 seconds of the FTP75 drive cycle. The final gear speed in Figure 3.4 is the vehicle speed in km/h converted by the wheel radius and the constant final gear ratio into the speed in rpm of the final gear input shaft. During this period the torque production in the ICE, DRM and Stator are shown in Figure 3.5. Here it can clearly be seen that the ICE and DRM torques are the same because the DRM only changes the speed and trans-

fers the ICE torque unchanged. The Stator either increases or decreases the torque so it matches the torque required at the final gear. In Figure 3.5 the Stator torque reaches very large negative values. In these cases both regenerative braking and conventional braking must be used.

Figure 3.6 shows the speeds in rpm of the ICE, the inner rotor and the outer rotor. The DRM speed is the difference between the ICE speed and the speed at the final gear. The speed of the DRM can also be negative, even when the vehicle is moving forward. This can be mostly seen at low speeds when the optimal speed of the ICE is higher than that required at the final gear.

As can be seen in figures 3.4-3.6, for a vehicle equipped with a 4QT system the ICE should be dimensioned for the mean power consumption and the 4QT for the difference between the mean and the peak power. The 4QT allows an optimal control of the ICE by changing the speed and the torque using the DRM and the Stator.

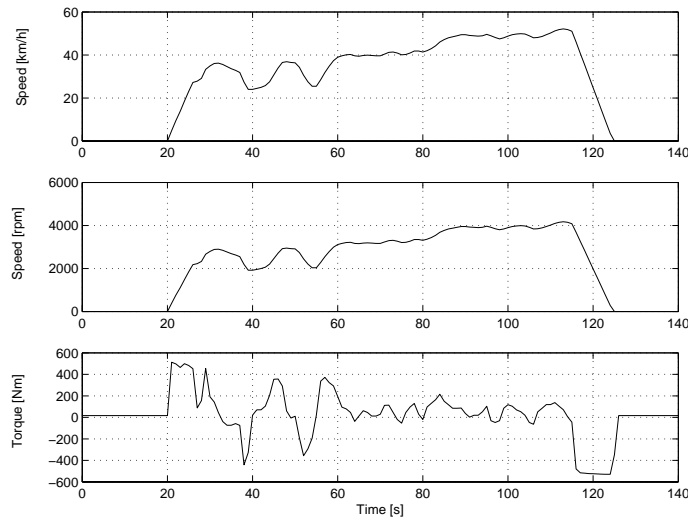


Fig. 3.4 Vehicle cruising speed, speed and torque at the final gear during the first 140 seconds of the FTP75 drive cycle.

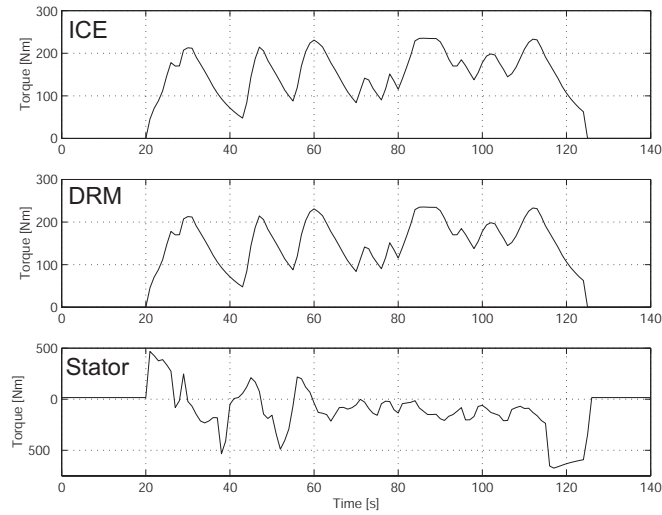


Fig. 3.5 ICE, DRM and Stator torques during the first 140seconds of the FTP75 drive cycle.

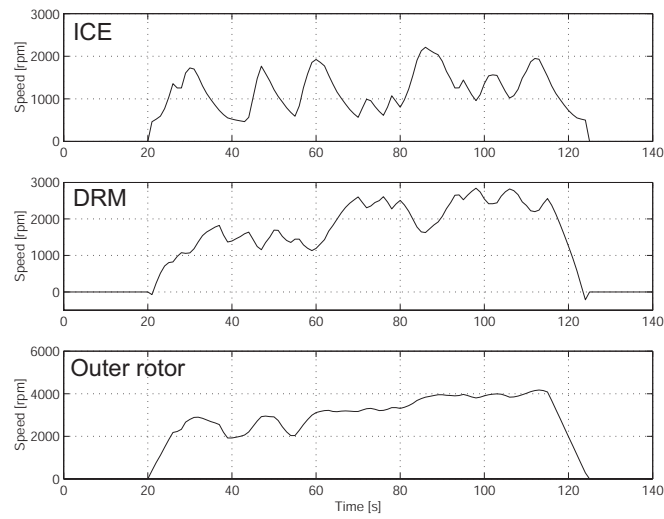


Fig. 3.6 ICE, DRM and outer rotor speed during the first 140seconds of the FTP75 drive cycle.

## 3.2 Output power of the 4QT

The output torque of the 4QT system is a combination of the ICE (or DRM) and the Stator torques shown in Figure 3.7. To derive the total output torque the Stator and ICE torques are added together. The output speed of the system is obtained by adding the DRM speed to the ICE speed.

So the maximum torque output is the maximum ICE torque plus the maximum stator torque while the maximum output speed of the system is the maximum ICE speed plus the maximum DRM speed.

The maximum power output that is possible to deliver from the 4QT system is different for transient and steady-state conditions. At transient conditions the maximum output power, when neglecting all losses, is the ICE power plus the battery power assuming the inverters are dimensioned for this. At steady-state condition the maximum output power becomes the same as the maximum ICE power. When running for a long time at a high power the battery gets discharged and thus only the ICE power can be used during longer time periods.

The operation point at the output shaft in Figure 3.7 can be deduced starting from the ICE operation point, then adding first the speed increase from the DRM, and then finally the torque increase from the Stator. This point is a transient operation point since both the speed and torque increases need extra energy from the battery.

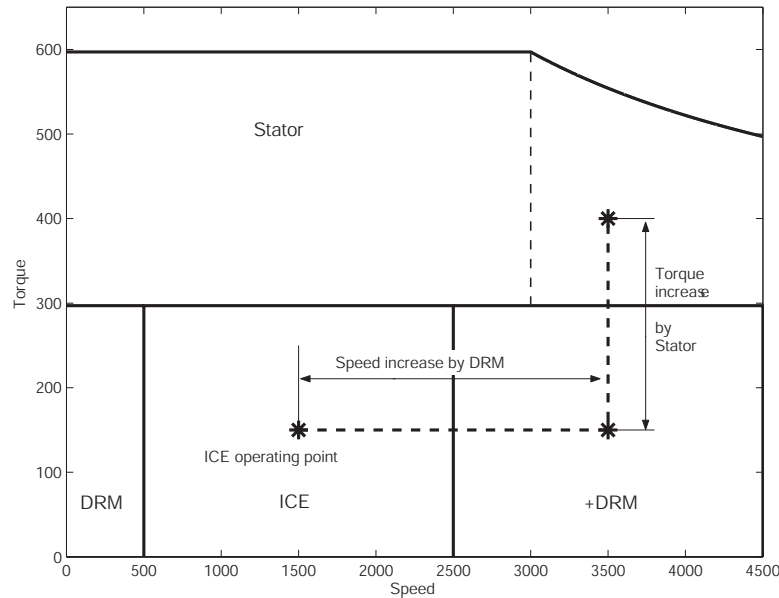


Fig. 3.7 Output torque versus speed for the 4QT system.

### 3.3 Different driving modes

The 4QT system obtained its name from the four different operating modes described in the following. Looking at a speed-torque diagram the 4QT can operate in all four quadrants modes defined with the origin at the operating point of the ICE.

These four modes can be described as:

- Increased speed and torque: The 4QT draws power from the battery under heavy load, both machines require power from the battery.
- Decreased speed and increased torque: The DRM decreases the speed and the Stator increases the torque. The DRM charges and the Stator discharges the battery.
- Decreased speed and torque: The DRM decreases the speed and the Stator the torque. Both machines are charging the battery.
- Increased speed and decreased torque: The DRM increases the speed and the Stator decreases the torque. The DRM discharges and the stator charges the battery.

All four modes will be further described in this chapter.

#### 3.3.1 Increased speed and torque

In this mode, shown in Figure 3.8, both the speed and the torque are increased by the 4QT from the ICE to the final gear. This mode is for example used when the vehicle is operating at high speed and is accelerated. Figure 3.8 shows the power flow in the system. The power flows from the battery to both machines which leads to a decrease of the battery SOC (State of Charge), so this mode of operation is time limited by the battery energy content or by the lowest allowed SOC level.

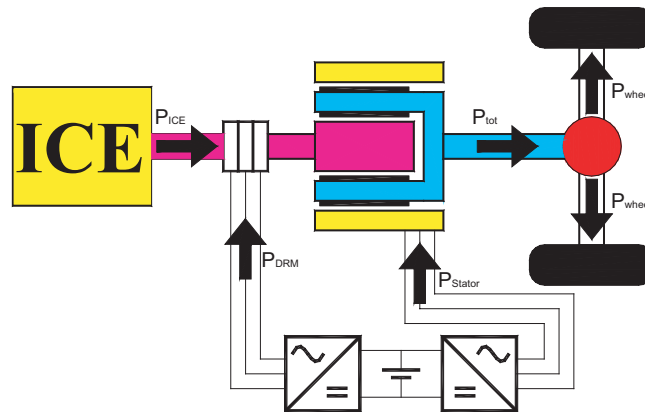


Fig. 3.8 Increased speed and torque.

### 3.3.2 Decreased speed and increased torque

In this mode, shown in Figure 3.9, the DRM decreases the speed of the ICE and operates as a generator, feeding power to the Stator and/or the battery. The Stator increases the torque from the ICE torque to the required torque at the final gear. The Stator gets power from the DRM and/or the battery. If this mode is used for a longer period of time all power used by the Stator must be produced by the DRM. This mode is used when the vehicle is driving at low speed and heavy loads, at start from standstill and when the optimal operation of the ICE is at a higher speed than the required speed at the final gear.

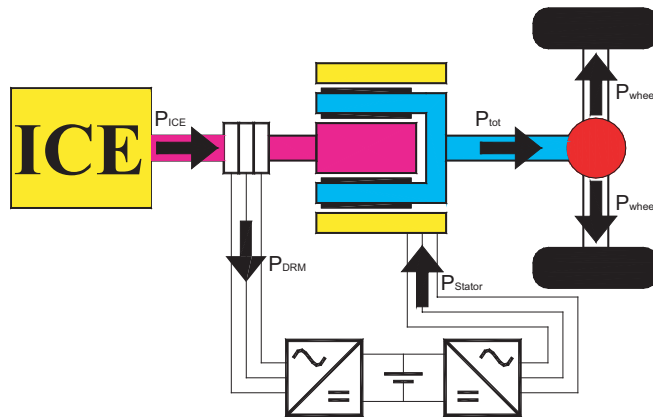


Fig. 3.9 Decreased speed and increased torque.

### 3.3.3 Decreased speed and torque

If the SOC in the battery is low and the battery needs immediate charging both the DRM and the Stator can operate as generators simultaneously. In this case the ICE is working with a higher speed and torque than what is required at the final gear. The DRM decreases the speed and feeds power to the battery via one inverter, the Stator decreases the torque and charges the battery with power via the other inverter. Figure 3.10 shows the power flow during this mode of operation. The ICE power is in this case the required power at the final gear plus power delivered to the battery through the DRM and the Stator. This mode is used at transient condition to charge the battery quickly and the charging power to the battery has to be considered since the battery has a maximum input power limit. It is also used in case of regenerative braking of the vehicle when either braking with the Stator or the DRM or both together.

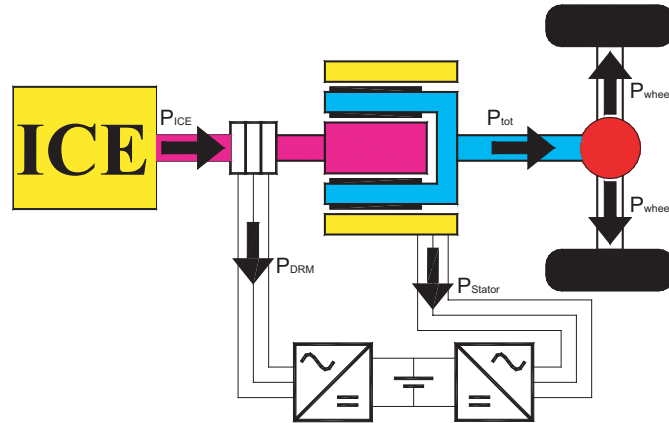


Fig. 3.10 Decreased speed and torque.

### 3.3.4 Increased speed and decreased torque

The most common driving mode is increased speed and decreased torque, see Figure 3.11. This is because the ICE optimal operation is located at relatively low to moderate speeds but at high torques. During this mode the DRM takes power from the battery or from the Stator, that operates as a generator, and increases the speed. The Stator, which operates as a generator, decreases the torque. This driving mode gives at first sight the impression of a loop in the power flow, which is in fact true but the circulating power is very low compared to the power that flows straight through the system. As an example the circulating power is only 5 % of the final gear power in simulations when driving a 12-ton vehicle at 100km/h on a flat road.

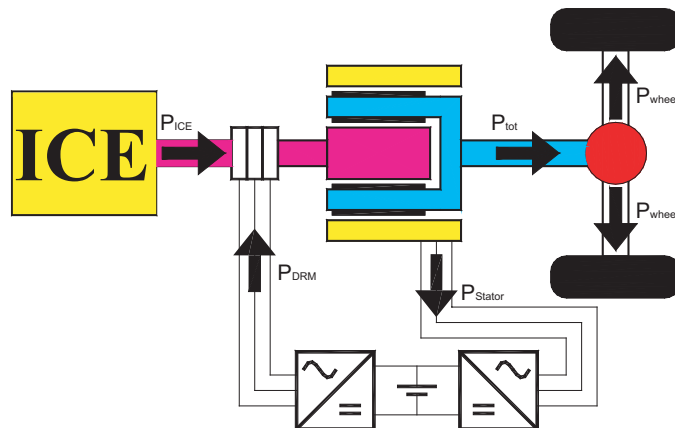


Fig. 3.11 Increased speed and decreased torque.

### 3.3.5 Pure electric mode

There is in fact a fifth mode of operation, the pure electric mode, shown in Figure 3.12. In this mode the power from the battery is consumed by the two machines of the 4QT. When operating the DRM in the pure electric mode the torque that is produced by the DRM is also acting on the ICE shaft. This could lead to a situation where the ICE may start to rotate in the opposite direction to the normal operation because of the DRM torque. To avoid this reverse rotation a lock-up function of the ICE shaft is required when the DRM is operating in pure electric mode. In order to minimize the cost of the system this lock-up function should preferably be avoided as it adds one more component to the system thereby increasing the cost and complexity of the system.

It is possible to avoid this lock-up function if only the Stator is used during pure electric mode operation. The drawback with this is that the electric performance becomes limited to the Stator power. Overall, this is considered as a minor problem since the pure electric mode is mostly utilized at low speed and low power of the vehicle. The electrical power is also limited by the battery power and using both machines in pure electric mode requires a battery with both high power and high energy capacities.

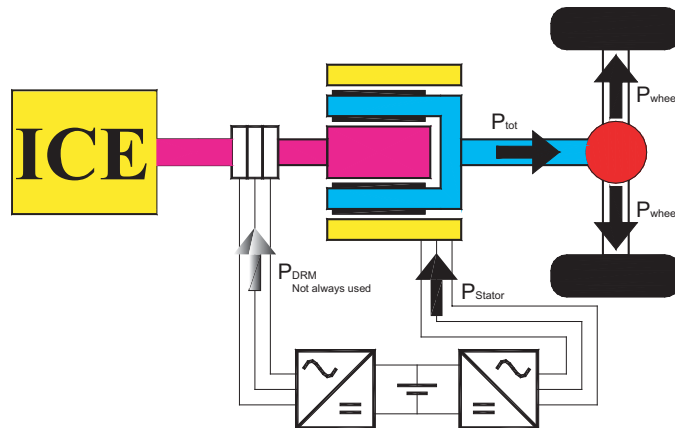


Fig. 3.12 Pure electric driving of the 4QT vehicle.

## 3.4 Different 4QT system layouts

It is possible to combine the 4QT with the ICE and final gear in a number of different configurations. It is also possible to arrange the drive train with gears before and after the 4QT.



When using the functional requirements [31] the maximum wheel torque starting requirement is approximately 9.5kNm and the maximum rotational speed at the wheels is 630rpm at driving speed of 100km/h. This introduces some demands of the 4QT drive system to fulfil all the driving requirements.

### 3.4.1 Only final gear

When using the 4QT system with a layout as in Figure 3.1, using only a final gear to reduce the torque from the wheel torque to the 4QT torque, the maximum speed at the wheel and the starting torque of the system become as shown in Figure 3.13 for different gear ratios.

If investigating the speed in Figure 3.13 the optimal gear ratio for driving at 100km/h is about 6, which gives a low speed for the DRM and thus low electrical power and losses in the electrical system. As mentioned above the maximum torque at the wheel from starting capability [31] requires a wheel torque of 9.5kNm. A final gear ratio of 6 requires a Stator torque of almost 1600Nm which can be compared to the maximum DRM torque that is equal to the ICE maximum torque of 297Nm. The Stator torque is thus 5 time larger. It is possible to optimize the system for both operation points with the usage of a two-speed gearbox. However, in the real case scenario the system has to be able to operate during a complete drive cycle with different speeds and torques.

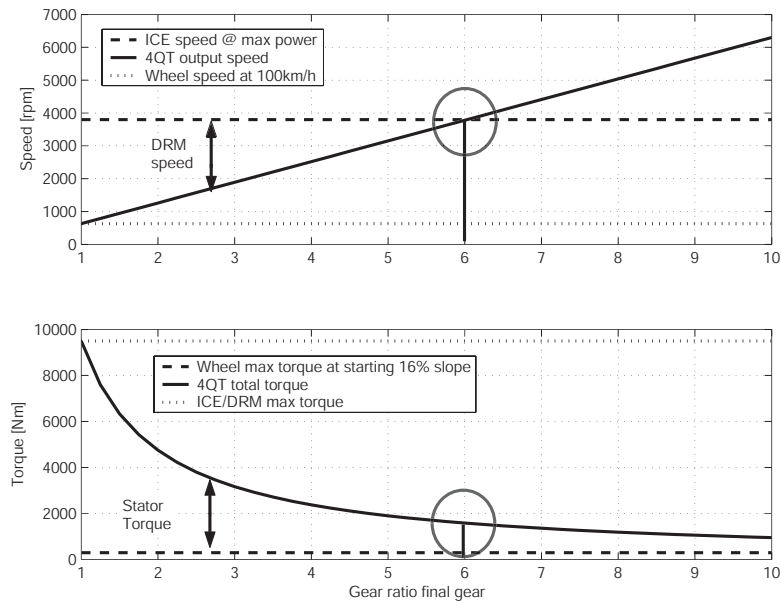


Fig. 3.13 Maximum speed and starting torque of the 4QT system with only a final gear for different gear ratios.

### 3.4.2 Gear box between the 4QT and the final gear

Usage of a gear box between the 4QT and the final gear will make it possible to reduce the sizes of the 4QT machines. Using more gears will further reduce the demands on the 4QT but one important reason to use the 4QT system is to reduce the need of gears. Since the torque demand at starting in steep slopes is high, it may be necessary to use at least a two-speed gear box to minimize the effects of this highest torque demanding mode of operation.

### 3.4.3 Gear between the ICE and 4QT

Usage of a constant gear between the ICE and the 4QT would increase the speed and reduce the torque of the inner rotor. Figure 3.14 shows the speeds at 100km/h and the starting torque at 16% slope for the 4QT system with a constant gear of gear ratio 2 between the ICE and 4QT.

As can be seen from the Figure 3.14 the inner rotor speed has increased to two times the ICE speed at maximum power compared to Figure 3.13, while the maximum torque on the inner rotor has been reduced by half.

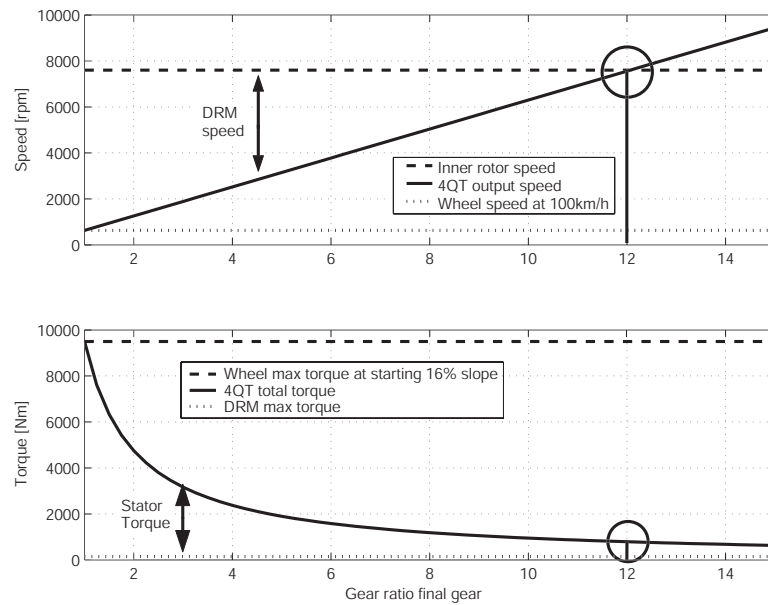


Fig. 3.14 Maximum speed and starting torque for the 4QT system with a gear with gear ratio 2 between the ICE and the 4QT for different gear ratios at the final gear.

According to Figure 3.14 the DRM speed becomes low at high gear ratios of the final gear. At a gear ratio of 12 on the final gear the DRM speed becomes zero. Using a high gear ratio in the final gear also decreases the torque required from the Stator. These changes will make it possible to achieve a compact 4QT machine which will, however, operate at high speeds. High speeds will impose new challenges on the 4QT design. The inner rotor will rotate at a maximum speed of 8000 rpm which will expose the inner rotor windings to higher centrifugal forces and expose the sliprings feeding the inner rotor windings to larger stresses. The outer rotor speed will also be dependent of the gear ratio but since the outer rotor consists of a solid steel tube the centrifugal force are of less significance. However, the demands of holding the outer magnets in place with suitable bandaging will increase.

The starting torque demand on the 4QT system at large slopes will be reduced with a high gear ratio of the final gear as seen in Figure 3.14, this reduces the torque demand on the Stator machine.

### **3.4.4 Using the 4QT as a retarder**

A retarder is a wear-free additional retarding braking system used in heavy vehicles such as buses and trucks. The retarder increases the safety of the vehicle and reduces the stresses and service on the braking system. There are several different retarder systems available in the market [2]:

#### ***Hydrodynamic retarders***

The hydrodynamic retarders are mounted on the drive shaft and during braking a rotor is used to convert mechanical energy from the drive shaft into kinetic energy in a fluid, oil. The amount of oil is controlled by pressurised air that is regulated by an electric control circuit that in turn is controlled by the drivers brake request. The following are some features of the hydrodynamic retarder:

- Relatively complex design
- Low weight of the retarder when it is integrated in the transmission
- High specific braking powers
- Very sensitive control of the applied braking power can be achieved
- Fan losses when retarder is not running

#### ***Electrodynamic retarder***

The electrodynamic retarder has field coils in a stator which when supplied by voltage produces a magnetic field in the rotor that induces eddy currents which will brake the rotor connected to the drive train. This gives an easy voltage regulated electric control of the brake torque by changing the supplied voltage. The following are some features of the electrodynamic retarder:

- Heat dissipated to the atmosphere
- Relatively simple design
- Relatively heavy construction
- Heating of the retarder decreases the braking torque
- High braking powers achievable even at low speeds

### ***Using the 4QT as a retarder***

The 4QT electric machine could be used as a retarder for the vehicle, thus limiting the need of an extra component in the drive train. The braking torque will be limited to the maximum torque of the 4QT. This maximum torque could be made up of either only the Stator torque or both the Stator and DRM torques. In a 4QT system without a lock-up function it is only possible to use the Stator as a brake. If a lock-up function is used on the ICE shaft there is the possibility of also using the DRM as a brake generator thus increasing the braking power of the retarder.

The brake power from the electric machines working as retarders in the 4QT system has to be stored in the battery or dissipated in some resistive load bank. The demands on the retarder from [31] are to keep a constant speed of 30km/h at a road slope of 7% for a distance of 6km. To do so a retarder brake power of 47kW is needed. To drive 6km at 30km/h takes 12min. This gives an energy storage requirement of 33MWs.

To conclude, it is possible to use the 4QT as a retarder, the challenge is not the limitations in the machine or the inverter operation, but in the storage of all the brake energy. Using a resistive load, would make it possible to use the 4QT as a retarder independent of the battery SOC.

## **3.5 Conclusions**

The 4QT system gives an opportunity to operate the ICE in a hybrid vehicle at optimal efficiency during all driving conditions. The system also makes it possible to use regenerative braking to save energy. Further, it is possible to drive the vehicle in pure electric mode within a drive range that is limited by the energy content, or minimum allowed SOC level, of the battery.

The 4QT system shows several advantages when compared to a conventional drive train system.

## 4 Drive cycle simulations

To determine the fuel consumption, efficiency and performance of the 4QT system, simulations under different driving conditions have been carried out.

There are also some driving demands on the system as listed below:

- Startability at 16% slope
- Gradeability, 75 km/h at 1.5% slope
- Maximum speed 100 km/h
- EV range of 2 km at a speed of 10 km/h

The vehicle should also have the capability to follow the FTP75 drive cycle. Because it is a heavy vehicle a slightly reduced FTP75 drive cycle has been used.

### 4.1 The target vehicle

The vehicle in the simulations is a twelve metric ton truck used for urban traffic. The chosen vehicle is a typical cargo truck used for delivering groceries to different stores in cities. This type of vehicles is especially suited for a hybrid drive as they almost only operate in urban traffic. The possibility to use pure electric mode is also an advantage when delivering goods to indoor locations.

*Table 4.1 Data for the simulated twelve metric ton truck.*

Vehicle data		
Curb weight	5.5	ton
Payload	6.5	ton
Gross vehicle weight	12	ton
Mean weight	8.75	ton
Front area	8	m <sup>2</sup>
Rolling radius	0.421	m
Drag coefficient	0.6	-
Rolling resistance	0.0055	-

The data for the used vehicle are shown in Table 4.1. The mean weight is the one used in the drive cycle simulations. This is because of the assumption that the vehicle is fully loaded at the start of the drive cycle and empty at the end. Thus the mean weight is the curb weight plus half the load weight.

The internal combustion engine is a 5-cylinder 2.25 litre turbo diesel engine. The maximum torque is 297 Nm at 2000 rpm and the maximum power is 100 kW at 3800 rpm. The maximum torque and power versus speed are shown in Figure 4.1 below.

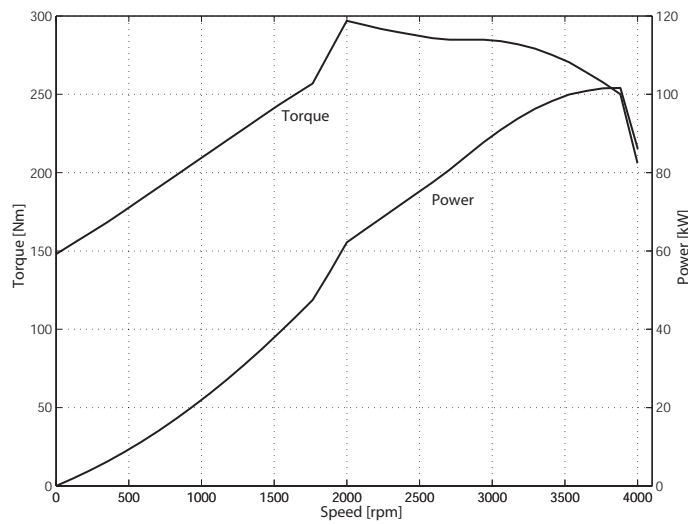


*Fig. 4.1 ICE maximum power and torque versus speed.*

The data for the five speed gearbox used in the simulations are shown in Table 4.2. The efficiency of the final gear is 0.97 and the final gear ratio is chosen to fit the requirements of the engine. For the simulated vehicle a gearbox is used to reduce the size of the 4QT machine.

*Table 4.2 Data for the five speed gearbox used in the simulations.*

Gear	Gear ratio	Efficiency
1	3.07:1	0.96
2	1.77:1	0.96
3	1.19:1	0.96
4	0.87:1	0.96
5	0.7:1	0.98

## 4.2 The simulation program

The program used for the simulations is running in the Matlab/Simulink environment. In Simulink a program of the backward facing type has been developed. The backward facing program calculates the required drive power at the wheels to follow a certain drive cycle, this power is then fed into the simulation program. The program then calculates the power that must be fed to the traction motor by taking into consideration the losses at the wheel, drivetrain and the traction motor itself. The opposite method is to have the drive cycle as a reference and let a simulated driver, e.g. modelled as a PI controller, drive the system with a throttle control and follow the reference drive cycle. This method is called forward facing program.

The program is divided in five different blocks, see Figure 4.2. The first block, which is the “POWER NEEDED” block, derives from the drive cycle the speed, torque and power required from the 4QT to drive the vehicle. The next block, “CONTROL ICE”, handles the control of the ICE so that the operation point is kept at the optimal operation line (OOL) at all conditions. The “ELECTRIC SYSTEM” block controls the 4QT and calculates the losses and the power that is either produced or consumed by the 4QT. The “BATTERY” block handles the battery management. The last block, the “EFFICIENCY” block, calculates the total fuel consumption in litres per km and the total efficiency of the system. The total efficiency is the actual energy used to drive the vehicle during the drive cycle divided by the specific calorific value of the used fuel. The blocks mentioned above and showed in Figure 4.2 are more clearly described in the licentiate thesis written by the author [23].

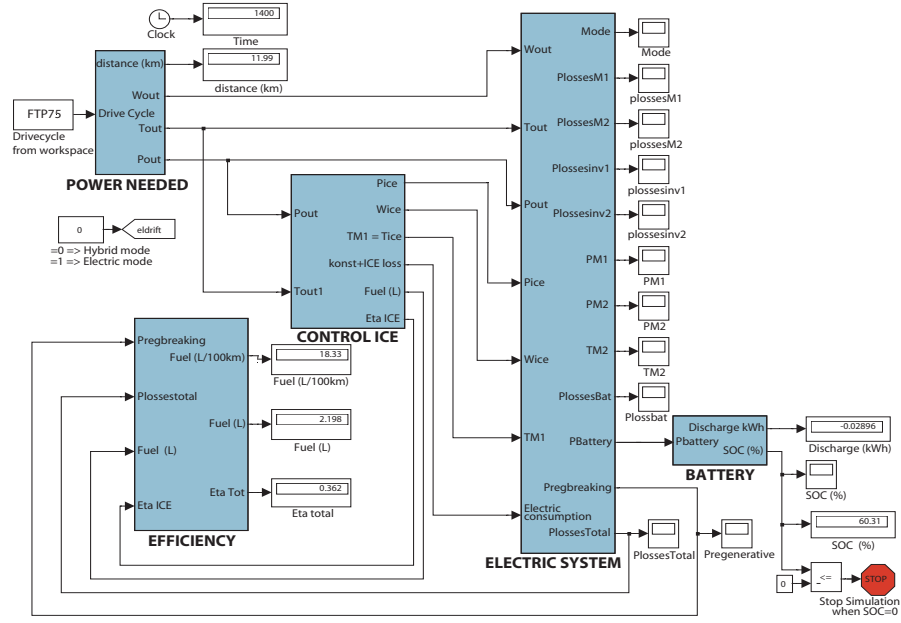


Fig. 4.2 The 4QT simulation program in Simulink.

### 4.3 The used drive cycle

There are a number of different drive cycles in the world today, adjusted for different countries and different regulations. The ones used in the simulations presented in this thesis are the FTP75 and the FTP72 [1]. FTP stands for Federal Test Procedure and denotes a drive cycle derived from measurements of the traffic speed in Los Angeles during one period in the morning [1].

As can be seen from Figure 4.3, the FTP75 drive cycle consists of two parts. The first part, referred to as the FTP72 drive cycle, starts with a cold ICE. The second part starts with a warm ICE which has only been allowed to cool down for six hundred seconds. The FTP72 drive cycle is the drive cycle that is officially used in Australia, Mexico, Sweden and Switzerland, while the FTP75 is used in America and Canada. The ECE15 (Economic Commission of Europe) drive cycle in Figure 4.3 is a synthetically developed drive cycle. The purpose was to form a drive cycle that is close to the real driving conditions in an urban traffic situation. This drive cycle is used in Germany, Netherlands, Belgium, Luxembourg, France, Denmark, Great Britain, Italy, Ireland, Austria, and Norway.



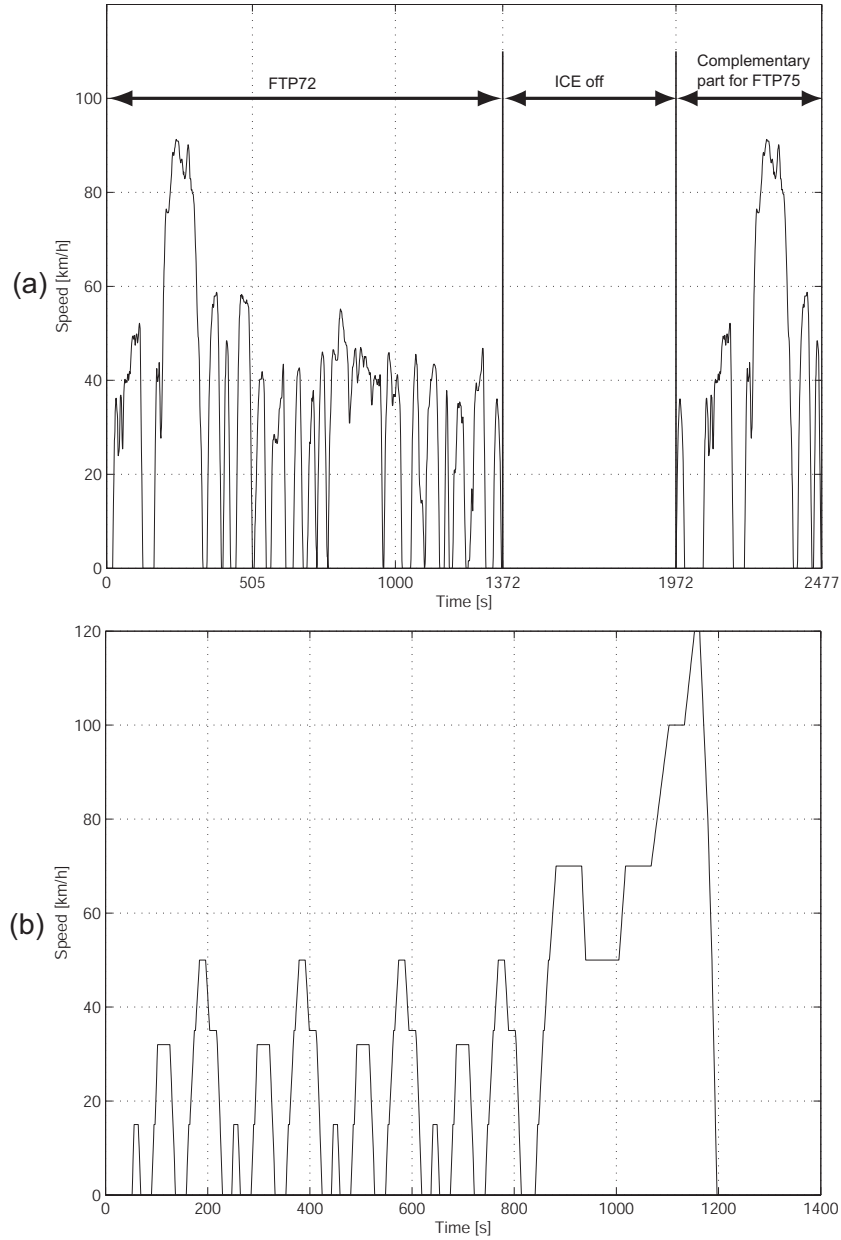


Fig. 4.3 (a) FTP75 and FTP72 drive cycles, (b) ECE15 drive cycle.

## **4.4 Simulation results**

The 4QT system has been simulated for different driving conditions. One was the FTP75 drive cycle and the others are listed below:

- Startability at 16 % slope
- Gradeability, 75 km/h at 1.5 % slope
- Maximum speed 100 km/h
- EV (Electric Vehicle) range of 2 km at a speed of 10 km/h

These demands were set on the 4QT system [24] and they are the same demands that are used for conventional vehicles of the same class, except the EV range demand.

### **4.4.1 Startability at 16 % slope**

This demand is used to secure startability at steep slopes. The major difficulty with this demand is the high torque required to start the vehicle from zero speed. The twelve ton truck, started with a constant acceleration of  $0.2 \text{ m/s}^2$ , requires a starting torque according to Figure 4.4. As can be seen in the figure the maximum torque at the 4QT output shaft is 790 Nm with a constant gear ratio of the final gear equal to 12.7. This gear ratio gives a maximum speed of the outer rotor of 8000 rpm at 100 km/h.

If instead a five-speed gearbox with data as presented in Table 4.2 is used together with a final gear with a gear ratio of 7.9, the rotational speed of the shaft becomes 3800 rpm at 100 km/h, which is close to the maximum power speed of the ICE. When starting at 16 % slope and a acceleration of  $0.2 \text{ m/s}^2$ , the required starting torque becomes 420 Nm using this configuration together with the highest gear ratio of the gearbox.

If the ICE is operating at maximum torque (297 Nm) when starting the vehicle, the Stator needs to supply the torque difference of either 493 Nm or 123 Nm for the two different cases.

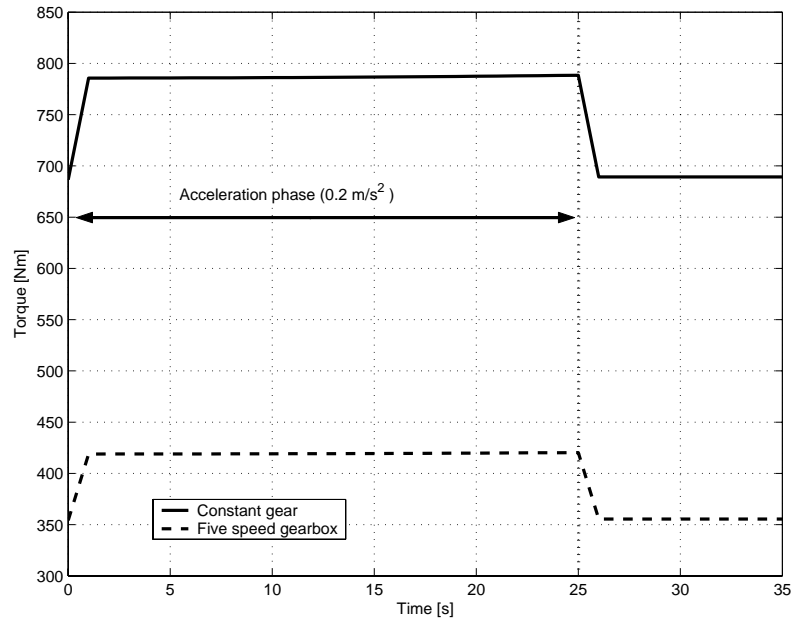


Fig. 4.4 Torque requirements at the output shaft of the 4QT during a start with 16% slope and a constant acceleration of  $0.2 \text{ m/s}^2$  with a constant gear and with a gearbox.

#### 4.4.2 Gradeability, 75 km/h at 1.5% slope

When driving at a speed of 75 km/h and a slope of 1.5%, the power, torque and speed at the final gear, the ICE, the DRM and the Stator are shown in Table 4.3. The most relevant figures in the table are the power produced by the ICE and the power required at the final gear. The total efficiency of the drive train becomes the power required at the final gear divided by the ICE power minus the auxiliary electric load of 3.65 kW. The drive train efficiency in this operating point becomes 93%, neglecting the efficiency of the ICE and the gearbox. A gearbox has an efficiency of about 96% and the ICE is, according to the ICE fuel consumption map, operating at an efficiency of 38% which is the maximum efficiency of the ICE at the required power. Combining the efficiency of the ICE, the 4QT drive train, and the gears, the total efficiency becomes about 34%. A conventional vehicle for the same operating condition has an efficiency that will depend upon the gear ratio but in most cases it will be lower than the efficiency of the 4QT equipped vehicle.

*Table 4.3 Speed, torque and power at 75km/h and 1.5% slope.  
The auxiliary power is 3.65kW.*

	T [Nm]	Speed [rpm]	Power [kW]
Final Gear	155.2	4271	69.4
ICE	237.2	3154	78.36
DRM	237.2	1117	27.7
Stator	-82	4271	-36.7

#### **4.4.3 Maximum speed 100km/h**

The maximum speed according to the regulations for this kind of vehicles is 100km/h. In Figure 4.5 the drive line diagram of the 12-ton vehicle is shown. The maximum continuous speed according to Figure 4.5 is 108km/h. This speed is limited by the maximum ICE power and the total road resistance. The link between the ICE speed via the gearbox and wheels to the vehicle speed is not valid when the 4QT system is used because the 4QT changes the speed so the maximum power point of the ICE matches the maximum speed. The maximum speed of the vehicle, if the 4QT is not used, is 106km/h which is the inner rectangle in Figure 4.5. In this case the maximum speed is limited by the chosen gear ratio of the final gear which should be optimized so that the maximum power and speed of the ICE is used at maximum speed of the vehicle. The maximum transient speed is the outer rectangle. This speed is limited by the maximum power from the ICE and the batteries together. Here the ICE/4QT speed is linked to the vehicle speed by the gears and the wheels. This speed is about 135km/h.

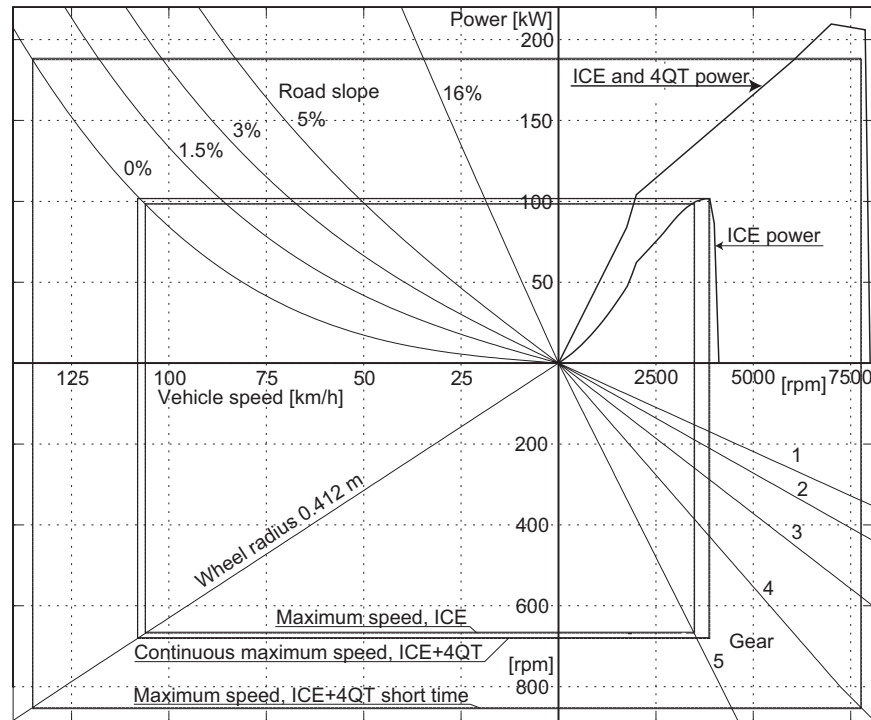


Fig. 4.5 Drive line diagram of a 12-ton truck.

The maximum continuous speed of the 12-ton vehicle should be 100 km/h. At this speed the ICE has to produce a power of 92.5 kW. From this power 83.6 kW is required to drive the vehicle, 3.65 kW is required for the constant auxiliary electric load of the vehicle and the remaining 5.3 kW are the losses in the electrical components. As can be seen in Figure 4.6, the power circulates in the system through the Stator which operates as a generator, the inverters and the DRM which performs as a motor. This gives of course rise to losses, but the electrical power to the DRM is low in this case and will only give rise to low losses from the power loop compared to the total power flowing through the 4QT. The simulations shows a fuel consumption of 26.7 l/100 km for the hybrid vehicle equipped with a 4QT. A conventional 12-ton vehicle of the same type has a fuel consumption of 26 l/100 km. This result shows as expected, no gain in fuel consumption for the hybrid vehicle at high constant speed, but neither does it give any significant increase in the fuel consumption. As can be seen in Table 4.4, the electric power losses are the absolute value of the Stator power minus the DRM power and the auxiliary electric load. Thus the electrical power losses become 5.3 kW in the electric components of the 4QT system.

Table 4.4 Speeds, torques and powers in the 4QT equipped vehicle at 100km/h. Auxiliary power 3.65kW.

	T [Nm]	Speed [rpm]	Power [kW]
Final Gear	243.2	3284	83.6
ICE	281.6	3137	92.5
DRM	281.6	147	4.3
Stator	-38.4	3284	-13.3

Table 4.4 shows the speed, torque and power in the different parts of the 4QT vehicle. The ICE operating point in this case is at 92.5kW, where the efficiency is 38%. The Stator operates as a generator and supplies the DRM and auxiliary components with power. The DRM increases the speed of the ICE to the required speed at the final gear.

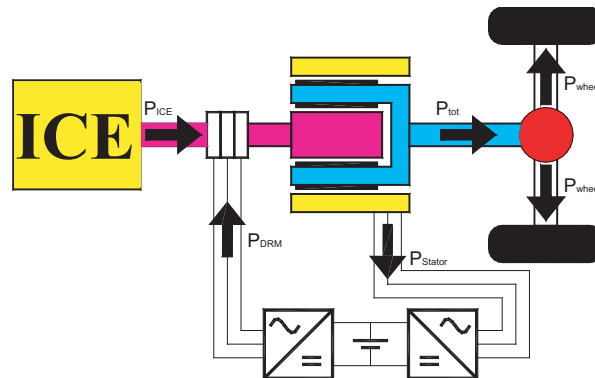


Fig. 4.6 Power distribution in the 4QT system at 100km/h.

## 4.5 FTP75 drive cycle analysis

The FTP75 drive cycle is used in Sweden during the prescribed exhaust testing of road vehicles. It is also the test cycle used when measuring the fuel consumption of a vehicle. In reality the drive cycle is started with a cold engine, this is not included in the simulation program. Neither is the simulation of the emissions included in the program.

### 4.5.1 Power demand during the FTP75/72 drive cycle

Driving a twelve ton vehicle in the FTP72 drive cycle is at the performance limit of the vehicle. The high powers and torques during the hardest acceleration set the constraints for the design of the 4QT.

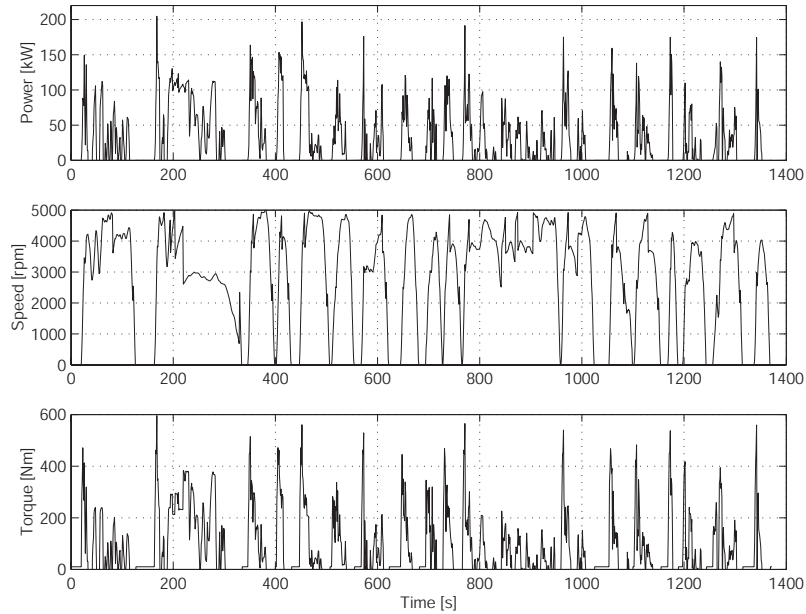


Fig. 4.7 Power, speed and torque required from the 4QT during the FTP72 drive cycle. A five-speed gearbox was included in the simulations.

Figure 4.7 shows the power demand at the final gear during the FTP72 drive cycle. This gives an idea of the required performance of the 4QT and the battery. To follow the drive cycle the battery has to be able to deliver the power difference between the maximum ICE power and the maximum power required by the drive cycle. As can be seen from Figure 4.7, the maximum power required during the drive cycle is 205 kW which can be compared to the maximum ICE power of 100 kW. This gives a minimum required battery power of 105 kW in order to be able to follow the FTP72 drive cycle. If the highest transient power peaks that are originating from gearshifts are neglected, implying just a small performance decrease, the maximum power required during the drive cycle becomes about 150 kW. With a maximum ICE power of 100 kW a minimum of 50 kW battery power is needed to enable the system to deliver the maximum power of 150 kW. The type of battery used in the simulation is a Li-ion battery with a power density of about 1 kW/kg. The battery weight will thus be 105 kg or 50 kg depending on the chosen performance of the vehicle. The maximum speed is about 5000 rpm

on the output shaft of the 4QT during the drive cycle, which should not pose any problem for the 4QT. The maximum torque, neglecting short torque transients, when using the five speed gearbox is about 500Nm during the drive cycle and the maximum deliverable ICE torque is 297Nm. The maximum required Stator torque then becomes 203Nm if the vehicle should be able to follow the requested drive cycle.

In the case of a constant gear the calculated power, speed and torque are shown in Figure 4.8. The power should be exactly the same as in Figure 4.7, and that is true if neglecting the short transients which originate from the gearshifts. The maximum speed of the 4QT during the drive cycle has increased to about 7000rpm and the maximum torque to 800Nm.

The dimensions of the 4QT transducer for a twelve ton vehicle, which has to follow the FTP75 drive cycle, will strongly depend on the gear ratio and the number of gears used in the vehicle. In the simulations a constant gear and a five speed gearbox, Table 4.2, together with a final gear has been used. According to the simulations the DRM has to deliver the same torque as the ICE, this gives the same DRM torque for the two different gear alternatives. However, for the case with the constant gear the 4QT speed is higher and therefore the DRM speed also becomes higher. The stator speed is also higher in this case. The maximum Stator torque becomes 203Nm in the case of the gearbox and 503Nm in the case of the constant gear. These values are dependent on the gear ratio of the final gear and of the gearbox.

When choosing the sizes of the two machines in the 4QT system, concern has to be taken to the maximum torque, but in a drive cycle the maximum torque is often a short transient and the largest continuous torque is often much lower. Figure 4.8 shows the torque during the FTP72 drive cycle when using only a constant gear, the maximum output torque of the 4QT is about 800Nm. Figure 4.9 shows the operation time at different torque levels in intervals of 20Nm for the 4QT machines during the FTP72. The DRM operates all the time between 200 and 300Nm and never over the ICE maximum torque. The Stator operates from 0 to 800Nm, but 50% of the time it operates below 120Nm, 75% of the time below 220Nm and it only operates short time periods at higher torques. This means that the maximum transient stator torque has to be 800Nm but the thermal limit of the design only needs to be around 200Nm, implying a required torque overload capability of 4 times for the Stator machine.



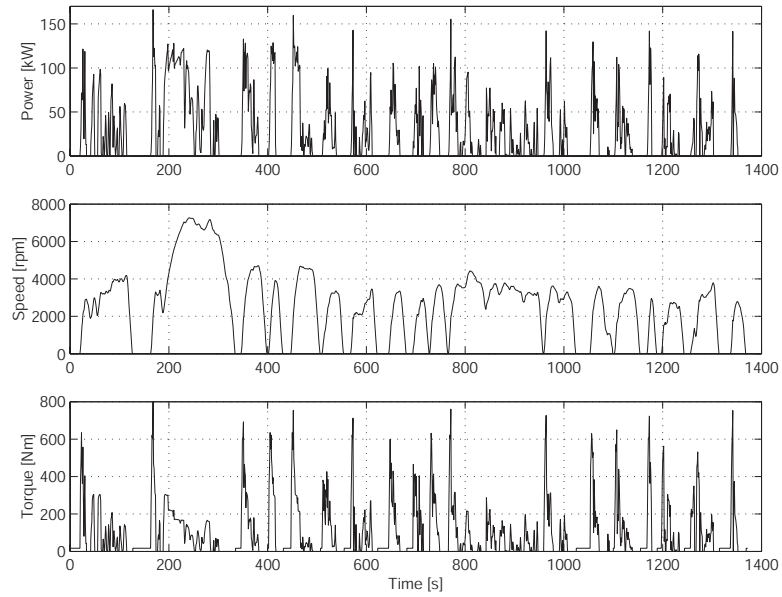


Fig. 4.8 Power, speed and torque of the 4QT during the FTP72 drive cycle, with a constant gear with the ratio of 12.7:1 (including the final gear ratio).

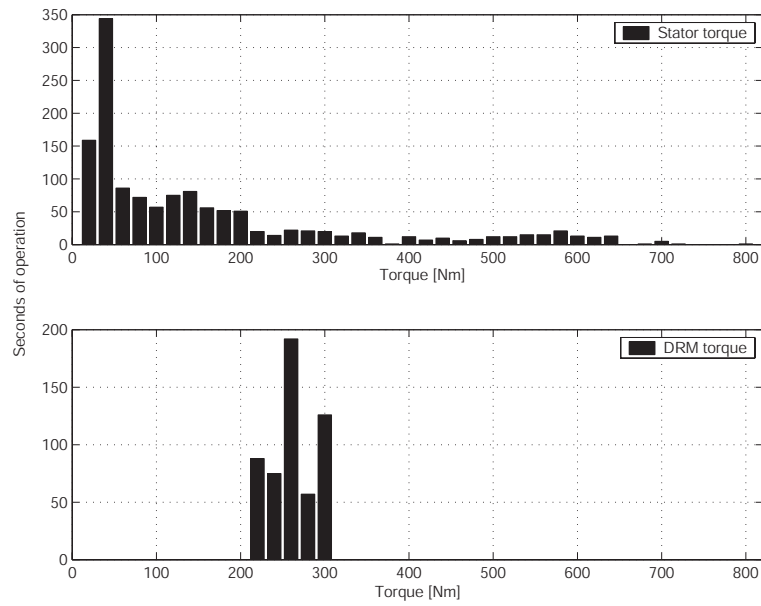
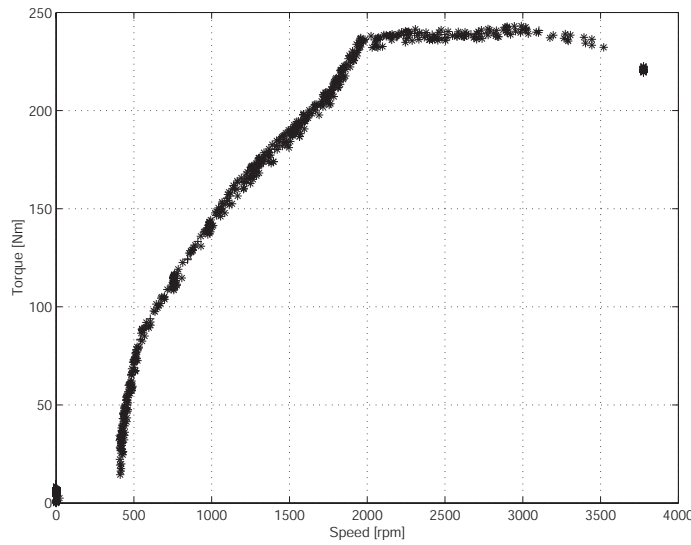
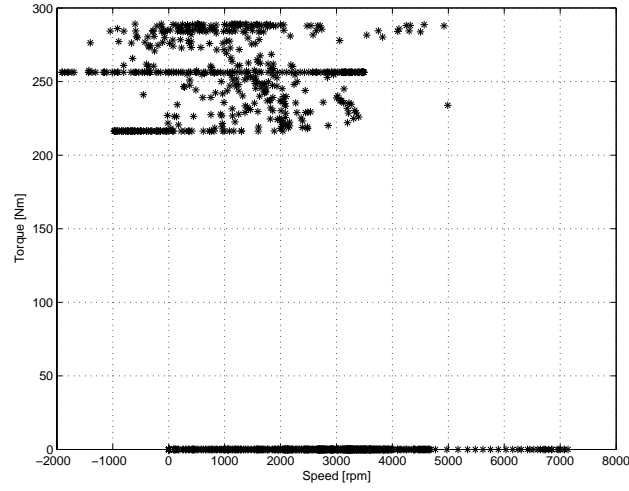


Fig. 4.9 Operation time at different torques (in intervals of 20Nm) for the Stator and the DRM.

The simulations shows that using a 4QT system decreases the fuel consumption of the vehicle by about 30% for the specified conditions. This decrease of fuel consumption is due to the more efficient use of the ICE and the use of regenerative braking. The ICE operation during the FTP72 drive cycle is shown in Figure 4.10, which clearly shows that during the complete drive cycle the ICE is operating following the OOL of the ICE. The DRM operates at the same torque as the ICE, and supplies the speed difference between the ICE and the final gear. The operation of the DRM during the FTP72 drive cycle is shown in Figure 4.11. The DRM operates mostly at high torques or at almost zero torque. The Stator operation is shown in Figure 4.12. As can be seen from the figure, the Stator operates over a wide speed and torque range, and at high speeds mostly as a generator. The large negative torque values are obtained during regenerative braking of the vehicle. Regenerative braking of the vehicle is producing 24% of the total energy used by the vehicle during the drive cycle. The total energy is the sum of the energy obtained from the regenerative braking plus the energy produced by the ICE. Each point in Figure 4.10 to Figure 4.12 represents one second of operation at that point.



*Fig. 4.10 ICE operation during the FTP72 drive cycle. (Each point corresponds to one second of operation.)*



*Fig. 4.11 DRM operation during the FTP72 drive cycle. (Each point corresponds to one second of operation.)*

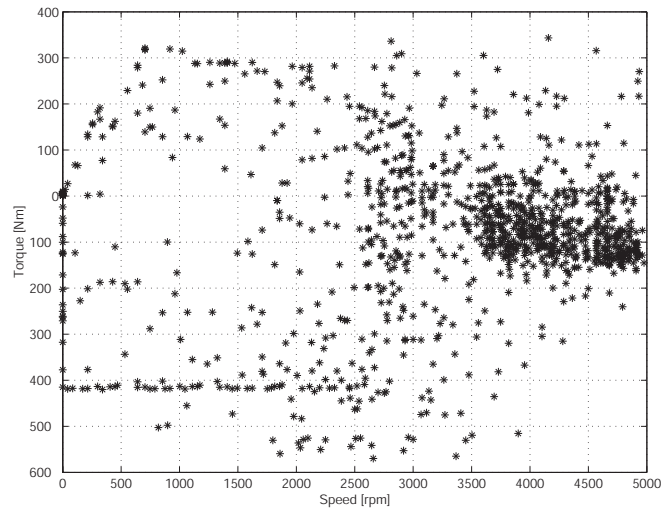


*Fig. 4.12 Stator operation during the FTP72 drive cycle. (Each point corresponds to one second of operation.)*

## 4.5.2 Fuel consumption simulations

The fuel consumption was simulated according to the method proposed in [7]. The principle of this method is to make a number of different tests over the same drive cycle and have different initial values of the battery SOC. The difference

between the start to stop SOC (the  $\Delta\text{SOC}$ ) during every test is plotted on the X-axis and the fuel consumption on the Y-axis in a graph. The real fuel consumption is assumed to be where the interpolated line intersects the Y-axis, this is at the zero SOC difference. This method is necessary when dealing with hybrid vehicles because the batteries are continuously charged and discharged during the drive cycle. The real value of fuel consumption can be calculated when there is no net charge into the battery during the drive cycle. If the battery net charge is positive the battery is charged during the drive cycle and this will give a higher fuel consumption. In contrast, if the battery is discharged during the drive cycle it contributes to the drive energy of the vehicle and the fuel consumption decreases. One way to decrease the fuel consumption of hybrid vehicles is to plug them into the grid and charge the battery before driving the vehicle. This has been investigated by for example [11].

Figure 4.13 shows the fuel consumption of the twelve ton vehicle plotted versus the  $\Delta\text{SOC}$  of the battery. The point where the line crosses the zero  $\Delta\text{SOC}$  value is the real fuel consumption. In this case the linear curve fitting gives a value of 181/100km for the fuel consumption during the FTP72 drive cycle. This value is for an auxiliary electric load of 3.65kW in the vehicle.

In Figure 4.14 the fuel consumption for the twelve ton 4QT hybrid truck is compared to a conventional truck of the same size. The fuel consumption for the FTP72 drive cycle is decreased for both auxiliary loads of 3.65kW and 12kW by about 30%. For a constant cruising speed of 100km/h there is no significant difference in the fuel consumption for the two vehicles.

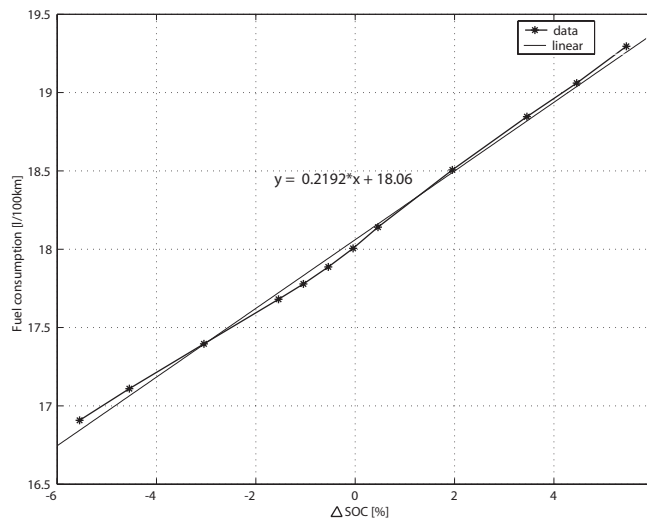


Fig. 4.13 Fuel consumption versus  $\Delta\text{SOC}$  for a twelve ton vehicle running FTP72.

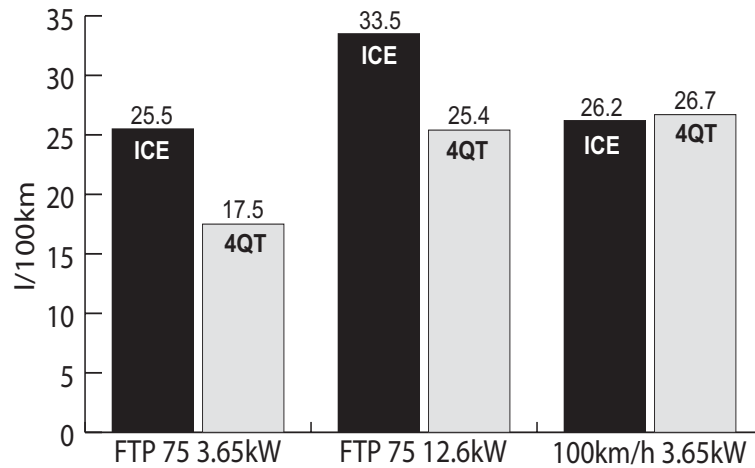


Fig. 4.14 Simulated fuel consumption for a conventional and a 4QT-equipped 12 ton truck during different driving conditions and auxiliary powers.

An auxiliary load is the extra electric load in the vehicle. In the example of the 12ton truck, the 3.65kW auxiliary load is for the basic functions in the vehicle. The 12.6kW auxiliary load is for a vehicle equipped with a freezer.

## 4.6 Battery size versus ICE operation

In a hybrid vehicle, the size of the battery is mostly dependent on the maximum battery power required to follow the drive cycle whereas in a pure electric vehicle battery size is mostly dependent on the battery energy requirement to achieve the required driving range. In the 4QT vehicle the battery size is also dependent on how fast the ICE responds to power transients. A fast response allows a decrease of the battery size, while a slow response requires an increase of the battery size. In Figure 4.15 the battery power is shown for the first 140s of the FTP75 drive cycle at two different time responses of the ICE. The negative values of the power in Figure 4.15 correspond to charging of the battery, and the large negative values occur when the vehicle is using regenerative braking.

Figure 4.15 shows how a fast response of the ICE decreases the required battery power and vice versa. This fast response is due to the direct correlation between the ICE power and the power requirements from the drive cycle. The battery that delivers the power difference between the required power and the power produced by the ICE can thus be decreased with a more transient operation of the ICE. The response time of the ICE is controlled by a low pass filter on the ICE power signal in the ICE control unit.

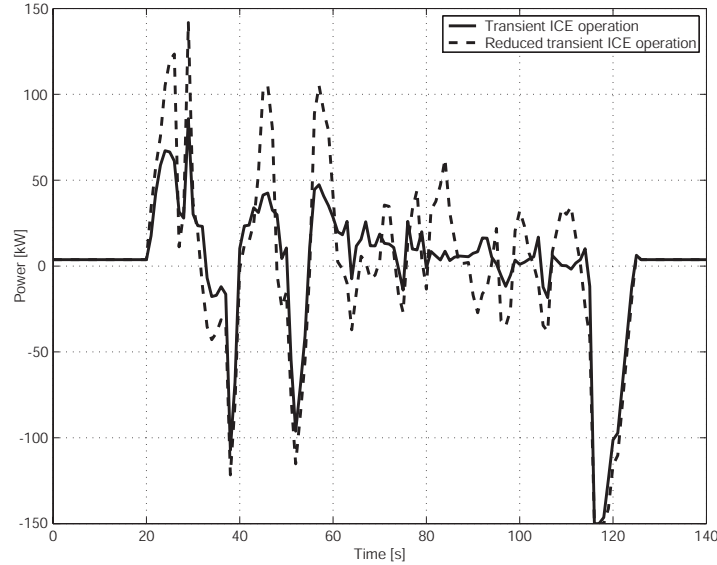


Fig. 4.15 Battery power at different transient operation of the ICE during the first 140s of the FTP75 drive cycle.

In Figure 4.15 the maximum required battery power is 141 kW and 85.8 kW respectively for the two different cases. The power density of the Li-ion batteries is about 1 kW/kg, this gives a decrease of the battery size of 55 kg for a more transient ICE operation. The disadvantage with this mode of operation is that the emissions increase because of the increased transient ICE operation. The efficiency of the ICE is also reduced with this mode of operation, but this does not always lead to increased fuel consumption, as less energy has to flow in and out of the battery.

#### 4.6.1 The importance of recovering the braking energy

Simulations were performed to investigate the fuel consumption of a 4QT hybrid vehicle for different strategies according to the list below in order to investigate the importance of regenerative braking. The fuel consumption for the different strategies are shown in Figure 4.16 and some drive cycle data are given in Table 4.5.

1. Maximum combustion engine efficiency 40%, no losses in the drive train
2. Maximum combustion engine efficiency 40%, all braking power fed back to the battery, no losses in the drive train
3. Maximum combustion engine efficiency 40%, maximum regenerative braking

- power is limited to 100kW, no losses in the drive train
4. Maximum combustion engine efficiency 40%, maximum regenerative braking power is limited 100kW and drive train efficiency of 80%
  5. 4QT hybrid system according to simulations earlier in this chapter
  6. Conventional vehicle

For the results in Figure 4.16 the values in Table 4.5 have been increased with the energy used for a constant electrical load of 3.65kW.

*Table 4.5 Energy components in the reduced FTP72 drive cycle.*

FTP72 drive cycle	Energy [Ws]
Total drive energy	$3.345 \cdot 10^7$
Total regenerative braking energy	$1.82 \cdot 10^7$
Regenerative braking energy, braking power limited to 100kW	$1.70 \cdot 10^7$

As can be seen in Figure 4.16, a minimum fuel consumption of 12.1l/100km for the reduced FTP72 drive cycle is achieved when maximum regenerative braking energy is recovered. When not using regenerative braking, the fuel consumption increases to 22.9l/100km. A conventional vehicle has a fuel consumption of 25.5l/100km [24]. The increase in fuel consumption due to the lower combustion engine efficiency and losses in the drive train is only 2.6l/100km. Thus the gain in fuel economy will be small when a hybrid vehicle without regenerative braking is used for a diesel driven heavy truck. Recovering the entire regenerative braking energy reduces the fuel consumption to 12.1l/100km, while limiting the regenerative braking power to 100kW due to battery and generator limitations gives a fuel consumption of 12.8l/100km. For this value all losses, except the losses in the ICE which is assumed to have a maximum efficiency of 40%, are neglected. Assuming a total drive train efficiency of 80% (from electrical machines, inverters, battery and gears) gives a fuel consumption of 16l/100km. The simulated value of the 4QT system is 17.5l/100km.

Comparing the 4QT system fuel consumption with the values for the other 5 proposed cases the values show that the fuel consumption of the simulations gives a reasonable value and that the gain in fuel economy mostly comes from regenerative braking.

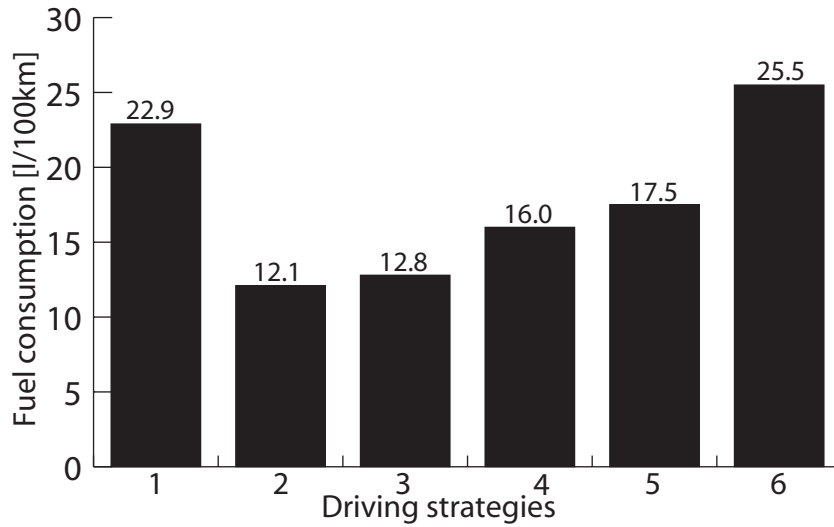


Fig. 4.16 Simulated fuel consumption for the different drive strategies for the reduced FTP72 drive cycle. Drive strategies are defined earlier in this section.

## 4.7 Conclusion and results

The drive cycle simulations give data on the behaviour, performance and efficiency of the 4QT vehicle drive system. Performance requirements of the 4QT transducer are also obtained from the simulations. The efficiency of the 4QT system when driving at 75km/h and 1.5% slope is 88.6%. The fuel consumption of the vehicle becomes 17.5l/100km for the reduced FTP72 drive cycle. This is 30% less than the fuel consumption of a conventional 12-ton vehicle of the same class.

In the simulations presented in this chapter the backward facing method was used, so no consideration has been taken to a simulated driver of the vehicle. Much more work can also be done on the ICE control. The used strategy is good but needs further optimization. The battery model is a simple constant efficiency model with only maximum power and energy limits. This model has to be further developed, the aspect of battery performance at different SOC should also be included.



## 5 The 4QT prototype design

As the 4QT transducer for a 12-ton truck is too large for the testing facilities at the department of electrical engineering an application for a smaller vehicle was desired. The machine data for the prototype was achieved from simulations performed at the department by Laurent Maquet [18] who derived the basic performance requirements of the 4QT system for a medium sized passenger car. During these simulation a combustion engine with the following parameters was used:

- 79kW maximum power at 5750rpm
- Maximum speed 6000rpm
- Maximum transient torque 148Nm at 3750rpm
- Maximum continuous torque 100Nm
- Torque at 1500rpm: 125Nm
- Torque at 6000rpm: 125Nm

Using the data above, the following performance was derived [18] for the DRM:

- $T_{DRM-rated} = 100\text{Nm}$
- $n_{DRM-base} = 3000\text{rpm}$
- $P_{DRM} = 31.4\text{kW}$

and for the Stator:

- $T_{Stator-rated} = 70\text{Nm}$
- $n_{Stator-base} = 4000\text{rpm}$
- $P_{Stator} = 29.3\text{kW}$

The DRM maximal continuous torque is the same as the ICE continuous torque, the stator torque is derived from the extra torque contribution needed to achieve the driving demands.

These values are performance data for the two machines in the 4QT according to Figure 5.1. The field weakening range in Figure 5.1 is only modelled as a constant power region.

The radial-radial 4QT machine is assumed to fit into a cylindric volume with a diameter of 260mm and an active length of 110mm. These dimensions exclude the housing, cooling ducts and auxiliary equipment, as for example the sliprings.

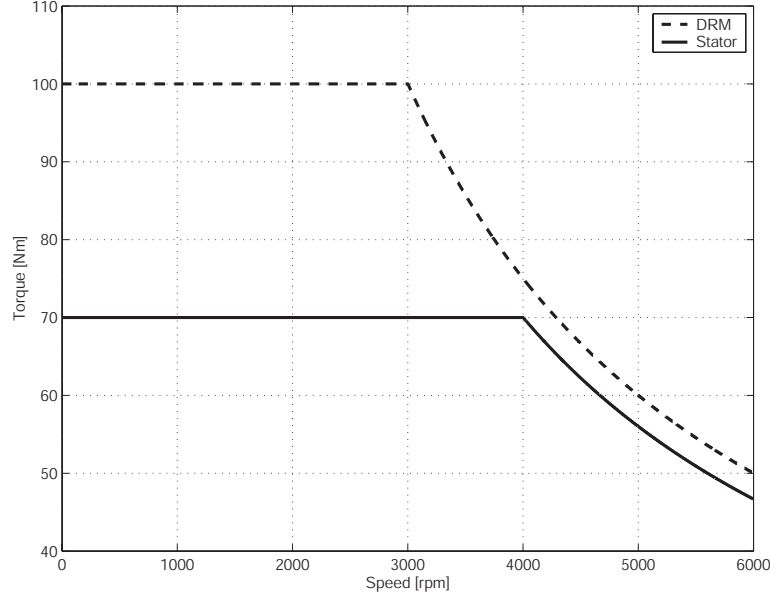


Fig. 5.1 The DRM and Stator performance in the prototype 4QT.

## 5.1 Pole number

The pole number was an important factor for the motor design. Using a higher pole number reduces the endwinding length and the stator back thickness, but increases the fundamental frequency of the machine. A higher fundamental frequency gives higher iron losses and requires smaller strands in the wires to reduce the skin effect.

For the 4QT the most important factors that influence the choice of the pole numbers were different for the two machines. The iron losses and skin effect properties were important for both machines, as they are for most electrical machines. For the DRM the stator back thickness is of minor importance because it is an outer rotor design and the stator back measured from the slot bottom to the shaft is normally large. The outer stator is as a conventional machine and in order to build a compact machine with a small outer radius this stator back should be kept thin.

The end winding length is more important for the DRM than for the Stator machine. This is because the rotating windings of the DRM will be vulnerable to centrifugal forces, and the length of the DRM end windings will also have a large impact on the total machine length since it is inside the outer rotor.

Using the same pole number for the DRM and the Stator reduces the outer rotor thickness. Since the no-load flux only penetrates straight through the outer rotor in radial direction, and small no-load flux is leaking between the poles in the outer rotor.

For the 4QT machine a high pole number that reduces the end winding length was preferred in order to reduce the copper losses and to minimize the effects of centrifugal forces on the end windings.

Thus a pole number of 12 poles was chosen. This gave the machine the following end winding length according to [15]:

$$L_{ys} = \frac{y_{sp} \cdot \tau_s}{2} + (n - 1/2) \cdot b \quad (5.1)$$

where  $y_{sp}$  is the pitch length,  $\tau_s$  is the slot pitch,  $n$  is the number of coil parts and  $b$  is the slot width. This equation gives an axial length of the end windings of 27.8mm for the DRM and 33.7mm for the Stator. On the prototype machines the measured lengths were 55mm for the DRM and 35mm for the Stator. For the Stator with almost square slots there was thus good agreement but for the DRM with deep slots equation (5.1) gave only about half the value of the measured endwinding length. This was solved during the manufacturing of the prototype by first winding the Stator and the inner rotor and then deciding the total length of the outer rotor and the housing.

## 5.2 Analytic design

The main purpose for the manufacture of the prototype was to validate the general functionality of the 4QT machine, thus no real optimization was made for the design of the prototype. The DRM design is based on the design and dimensions from [3], with only some minor changes. The 4QT was assumed to be fed from a battery with a DC voltage of 246V when loaded with rated current.

### 5.2.1 Basic design of the DRM

The DRM is in many ways based on an earlier prototype, the Integrated Energy Transducer (IET) [3]. In the newer prototype the radius of the inner rotor was slightly increased. This made it possible to increase the slot area and as a result decrease the current density and cooling requirements of the windings.

The double rotor machine has a base speed of 3000rpm and a base torque of 100Nm, which gives a base output power of 31.4kW. Assuming an efficiency of 90% at base speed and a displacement power factor equal to 1, gives an input power of 34.9kW.

With the chosen battery voltage the RMS-value of the fundamental component of line to line voltage becomes [19]:

$$U_{ll} = \frac{U_{dc}}{\sqrt{2}} = 174V \quad (5.2)$$

when assuming a quasi-sine shaped reference waves, i.e. with third harmonics injection and a modulation index equal to unity.

This gives a phase voltage of:

$$U_{ph} = U_{ll}/(\sqrt{3}) = 100,5V \quad (5.3)$$

Using this phase voltage and the input power, the phase current  $I_{ph}$  becomes:

$$I_{ph} = \frac{P}{3U_{ph}} = 115,8A \quad (5.4)$$

Assuming an airgap flux density  $\hat{B}_\delta = 0.8$  T gives for values of the diameter  $D = 180$  mm, number of poles  $p = 12$ , frequency  $f = 300$ Hz and a base speed of  $n = 3000$ rpm the following number of conductors per slot ( $N_s$ ) [15]:

$$N_s = \frac{U_{ph}}{\sqrt{2} \cdot \pi \cdot L \cdot D \cdot (f \cdot \hat{B}_\delta)} \quad (5.5)$$

This value becomes 4.76 but it has to be an integer so the chosen value is 5. Using  $N_s = 5$  gives a flux density  $\hat{B}_\delta = 0.76$ T.

The slot pitch of the DRM with the number of rotor slots  $Q_r = 36$  becomes:

$$\tau = \frac{\pi \cdot D}{Q_r} = \frac{\pi \cdot 180}{36} = 15,7mm \quad (5.6)$$

This gives a current loading of:

$$S_{rms} = \frac{N_s \cdot I_{ph}}{\tau} = 368 \text{ A/cm} \quad (5.7)$$

The rotor slot dimensions are shown in Figure 5.2. Using this rotor slot shape with 5 conductors per slot, a slot area of 216 mm<sup>2</sup> (Autocad drawing data) and assuming a copper fill factor of 45.6%, gave a current density of 5.88 A/mm<sup>2</sup> (RMS) in the copper. In the actual machine, the five conductors were each made of 25 strands with diameter 0.95 mm. The copper area is thus 88.6 mm<sup>2</sup> which gives a fill factor and current density of 41 % and 6.5 A/mm<sup>2</sup>, respectively.

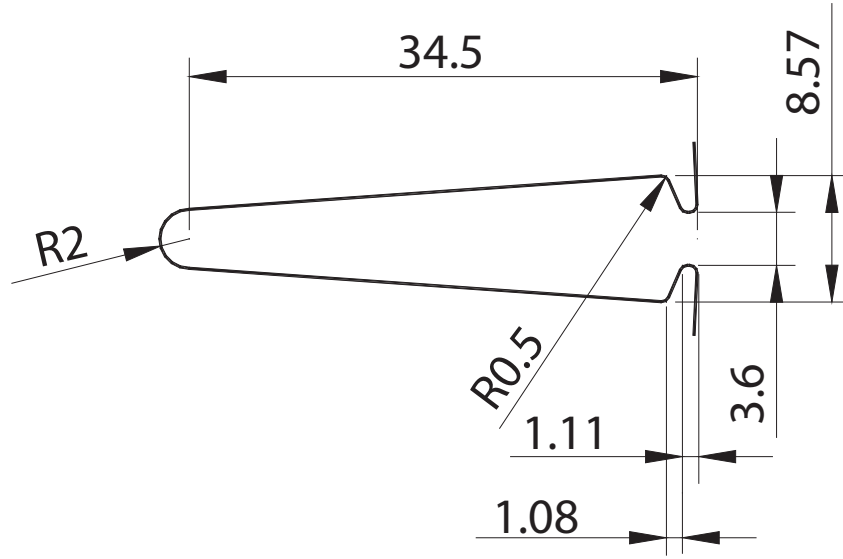


Fig. 5.2 Rotor slot dimensions. All dimensions are in mm.

All sharp corners have a radius of 0.25-0.5 mm due to the laser cutting of the sheets. This was necessary both for the stator and rotor laminates.

### 5.2.2 Calculation of the “DRM” magnet thickness

An accurate calculation of the magnet thickness is essential in the design of permanent magnet machines. In this design magnetic saturation is taken into consideration by increasing the analytically calculated magnet thickness by 20%. The thickness was calculated from equation (5.8) and equation (5.9). With  $\hat{B}_\delta = 0.76$  T,  $B_{r,magn} = 1$  T,  $\mu_r = 1.05$  and the magnet arc angle  $\alpha = 60^\circ$  for an air-gap length  $\delta = 1$  mm, a magnet thickness  $t_m$  of 2.56 mm was achieved. Taking saturation into account the thickness becomes 3 mm.

$$B_m = \frac{\pi \hat{B}_\delta}{4} \frac{1}{\sin \alpha} \quad (5.8)$$

$$B_m = B_{r, \text{magn}} \frac{1}{1 + \mu_r \frac{\delta_e}{t_m}} \quad (5.9)$$

Where  $\delta_e = \delta \cdot c_f$  is the equivalent air gap length, i.e. the physical air gap length  $\delta$  times the carter factor  $c_f$ .

This initial analytical design was further investigated and validated with the FE method.

### 5.2.3 Basic design of the Stator

The stator airgap radius was determined by the inner rotor radius and the outer rotor thickness. The outer radius of the stator was defined by the geometrical limits set for the prototype. The active length and the pole number are the same as for the DRM.

The base speed of the stator was 4000rpm and the base torque was 70Nm. This gave a base output power of 29.3kW. Assuming an efficiency of 95% and a displacement power factor equal to unity, gives an input power of 31kW.

Using the same battery as for the DRM gives, with the voltage drop over the internal resistance in the battery, the following voltage level of the DC voltage at rated load is estimated to be:

$$U_{dc} = E_{bat} - R_{bat} \cdot I_{max} = 250V \quad (5.10)$$

where  $E_{bat}$  is the battery voltage,  $R_{bat}$  the internal resistance of the battery and  $I_{max}$  is the maximal current from the battery. According to equation (5.2) the line to line voltage becomes square root of two times lower:

$$U_{ll} = 177V \quad (5.11)$$

This gives a phase voltage of:

$$U_{ph} = 102V \quad (5.12)$$

Using this phase voltage the phase current  $I_{ph}$  becomes:

$$I_{ph} = 101A \quad (5.13)$$

Assuming an airgap flux density  $\hat{B}_\delta = 0.8 \text{ T}$  gives for values of diameter  $D = 217.2 \text{ mm}$ , number of poles  $p = 12$ , frequency  $f = 400 \text{ Hz}$  and a base speed of  $n = 4000 \text{ rpm}$ , the following number of conductors per slot ( $N_s$ ) according to [15]:

$$N_s = \frac{U_f}{\sqrt{2} \cdot \pi \cdot L \cdot D \cdot f \cdot \hat{B}_\delta} \quad (5.14)$$

This value became  $N_s = 3$  which is an integer.

The slot pitch of the machine with the number of stator slots  $Q_s = 36$  becomes  $18.95 \text{ mm}$  according to equation (5.6). This gives a current loading of  $S_{rms} = 160.4 \text{ A/cm}$  according to equation (5.7).

The stator slot dimensions are shown in Figure 5.3. Using this stator slot shape with the numbers of conductors per slot equal to 3, a slot area of  $99.8 \text{ mm}^2$  (Autocad drawing data) and assuming a fill factor of 45.6%, gives a current density of  $6.68 \text{ A/mm}^2$  (RMS).

The real copper area, fill factor and current density for the prototype machine with 19 strands with  $0.95 \text{ mm}$  diameter per turn and 3 turns became  $40.4 \text{ mm}^2$ , 40.5% and  $7.5 \text{ A/mm}^2$  RMS respectively.

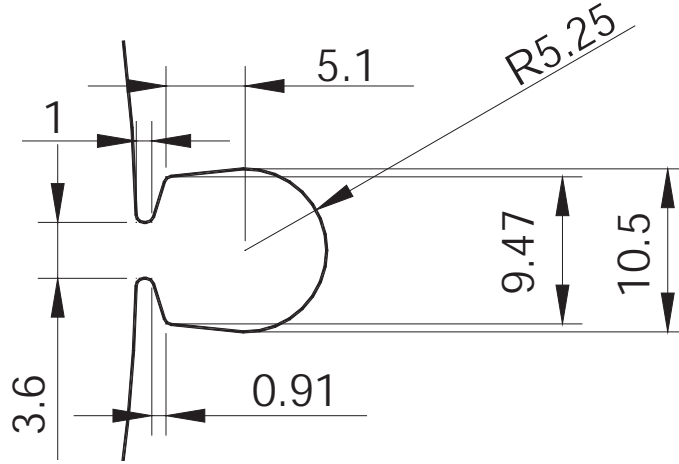


Fig. 5.3 Stator slot dimensions. All dimensions are in mm.

### 5.2.4 Calculation of the “Stator” magnet thickness

The magnet thickness of the Stator was calculated from equation (5.8) with the same method as used for the DRM. The magnet thickness becomes  $2.8 \text{ mm}$  and by taking saturation into account the thickness becomes  $3.4 \text{ mm}$ .

## **5.3 FEM investigation of the design**

The analytical design was confirmed and the cogging torque, torque ripple, inductance and field weakening performance were investigated using FE models of the 4QT.

### **5.3.1 Magnetic airgap flux density**

The 4QT has two airgaps and therefore two different airgap flux densities. The inner airgap flux density is produced by the inner magnets and the outer by the outer magnets for the outer airgap. The inner magnets are surface mounted on the inner surface of the outer rotor and the outer magnets are of inset type and breadloaf shaped. This breadloaf shape gave a more sinusoidal airgap flux density wave shape compared to the case of magnets with constant thickness. The outer magnets had a distance of twice the airgap to the iron in the circumferential direction to reduce flux leakage. The flux distribution created by the magnets at no-load in the machine is shown in Figure 5.4. The resulting magnet flux at no-load penetrates straight through the outer rotor and into the inner rotor.

The outer magnets are bandaged with a carbon fibre composite to hold them in place when centrifugal forces are acting on them. The shapes of the airgap flux densities in the outer and inner airgaps are shown in Figure 5.5 and Figure 5.6, respectively. As can be seen in the figures, the peak value of the fundamental component of the airgap flux density is 0.76T for the outer airgap and 0.85T for the inner airgap. The outer airgap has lower airgap flux density even though the outer magnets are thicker. This is because the outer airgap length is 1.6mm while the inner airgap length is 1mm. The larger airgap is necessary to accommodate the carbon fibre bandage. The inner magnets do not require a bandage since they are pressed against the rotor surface by the centrifugal forces.

The analytical values of the airgap flux density used for calculating the magnet thickness are 0.8T for the outer airgap and 0.76T for the inner airgap. To the magnet thicknesses an extra 20% is added to take the saturation effects into account. For the inner airgap this gives a magnet flux density slightly higher using FEM than the analytical value. For the outer airgap which is larger and which is magnetised by inset magnets this give an airgap flux density slightly lower using FEM than the analytical value.



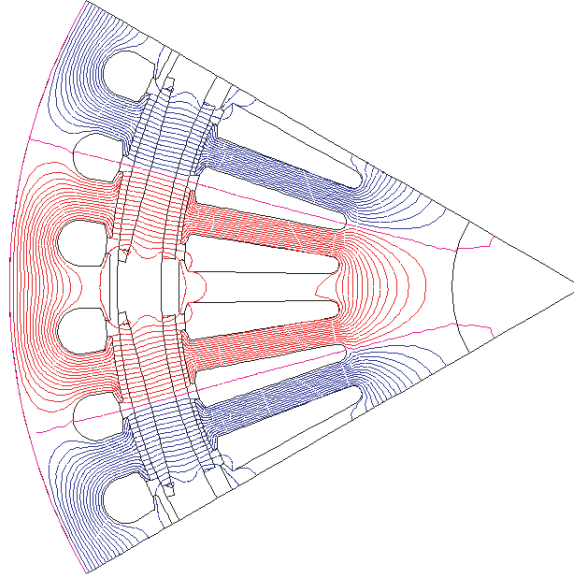


Fig. 5.4 Flux distribution in the 4QT at no-load.

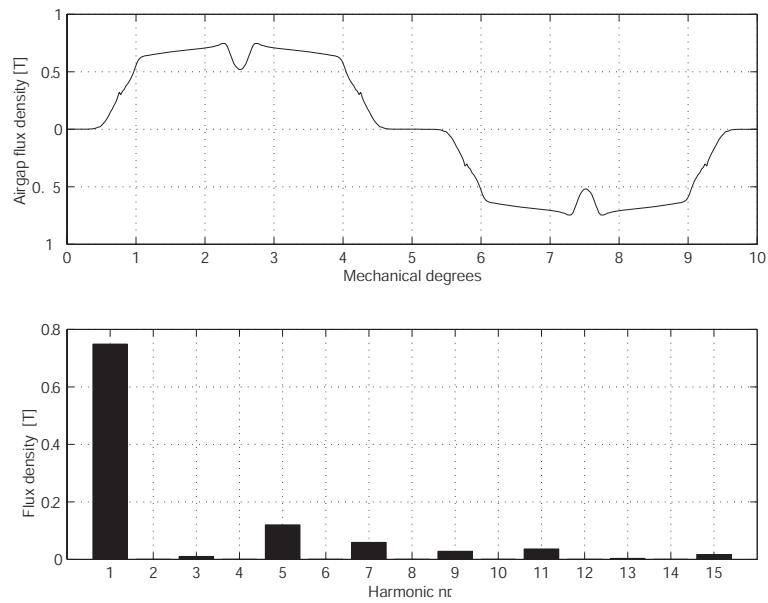


Fig. 5.5 Outer airgap flux density and corresponding harmonics.

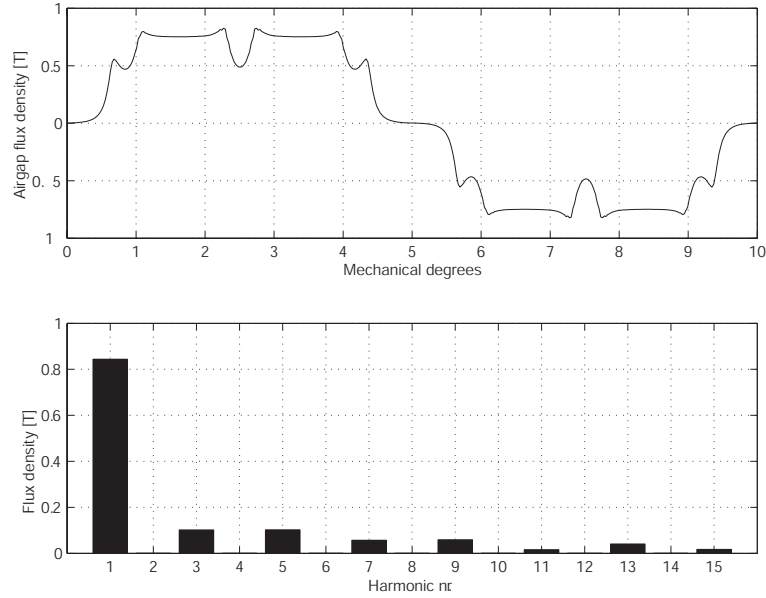


Fig. 5.6 Inner airgap flux density and corresponding harmonics.

### 5.3.2 Back EMF

The back EMF (Electromotive Force) or the voltage induced in the windings by the magnetic flux is one of the factors that decides the operating voltage of the machine.

The 4QT is in fact made of two separate machines with two separate windings and thus there are two different back EMF's. The back EMF was calculated both with a semi-analytical method from [9] and by the time stepping FE method [12].

The values from the semi-analytical, FE and measurements are shown in Table 5.1. The FE analysis and measured waveforms are shown in Figure 5.7 and Figure 5.8.

The semi-analytical calculated and measured RMS values show good agreement with an error of between 1.2 to 11 %. The difference between the FE values and the measured values lie between 6.2-7 % for the two windings. One of the factors that contributes to this difference is the skewing of the windings, which is skewed by one slot pitch both for the DRM and the Stator, thus reducing the winding factor. The winding factor for a motor with one slot per pole per phase and a pitch length of three slots is equal to one [15] and that is the case for the

non-skewed machine. When skewing the slots by one slot pitch, the winding factor is reduced according to equation (5.15) from [3],[15] to 0.95, which will also reduce the induced voltage by 5 %. If this is included in the calculation the difference between the FE analysis and the measured values will lie between 1.2-2 % for the Stator and DRM, respectively.

$$k_{\text{skew}} = \frac{\sin \frac{\pi}{6q}}{\frac{\pi}{6q}} \quad (5.15)$$

The wave forms for the FE analysis and the measured values show good agreement as seen in Figure 5.7 and Figure 5.8. As seen in the figures the measured curves are much smoother than the curves from the FE analysis, this is because the FE analysis was based on a 2D model while the measured values of course include the slot skewing.

Table 5.1 Back EMF values for semi-analytical, FE and measured values.

	Semi analytical		FE analysis		Measured
	Back EMF [V]	Difference [%]	Back EMF [V]	Difference [%]	Back EMF [V]
Stator	166	1.2	175.5	7	164
DRM	200	11.2	191	6.2	179.9

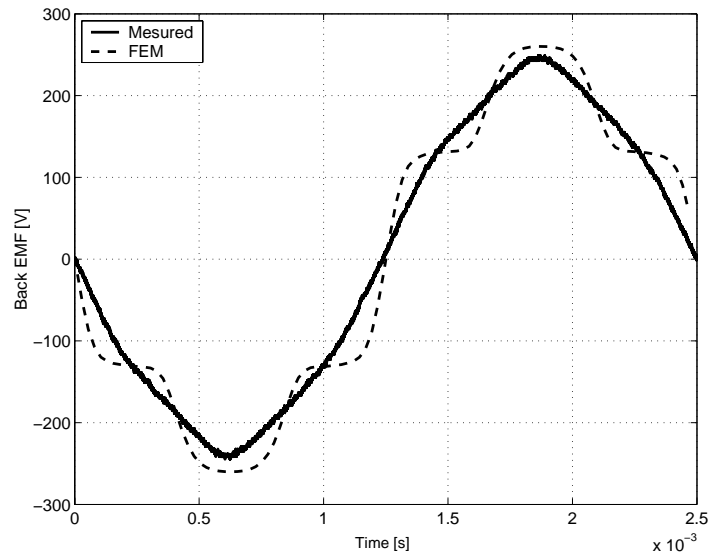


Fig. 5.7 Measured and FE simulated back EMF for the Stator machine.

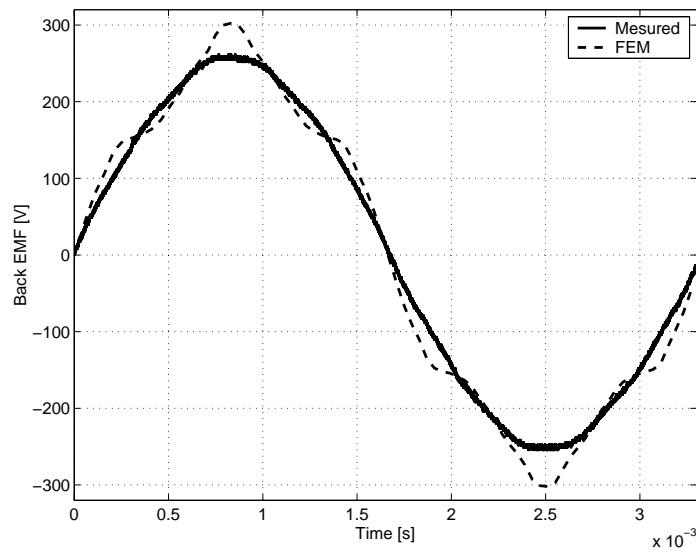


Fig. 5.8 Measured and FE simulated back EMF for the DRM machine.

### 5.3.3 Cogging

The cogging torque occurs when the magnets are moved close to a non-smooth surface such as slot openings in a stator. The cogging torque is the resulting torque from the forces at the leading and lagging ends of the magnets, that either holds or pushes the magnets against or along the direction of rotation of the rotor.

There are several ways to reduce the cogging torque such as magnet design, changing the geometry of the machine or skewing of either the rotor or the stator.

It is possible to design the magnets with chamfered edges and/or change the pole arc design to an optimal value to reduce the cogging torque [27].

The machine geometry can be changed in different ways, as an example dummy slots can be inserted between the real slots. This will reduce the amplitude and increase the frequency of the cogging dependent on the shape and number of dummy slots [28].

Skewing is usually used in induction machines where the rotors are continuously skewed. In a PM machine the skewing of the rotor means staggering of the magnets which has to be done in steps. This reduces the cogging but is not as effective as in the case of a continuous skew. In the 4QT machines another approach was used; instead of skewing the PM rotor, the windings in the stator and the inner rotor were skewed continuously by one slot pitch. When the skewing angle is equal to the period of the cogging torque, and the skewing is one slot pitch, the cogging torque is theoretically reduced to zero [29].

When the windings are skewed, as in the 4QT machines, the magnet shape can be chosen for easy and cheap manufacturing with straight edges. The skewing in the 4QT, from the cogging point of view, is in fact not continuous but made up of 315 steps which is equal to the number of laminations. This together with some end effects will give some cogging contribution in the machine.

The cogging was simulated with 2D FE analysis [12] and with analytical methods [30]. For the FE model the skewing was simulated by changing the geometry of the model to different steps of skew. Figure 5.9 shows an example of a 2-step skew of the inner rotor. When the number of steps were increased the cogging decreased. According to [34] 8 steps gives satisfactory results for the 4QT machines.

Figure 5.10 shows the cogging for the stator machine calculated both analytically according to [30] and with the FE method for different numbers of the step skewing. As can be seen from the figure, the cogging was reduced when increasing the number of steps. Figure 5.11 shows the FE cogging torque for the DRM which shows the same trend as for the stator machine with decreasing cogging

torque when increasing the number of steps.

Skewing of the lamination packages of the stator and inner rotor of the 4QT machine will reduce the cogging torque to almost zero except for the contribution from the axial sides of the machine.

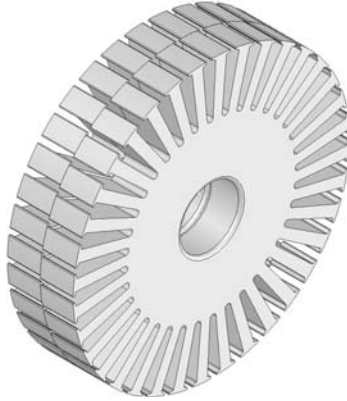


Fig. 5.9 An example of step skewing for the inner rotor winding used in the FE simulations.

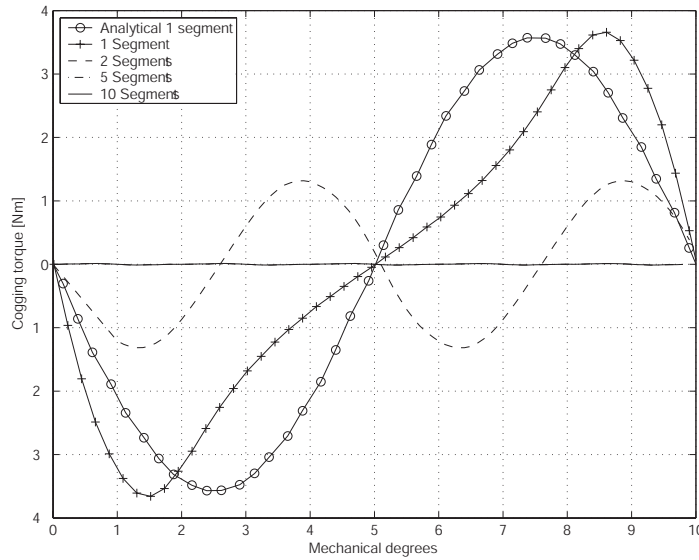


Fig. 5.10 Cogging torque for the Stator calculated analytically and using the FE method with varying number of steps in the axial direction to simulate winding skew.

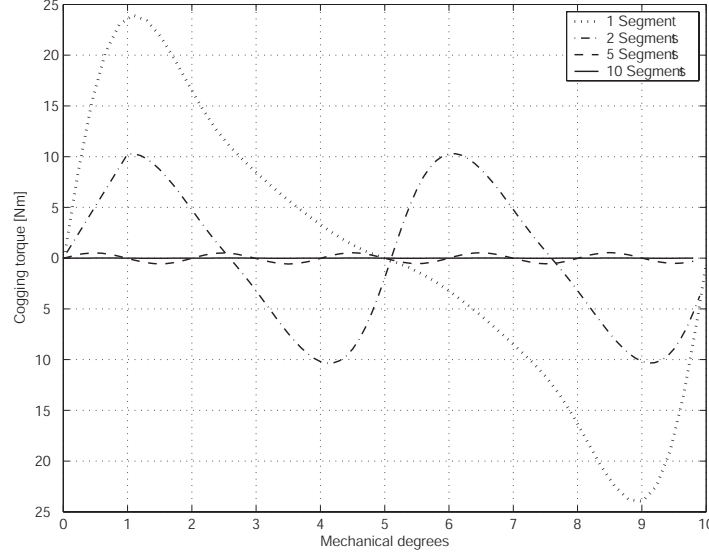


Fig. 5.11 Cogging torque for the DRM, calculated using the FE method for varying number of steps in the axial direction to simulate winding skew.

### 5.3.4 Torque ripple

The torque ripple in an electrical machine is much lower than in combustion engine, where there is a large peak torque at every ignition. This is the reason why a flywheel is used in a conventional vehicle drive line. In the 4QT system the inner rotor inertia could act as a flywheel, it is possible that the system also needs a conventional flywheel but this has not been included in the investigation. The torque ripple of the two electrical machines in the 4QT has been investigated with the help of time stepping FEM.

FEM simulations of the torque ripple at base speed of both the Stator and the DRM was performed with windings skewed in different steps. Figure 5.12 and Figure 5.13 show the ripple torque for the DRM and Stator respectively, with windings skewed in steps as described by Figure 5.9. The values of the ripple torque are presented in Table 5.2. There it is quite obvious that the torque ripple of the machines are drastically reduced when skewing is used. When the number of skew steps are increased, the torque ripple will be smaller. In the torque ripple calculations only the active part of the machine contribute to the torque ripple. In a real machine there will be an extra torque ripple contribution from end effects, eccentricity and mechanic tolerances.

Table 5.2 Mean torque and peak-to-peak torque ripple for the Stator and the DRM.

	Stator		DRM	
	[Nm]	[%]	[Nm]	[%]
Mean	67	100	118.2	100
1 step	15	22	37.9	32
2 steps	5.9	9	16.1	13.6
4 steps	1.1	1.6	5.0	4.2

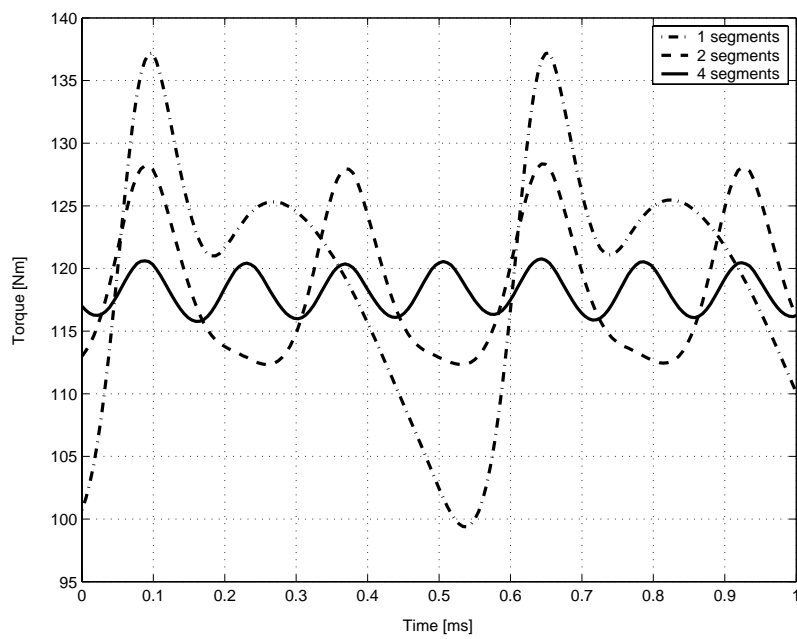


Fig. 5.12 Torque ripple for the DRM.



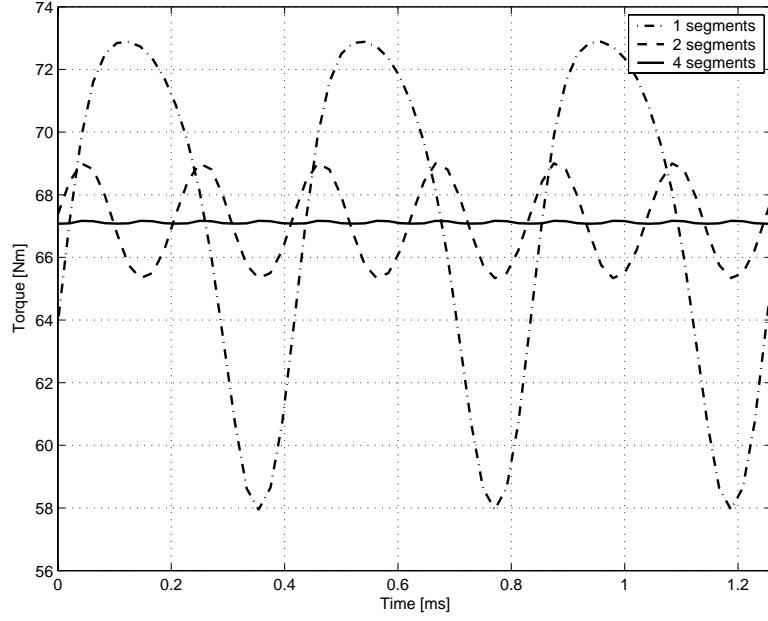


Fig. 5.13 Torque ripple for the Stator.

## 5.4 Inductances

The inductances of the 4QT machines are calculated with FEM by inserting sinusoidal currents in the slots in Figure 5.14 defined by equation (5.16). When calculating the Stator inductances the inner rotor slot currents are set to zero and vice versa.

$$\begin{cases} i_A = \hat{i} \cos(\omega t) \\ i_B = i_C = -\frac{1}{2} \hat{i} \cos(\omega t) \end{cases} \quad (5.16)$$

Using FEM the winding flux linkage  $\Psi$  can be obtain, then the d- and q-axis inductance can be calculated using equation (5.17) for the two different geometries presented in Figure 5.14.

$$\begin{cases} L_d = \frac{\Psi_A}{i_A} \Big|_{d\text{-axis}} \\ L_q = \frac{\Psi_A}{i_A} \Big|_{q\text{-axis}} \end{cases} \quad (5.17)$$

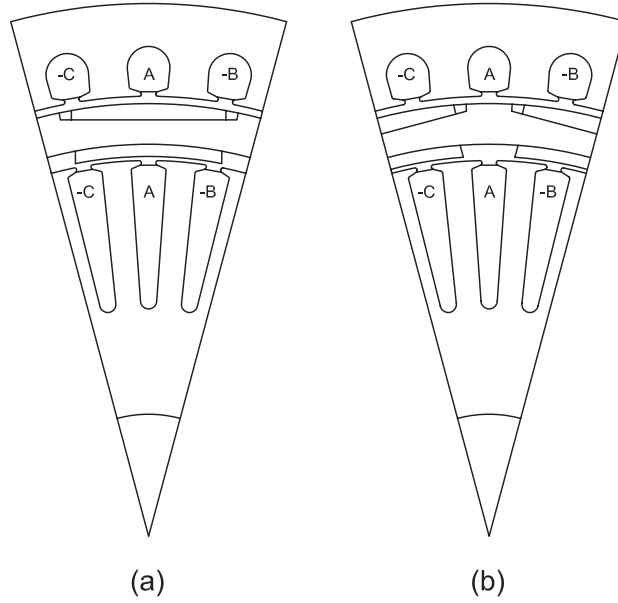


Fig. 5.14 Model for (a)  $q$ -axis, (b)  $d$ -axis inductance calculation.

The FEM simulated inductance values are corrected with the skewing factor from equation (5.15) and then the analytical end winding inductance  $6.9 \mu\text{H}$  for the Stator and  $24.2 \mu\text{H}$  for the DRM from [35], which are added to the FEM inductance values. The results are presented Figure 5.15.

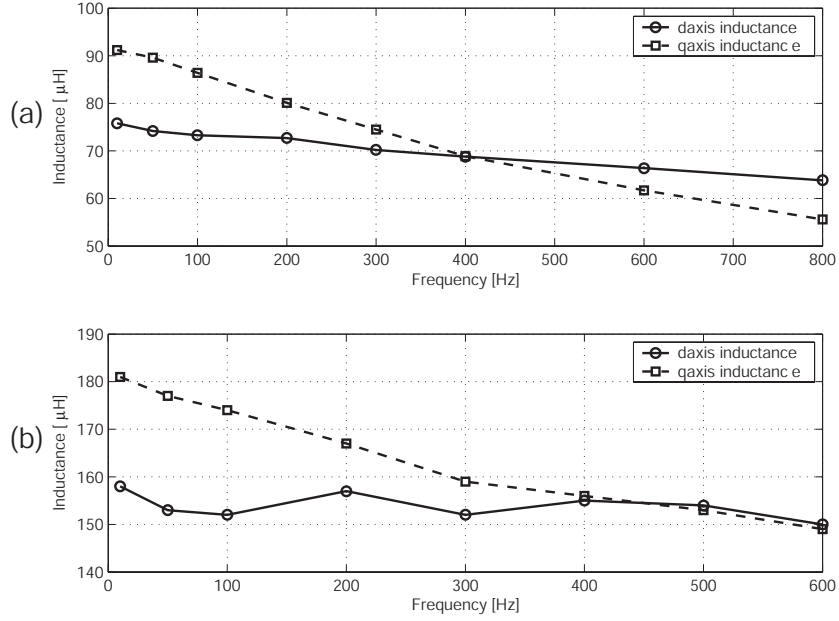


Fig. 5.15 FEM calculated (a) Stator and (b) DRM, d- and q-axis inductances.

## 5.5 Field weakening

The field weakening operation is essential for the Stator, therefore its field weakening capability has been investigated both analytically and by the use of the time stepping FEM, [14]. At field weakening in the constant volt-ampere region the  $i_d$  and  $i_q$  currents need to be known to calculate the torque. Solving equation (5.18) to equation (5.20) suggested in [16] makes it possible to calculate the field-weakening region of the stator analytically.

$$t = \lambda_m i_q + (l_d - l_q) i_q i_d \quad (5.18)$$

$$\left(\frac{u}{\omega}\right)^2 = (\lambda_m + l_d i_d)^2 + (l_q i_q)^2 \quad (5.19)$$

$$i^2 = i_d^2 + i_q^2 \quad (5.20)$$

The inductances  $l_d$  and  $l_q$  are the d- and q- axis inductances,  $i_d$  and  $i_q$  are the d- and q- axis currents, and  $\lambda_m$  is the PM flux linkage. In the Stator case there is a

salient-rotor design and the d- and q- axis inductances are not equal. This gives a reluctance torque contribution from the last term in equation (5.18). Figure 5.16 shows the field weakening torque for the Stator in p.u. for both the analytical calculations and the time stepping FEM calculations. The FEM field weakening calculations were done with an external circuit connected to the FEM model. The circuit consisted of the end winding inductances and resistances, which were calculated analytically and included in the circuit. The motor was assumed to be fed from sinusoidal voltage sources. The field weakening control strategy was made with a simple voltage/frequency control. It should be possible to simulate the control using the vector control method which will give more torque from the machine.

The results of these simulations show that the required wide field-weakening range of the Stator can be achieved. The stator is only required to utilize field-weakening up to two times the base speed of 4000rpm. At double base speed, that is 8000rpm, the maximum torque becomes about 45 % of the nominal torque for the Stator machine.

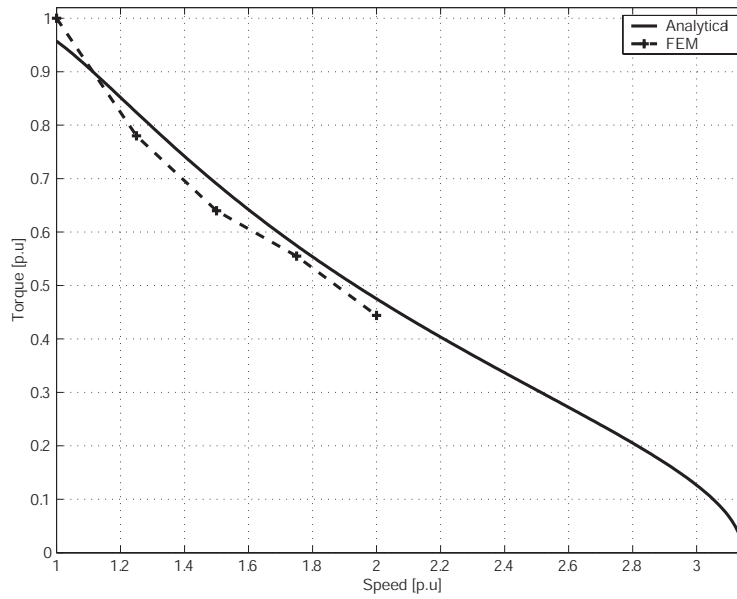


Fig. 5.16 Field weakening torque for the stator in (p.u).

## 5.6 Mechanical design

### 5.6.1 Bandage

The outer magnets cannot be held in place with glue only. Glue is not sufficient to withstand the large centrifugal forces at maximum speed that will attempt to throw the magnets loose. If this failure occurred, the loose magnet can cause extensive damage to both the rotor and the stator of a PM machine. To avoid this scenario a bandage is wound around the rotor to hold the magnets against the centrifugal forces.

The bandage thickness is dependent on the weight of the magnets, the maximum rotating speed and the radius of the rotor. The centrifugal force and the magnet design determine the thickness of the bandage.

The bandage was obtained by applying five layers of Toray T1000GB carbon fibre mixed with epoxy resin, this gave a bandage thickness of about 1 mm. After bandaging the rotor was baked in an oven for 6h in 100 °C and 8h in 130 °C. The maximum allowable continuous temperature of the magnets is 150 °C [46]. Thus there is sufficient margin to avoid damage to the magnets from too high temperatures during the baking process. The bandaging was performed at Sicomp AB.

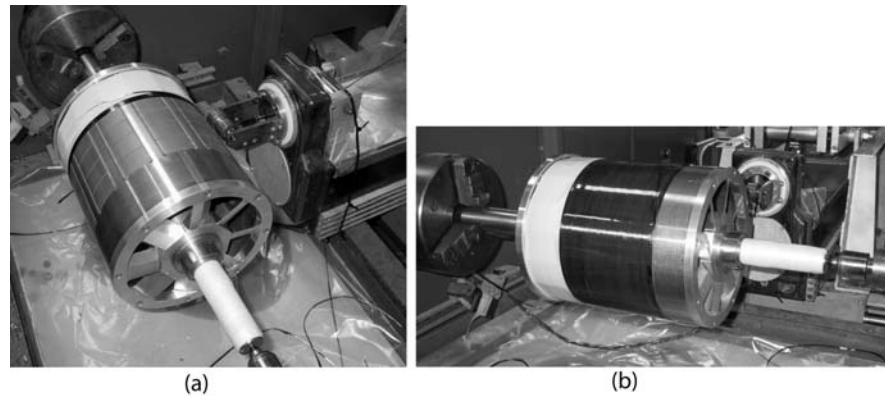


*Fig. 5.17 (a) Start of bandaging, (b) end of bandaging.*

## **5.7 Redesign after inner rotor failure**

After extensive testing at high load on both machines the inner winding overheated and the insulation failed, see Figure 5.18. Due to this, a redesign of the prototype machine was done. The redesign can be divided into two different steps:

- Repair and replacement of the laminations and winding of the inner rotor
- Improvement of the cooling of the inner rotor

The new laminations were manufactured exactly the same as the first ones. One improvement that could have been made was the use of shallower rotor slots but this was not possible as the required copper area and consequently the required slot area was the same. For an inner rotor design, the area increase of the slot is smaller as the slot grows deeper, which inevitably leads to deep slots. The winding was redesigned and divided into a two layer winding to get a more compact and easy to wind solution. The winding configurations are shown in Figure 5.19 where the turns numbers 1 and 2 in the first slot in the lower parts of the figure are led to the positions 4 and 5 for the second slot in the same phase. Similarly turn numbers 1, 2 and 3 in the second slot are led to positions numbers 3, 4, 5 in the third slot.

To improve the cooling of the machine the internal cooling system for the inner rotor which consisted of a circulating air flow, driven by two shaft mounted fans, was removed. This was due to the fact that the fans actually never drove any air flow through the machines. The new design relies on a separate external fan that forces outer air through new openings in the end shields at both sides of the 4QT machine.



*Fig. 5.18 Inner rotor after failure.*

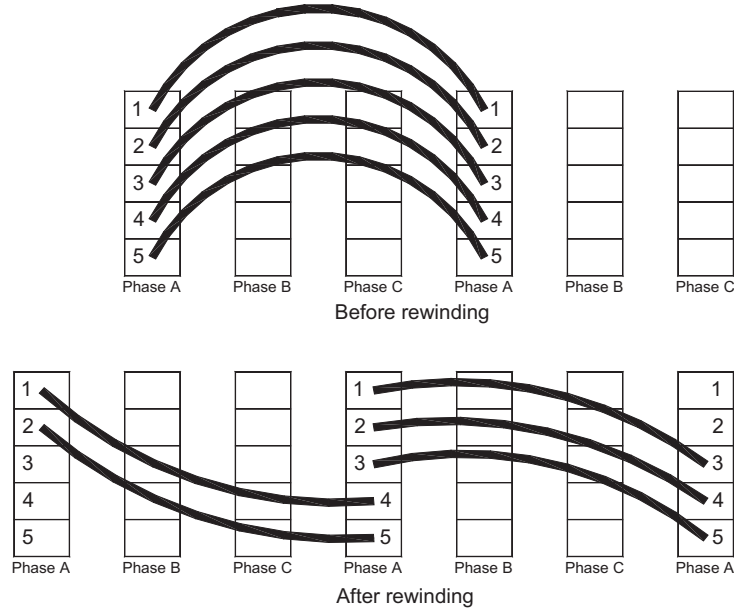


Fig. 5.19 Winding arrangements of the inner rotor, both before and after the rewinding.

## 5.8 Cooling

The cooling of the 4QT machine was solved by using water cooling for the Stator machine and air cooling for the inner rotor. The initial idea to cool the inner rotor was to use shaft mounted fans to drive a circulating air flow through the airgap and the axial holes in the inner rotor, then up into the heat sink which is integrated in the aluminium housing, see Figure 5.20 and Figure 5.21.

The Stator cooling consists of water flowing through the Stator housing, Figure 5.21. The water cooled housing cools the active parts of the Stator through conduction.

The two cooling methods had some advantages and disadvantages. First the advantages:

- The internal air cooling system creates a sealed machine which is desirable for automotive application.
- The water cooling is effective and makes it possible to overload the Stator.

The following are the disadvantages:

- The circulating air flow driven by the shaft mounted fan did not perform well at low speed, which is critical especially at high torque loads that require high current and thus cause high copper losses.
- Design errors in the fan mounting. The axial fan was mounted too close to the end windings and the outer end shield which gave limited space before and after the fan, thus limiting the pumping effect of the fan.

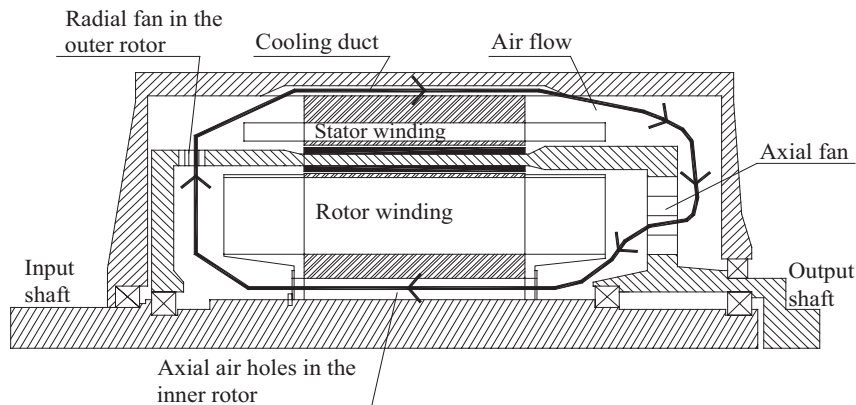


*Fig. 5.20 Old air cooling system of the inner rotor in the 4QT.*

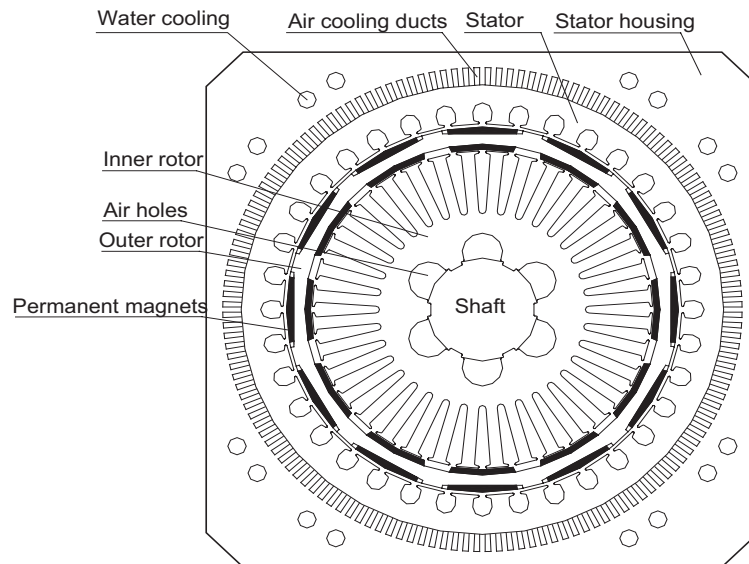


*Fig. 5.21 Radial cross-section view of the 4QT, showing the water and air cooling channels.*



After the devastating failure of the 4QT, see section 5.7, the inner rotor was re-wound and the cooling system of the inner rotor redesigned. To improve the cooling effect of the inner rotor a forced air cooling system driven by an external fan was used. The fan was mounted on the top of the 4QT, Figure 5.22. This fan pressed the cooling air through the new axial holes in the end shields and through the 4QT, cooling the inner part, and out through the other axial end, Figure 5.23.

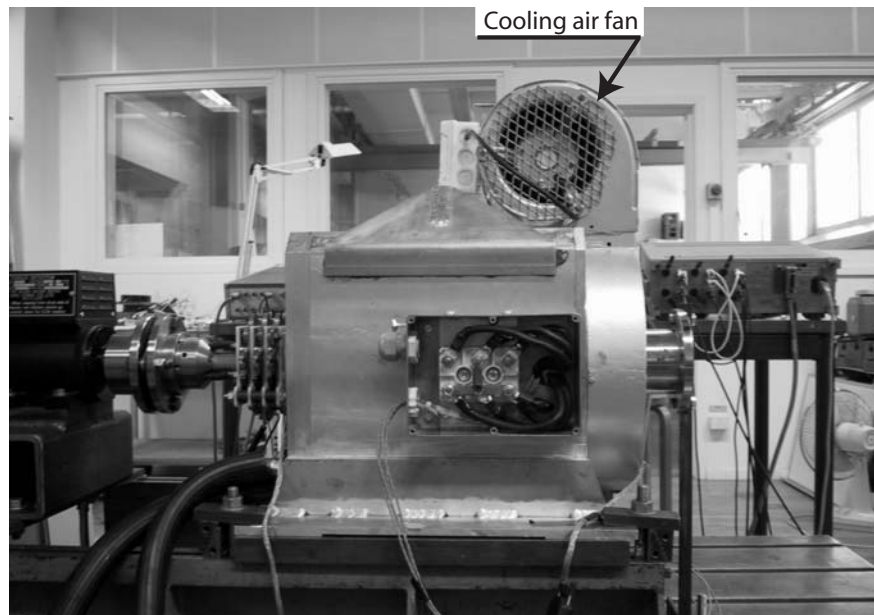


*Fig. 5.22 4QT prototype with mounted external cooling fan.*

The external fan gave an air flow independent of the rotational speed of the shafts, this is the solution recommended for automotive applications. The drawback of this method is that it needs external air so that the machine is no longer hermetically sealed. This can be solved by leading the cooling air from the fan through the 4QT into a heat sink for cooling and then back to the fan and again into the 4QT in a closed circuit.

The cooling and thermal modelling of the 4QT machine are described in more detail in chapter 7.

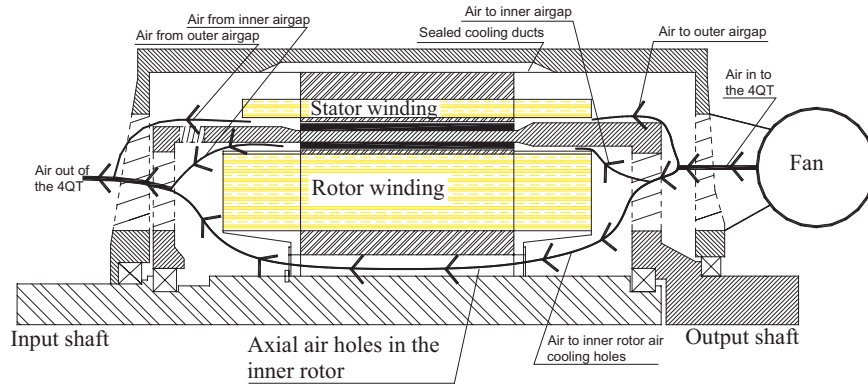


Fig. 5.23 New forced air cooling system for the inner rotor of the 4QT prototype machine.

## 5.9 Prototype layout

The prototype was constructed with the different parts shown in Figure 5.24.

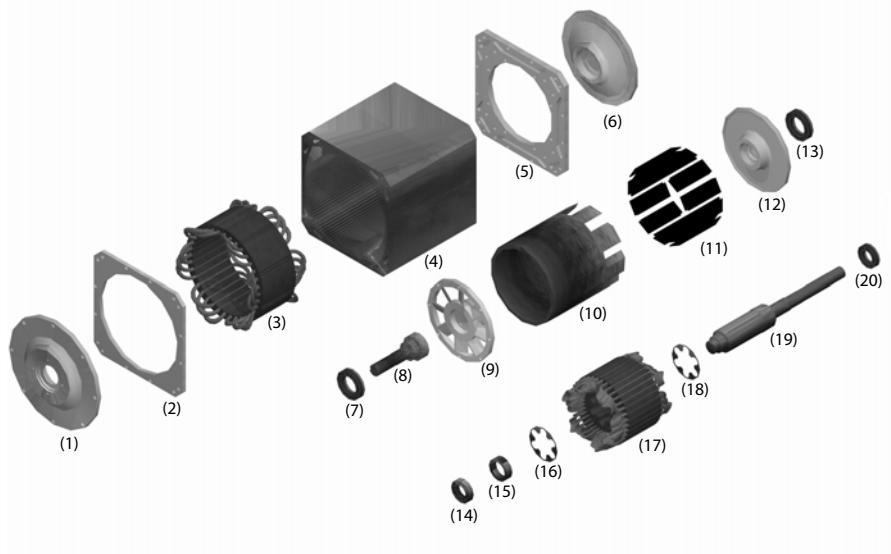
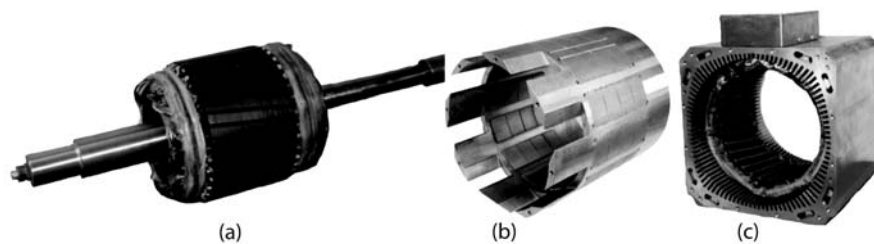


Fig. 5.24 Prototype layout.

In Figure 5.24 the different parts are:

1. End shield to support the output shaft
2. End shield with water cooling channels
3. Stator with laminations and windings
4. Housing in Aluminium, includes water and air cooling channels
5. End shield with water cooling channels
6. End shield to support the input shaft
7. Bearing
8. Output shaft from the outer rotor
9. End shield with axial fan for the outer rotor. Also supports the end of the inner rotor shaft(19) via bearing(14).
10. Outer rotor, with splines for magnets and integrated radial fan
11. Magnets
12. End shield for the outer rotor, support bearing(13) against the outer end shield(6) and bearing(20) against the inner rotor(19)
13. Bearing
14. Bearing
15. Nut to hold the inner rotor laminations by fastening through threads made at the end of the inner rotor shaft(19)
16. Washer between the nut(15) and the inner rotor(17)
17. Inner rotor with laminations and winding
18. Washer between the inner rotor(17) and the end of the axial tracks in the shaft(19) for the laminations.
19. Input shaft from ICE end
20. Bearing

Pictures of the assembled inner rotor, the outer rotor and the stator with the housing are shown in Figure 5.25.



*Fig. 5.25 (a) Inner rotor, (b) Outer rotor and (c) Stator with housing.*

## **5.10 Conclusions from the prototype design**

A 4QT prototype dimensioned for a medium size passenger car has been designed and manufactured. The first design had insufficient cooling of the inner rotor which led to overheated inner rotor windings.

When repairing the prototype, modifications of the inner rotor winding and to the cooling system were done and thus a forced air cooling system was installed.

Design criteria as back-EMF, cogging, torque ripple, winding resistance and inductance have been investigated both with analytic methods and by FEM. Initial measurements shows good agreement with tested values on the manufactured prototype.

## 6 Prototype testing

The 4QT prototype has been tested mostly in generator mode and the resistances, inductances, losses, efficiency and the thermal behaviour of the two separate machines, the Stator and the DRM has been tested separately and in combined operation tests. The Stator efficiency has been investigated with calorimetric measurements and for the DRM the slip ring friction losses has been measured.

### 6.1 Test setup for generator test

During the generator tests the temperatures in the machine, the cooling water flow and temperature, electrical output power, voltage, current, torque and speed were measured. The load power was dissipated into two resistive load banks via two passive rectifiers, Figure 6.2, one for each winding. This setup was used to simplify the adjustment of the resistance when loading the machine. If the rectifiers were not used three separate resistors would have been used for each winding which gives a total of six resistors each one able to handle 10kW of electric load at a current of 100 A (RMS). Using rectifiers decreased the amount of resistors but of course increased each resistor size to 30kW.

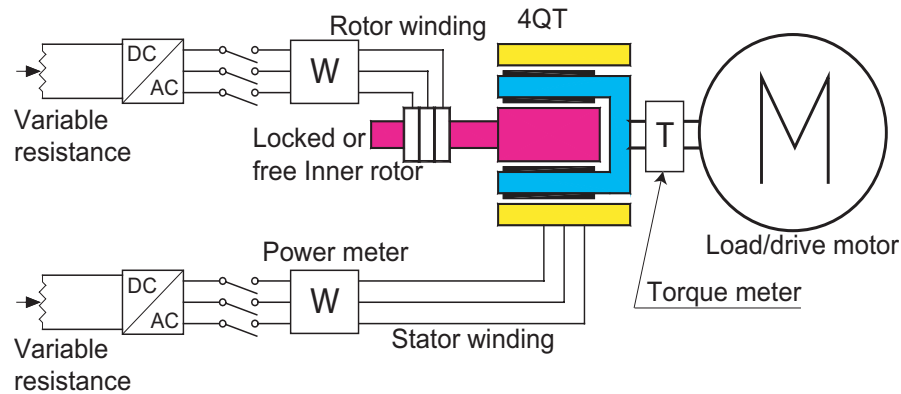
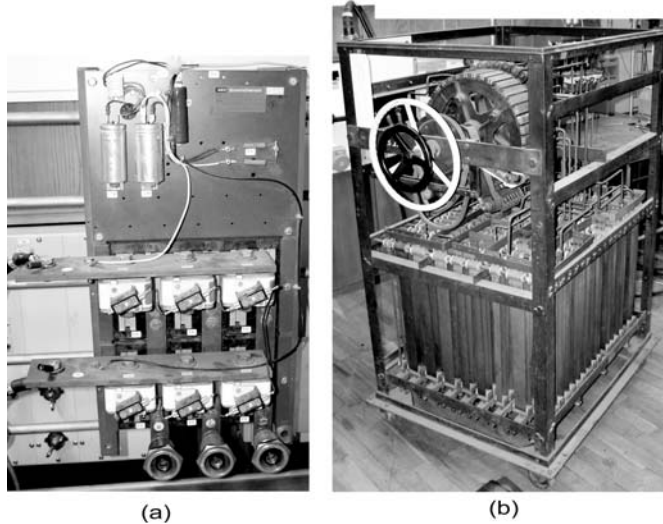


Fig. 6.1 Generator test setup.

The inner rotor was either locked or freely rotating, dependent of the type of load test. When only testing the Stator machine it is desirable to let the inner rotor follow the outer rotor at synchronous speed to avoid extra iron losses in the inner rotor that should have otherwise been included in the Stator machine measurements. Loading both machines requires a locked inner rotor which makes it possible to apply load torque to the inner rotor as well.



*Fig. 6.2 (a) Six pulse diode-bridge rectifier (b) Resistance bank, used for the generator tests.*

## **6.2 Placement of the measurement sensors**

To measure the temperatures in the 4QT, the cooling water and the ambient environment, different temperature sensors were used. These sensors were connected to a computer to record the temperatures during the tests.

### **6.2.1 Water temperature sensors**

The water inlet and outlet temperatures as well as the water flow were measured with temperature sensors and a flow sensor placed on an aluminium plate as shown in Figure 6.3. The flow sensor was fed with 15 V DC and the signals were read through a 9pin D-sub contact to a data acquisition unit<sup>1</sup> and then saved in a computer through a GPIB bus.

The water flow was measured with a flow sensor<sup>2</sup>, Figure 6.4. The sensor output signal was 5700pulses/litre in a square wave form and has an inaccuracy of  $\pm 1\%$ . The frequency was measured by the data acquisition unit<sup>1</sup> and when the measured frequency was transferred to a computer the water flow in litre/min

1. HP 34970A Data acquisition/Switch unit
2. Swissflow SF-800-B

was calculated. The water temperature was measured using PT-100 sensors inserted into a holder as shown in Figure 6.5. A rectangular piece of plastic was inserted before the sensor in order to create a more turbulent flow over the sensor and thus avoiding a temperature profile over the sensor.

The water temperature and flow module, Figure 6.3, made it possible to measure the calorimetric losses of the 4QT machine through the cooling water. Using equation (6.1) it is possible to calculate the total calorimetric losses.

$$\dot{q} = \dot{m}C_p\Delta T \quad (6.1)$$

where the heat flow is  $\dot{q}$ , the mass flow  $\dot{m}$ , the specific heat coefficient for water  $C_p$ , and the temperature difference between the inlet and outlet water  $\Delta T$ .

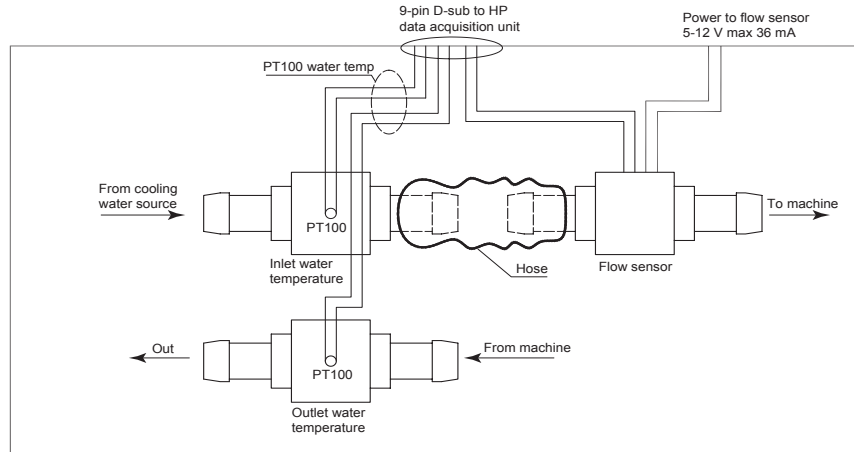


Fig. 6.3 Sensor setup for water flow and inlet/outlet water temperature.

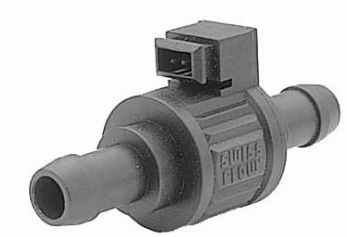
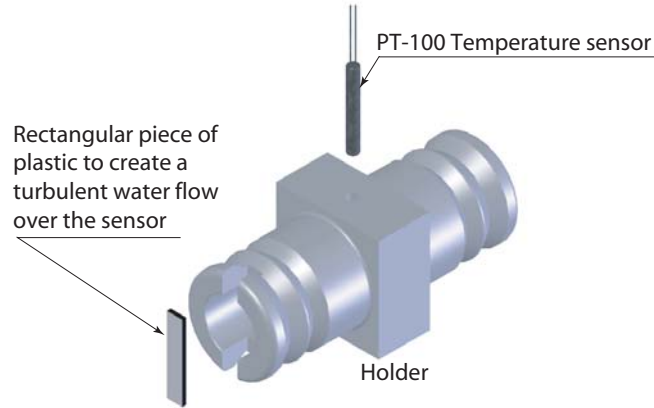


Fig. 6.4 Flow sensor Swissflow SF-800-B.



*Fig. 6.5 Water temperature measure component.*

### **6.2.2 Sensors in the 4QT**

In the 4QT there are seven temperature sensors, three in the inner rotor and four in the Stator and housing. The three sensors in the inner rotor are mounted on the winding, one at each end winding and one in a slot in the middle of the rotor. The Stator temperature sensors are mounted, one on the heat sink, one in the air, one on the endwinding and one in the stator slot.

All temperature sensors in the 4QT Stator and housing are thermocouples of T-type while the sensors in the inner rotor are of PT-100 type. The sensor placement are shown in Figure 6.6 to Figure 6.8 for the inner rotor, the Stator and the housing. The temperature sensors in the end windings and the slots of the inner rotor and Stator winding are placed inside the windings before vacuum pressure impregnation. The temperature sensors on the housing are for the heat sink glued to the aluminium heat sink fin and for the air channel freely placed in one of the air cooling channels in the heat sink.



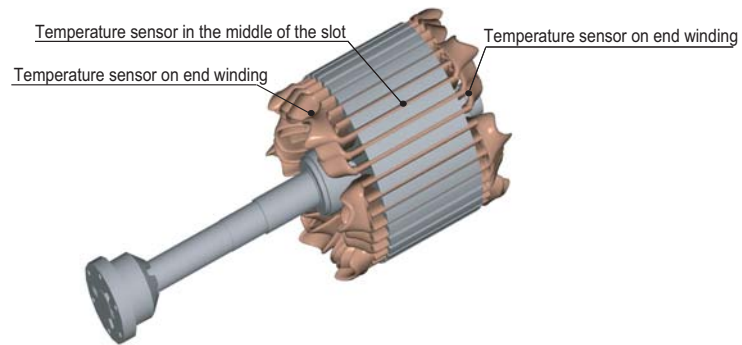


*Fig. 6.6 Temperature sensor placement in the inner rotor.*

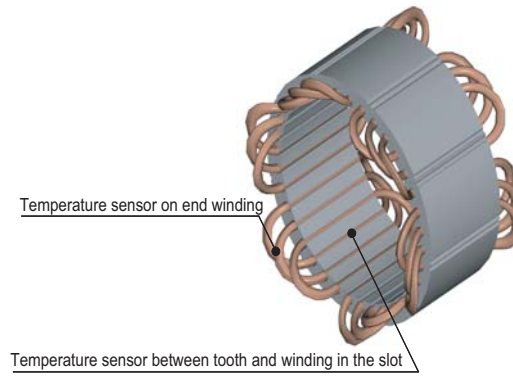


*Fig. 6.7 Temperature sensor placement in the Stator.*

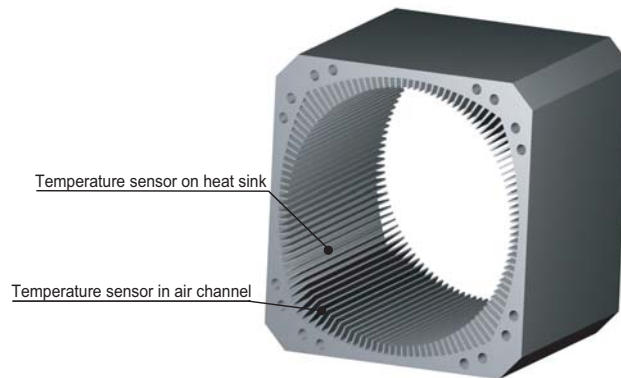


*Fig. 6.8 Temperature sensor placement in the housing.*

## 6.3 Generator tests

The 4QT machine was loaded as a generator to investigate its efficiency and thermal behaviour. The thermal issues of the 4QT, especially the temperature in the inner rotor windings are of great importance and critical to the design of the system.

### 6.3.1 Stator test

The Stator machine was tested as a generator prior to and after the failure of the inner rotor. Table 6.1 shows the different evaluated load steps, the first four before the failure and the last four after the failure. The first four had locked inner rotor which gave extra iron losses in the inner rotor. The last four tests were made with the inner rotor rotating freely and synchronously with the outer rotor. This gives negligible iron losses in the inner rotor since the magnets and the inner rotor lamination rotate at same speed. The bearing friction between the rotors can also be neglected; since the bearings are mounted between the rotors their relative speed is zero.

*Table 6.1 Load steps at Stator loading.*

Test number	Speed [rpm]	Load [Nm]	Test method	4QT design
T1	4000	29	Locked inner rotor	First
T2	4000	55	Locked inner rotor	First
T3	4000	62	Locked inner rotor	First
T4	4000	71	Locked inner rotor	First
T5	1500	30	Loose inner rotor	Second
T6	3000	54	Loose inner rotor	Second
T7	4000	67	Loose inner rotor	Second
T8	4000	78	Loose inner rotor	Second

The temperature increase from the inlet temp of the cooling water to the end winding and the slots of the Stator are shown in Figure 6.9 and Figure 6.10. Figure 6.11 shows the temperature increase of the end windings and slots at different loads for the two different designs. The second design had a smaller temperature rise than the first design, due to mainly two reasons. Firstly, in the

second test forced air cooling was used for the inner rotor machine instead of the internal air cooling system; secondly, the first test was carried out with a locked inner rotor causing iron and friction losses in the inner rotor which did not exist in the second test.

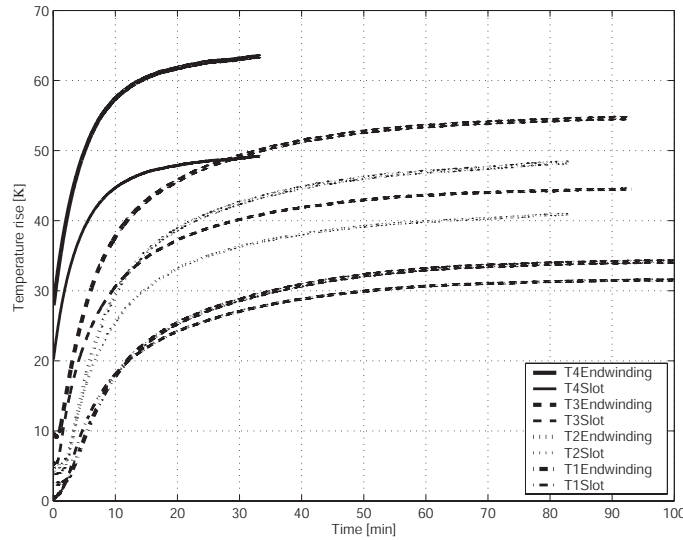


Fig. 6.9 Temperature rises in the Stator during load tests with the old designs before the inner rotor failure, see test T1-T4 in Table 6.1.

As can be seen in Figure 6.11 the cooling of the new design is more effective due to the lower temperatures, and since there were no changes made to the Stator during the repair of the 4QT prototype the decrease in temperature can be mainly related to the improved cooling system. The changes in the cooling system both increased the cooling air speed and decreased the cooling air temperature thus increasing the cooling efficiency of the machine.

Comparing the temperatures of the two designs in Table 6.2 it can be observed that there is a temperature decrease of 38.7% for the Stator end winding and a temperature decrease of 30.6% for the Stator winding in the slot. The larger decrease for the end winding can be explained by the increased efficiency of the forced air cooling on the exposed end windings as compared to the winding in the slot which is buried in the laminations.

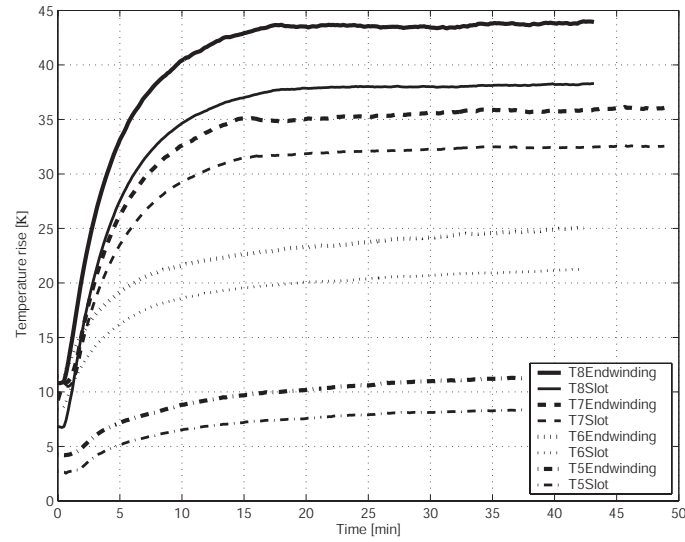


Fig. 6.10 Temperature rises in the Stator during load tests with the new designs after the inner rotor failure, see test T5-T8 in Table 6.1.

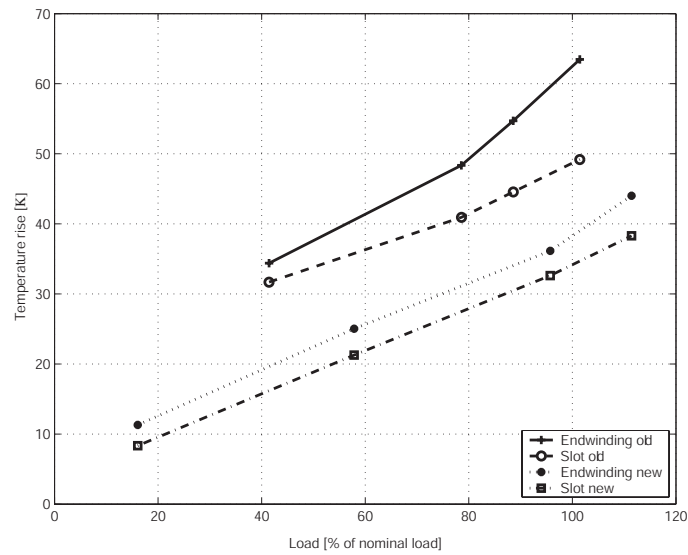


Fig. 6.11 Temperature rises at different loads with the old and new designs.

*Table 6.2 Temperature rises at the Stator end winding and the Stator winding in a slot for both the old and new designs of the 4QT at full load.*

	Temperature rise [K]			
	Old design		New design	
Load [%]	End winding	Slot	End winding	Slot
100	62	49	38	34

### 6.3.2 DRM test

The DRM was tested in the same way as the Stator before and after the failure of the 4QT machine. Table 6.3 shows the test operation points used when loading the DRM in generator mode with locked inner rotor and the outer rotor connected to a load machine. When using this method the Stator iron losses are included in the total losses. To measure the efficiency of the DRM the Stator iron losses has to be separated from the total losses.

Figure 6.12 shows the inner rotor temperature for no-load operation at nominal speed. The temperature of the inner rotor winding reaches 92 °C at steady-state. This temperature is on the air outlet side of the forced air cooling. At the air inlet side of the 4QT prototype the end winding temperature becomes approximately 13 °C lower.

When rewinding the inner rotor, temperature sensors were mounted in the winding, which made it possible to evaluate the influence of DRM load current on the inner rotor temperature. Figure 6.13 presents the temperature in the inner rotor versus the DRM load current. The actual tests were limited to 64 A (RMS) and 115 °C. If the temperature is extrapolated up to the rated current of 100 A (RMS) the temperature in the winding will be about 150 °C. The winding is of temperature class F and thus withstands a hot spot temperature of 155 °C at continuous operation. To be able to load the inner rotor at nominal load it has to be cooled in a more effective way, for example by using a more powerful fan. But, since the required life time in an automotive application normally is low compared to an industrial life time of an electrical machine, it is possible to run the machine at a higher temperature compared to a conventional industrial motor.

Table 6.3 Load points for the DRM.

Speed [rpm]	Torque [Nm]	Voltage [V]	Current [A]	Inner rotor steady- state maximum temperature [°C]
3000 <sup>a</sup>	-	183.1	-	92
3000 <sup>b</sup>	57.2	165.2	59.7	-
3000	26.75	182.9	22.8	94
3000	45.75	177.9	44.9	104
3000	65.4	173.8	64	115.7

- a. No-load test with locked inner rotor  
b. Test of the first inner rotor was without temperature sensors

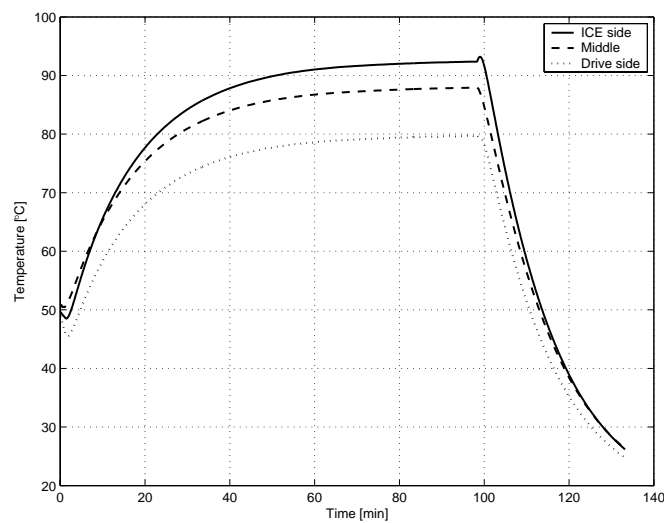


Fig. 6.12 Inner rotor temperatures, no-load test at 3000 rpm.

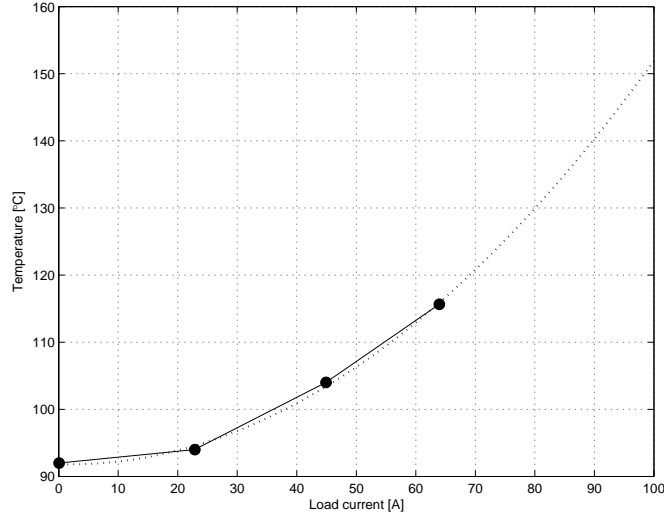


Fig. 6.13 Inner rotor temperature versus load current.

It is possible to estimate the magnet temperature rise from the difference in induced voltage at no-load if the magnet temperature coefficient for the used magnets is known. In the 4QT prototype VACODYM 655HR magnets were used with a temperature coefficient of  $-0.090\%/^{\circ}\text{C}$  for the remanence flux.

The induced voltage is dependent on the flux density from the magnets. When the magnets are heated the remanent flux density in the magnets are reduced and thus the flux linkage and the induced voltage will be reduced. This means that the temperature can be determined i.e. from the measured induced voltage.

At no-load and a cold machine the induced voltage was 185.6V and when running the machine until thermal steady-state, i.e. the first point in Table 6.3, the induced voltage becomes 183.1V. This gives a magnets temperature rise of  $15^{\circ}\text{C}$ . Assuming an ambient temperature of about  $25^{\circ}\text{C}$  the magnet temperature becomes  $40^{\circ}\text{C}$  at steady-state no-load condition.

### 6.3.3 Combined tests Stator and DRM

When loading both the Stator and the DRM the inner rotor is locked and the two windings are each connected to a rectifier and a resistive load bank, see Figure 6.1. The drive motor must supply the load torque for both machines, which at nominal torque becomes 170Nm. The speeds at this tests were the same for both machines because the magnets for the machines are mounted on the common outer rotor, which limits the flexibility of the combined load test for the

two machines. Table 6.4 shows the load points for the combined tests of the Stator and the DRM.

Table 6.4 Load points for combined tests of the Stator and DRM before the failure.

Speed [rpm]	Torque Stator [Nm]	Torque DRM [Nm]	Power Stator [kW]	Power DRM [kW]	Power total [kW]	Efficiency [%]
3000	58.5	90.5	15.4	35.6	41.8	95
3000	51	83	13.4	24.1	37.5	95.7
3000	46	76	11.6	21.6	33.2	96.9
3000	-	-	8.5	16.8	25.3	95.8

The DRM winding temperature was calculated from the increase in resistance of the rotor winding from the start value to the thermal steady-state value for each specific test. The load points of the tests are the same as those shown in Table 6.4. The results of the temperature increase from the water inlet temperature of 7.7°C to the inner rotor winding temperature are shown in Table 6.5.

Table 6.5 Temperature of the inner rotor windings at different load conditions before the failure. Stator cooling water inlet temperature was 7.7°C.

	Stator	Inner rotor winding	
Speed [rpm]	Current [A] (RMS)	Current [A] (RMS)	Temperature steady-state [°C]
3000	44	61	64
3000	62	81	73
3000	74	95	85
3000	87	109	102

The temperatures in Table 6.5 are the mean value of the temperature in the inner rotor winding since they are based on calculations of the winding resistance increase. It is possible, and also proven, that hot spots did exist in the winding. This is based on the fact that the windings actually failed due to overheating at higher load than the last row in Table 6.5, though the mean temperature was not to high



for the used class F insulation.

## 6.4 No-load losses

The no-load losses were measured at motor operation fed via a rotating converter and at generator mode when rotating the 4QT with a DC motor. The no-load losses were measured both for the Stator and the DRM.

### 6.4.1 Stator no-load losses

The no load losses for the Stator were measured from 500 to 4000 rpm. The measurements were carried out with a power meter for the motor operation, torque and speed sensors for the generator operation and by calorimetric measurement. The Stator no-load losses are shown in Figure 6.14. The losses from generator and motor tests were done for a cold machine while the calorimetric measurement was done at steady-state temperature, thus with a warmer machine. The no-load losses decreased therefore by 200 W. The motor tests were only done at 500 and 600 rpm since the Stator was operated as a motor via a rotating converter with a maximum frequency of 60 Hz. The calorimetric measurement was only made at one operation point, which was at nominal speed 4000 rpm.

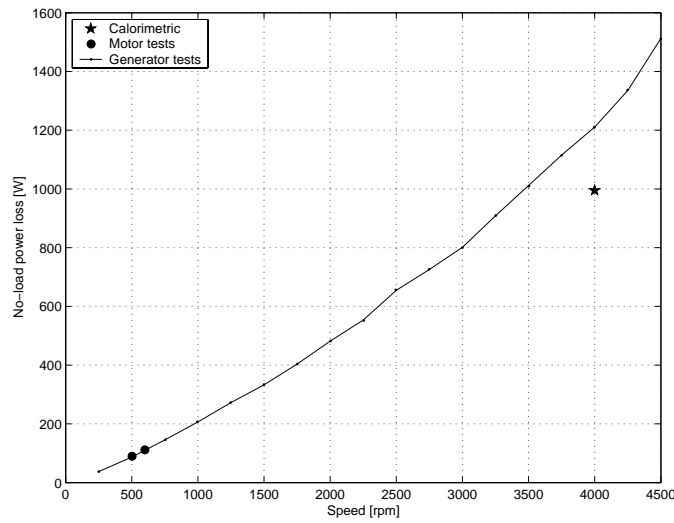


Fig. 6.14 Stator no-load losses from calorimetric, motor and generator tests.

### 6.4.2 DRM no-load losses

The DRM no-load losses were measured with a digital torque meter<sup>1</sup> in combination with a torque sensor<sup>2</sup> and the losses were derived from the speed and torque measurements. The no-load losses were measured both with and without the brushes mounted in the slip ring unit, see Figure 6.15, which makes it possible to separate the slipring friction losses, see Figure 6.16.

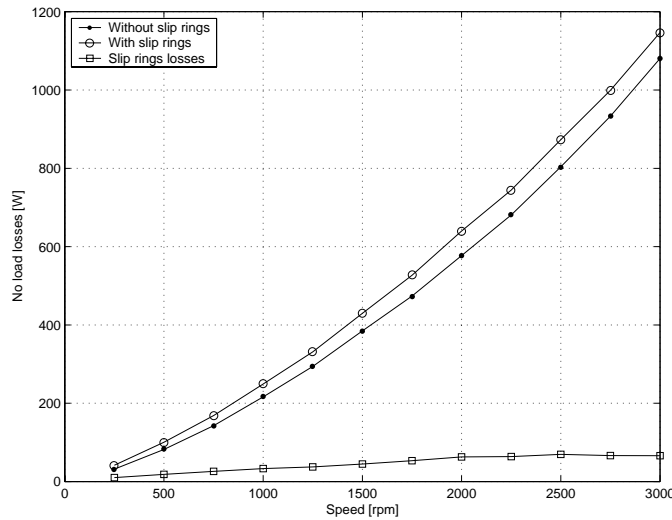


Fig. 6.15 DRM no-load losses, with and without the slipring friction losses, versus speed.

As presented in Figure 6.15 the slipring losses are small compared to the conventional iron and friction losses in electrical machines for the 4QT prototype.

## 6.5 Friction losses in the slipring units

The friction losses of the sliprings had an minor impact on the efficiency measurements. Even though in the Stator test, where the slipring friction should not be included in the efficiency measurements it had to be separated. When measuring the Stator efficiency the Stator machine is loaded at different loads for different speeds and torques. To avoid iron losses in the inner rotor lamination during the Stator test the inner rotor can be made to rotate at a speed that is syn-

1. Oni Sokki TS-800B
2. Oni Sokki SS-200

chronous with the outer rotor. This also means that the sliprings are rotating and producing friction losses that should not be included in the Stator efficiency measurements.

To measure the slipring power losses the torque and speed of the machine at no-load were measured both with the brushes on the sliprings, and with the brushes lifted from the slipring surfaces. The difference between these two measurements gives the slipring friction losses which are shown in Figure 6.16. The values are mean values from a series of measurements, since the slipring friction torque is small compared to the torque from the iron losses, and the subtraction of these two torques has low accuracy. According to measurements on slipring units done in [25],[26] the friction losses of a slipring is, as a first approximation (neglecting temperature and current effects etc.), proportional to the surface speed of the sliprings. As seen in Figure 6.16 the friction losses are small compared to the iron losses and has a general tendency of increasing proportional to the speed. The linear curve in Figure 6.16 is used to correct the efficiency measurements of the Stator machine.

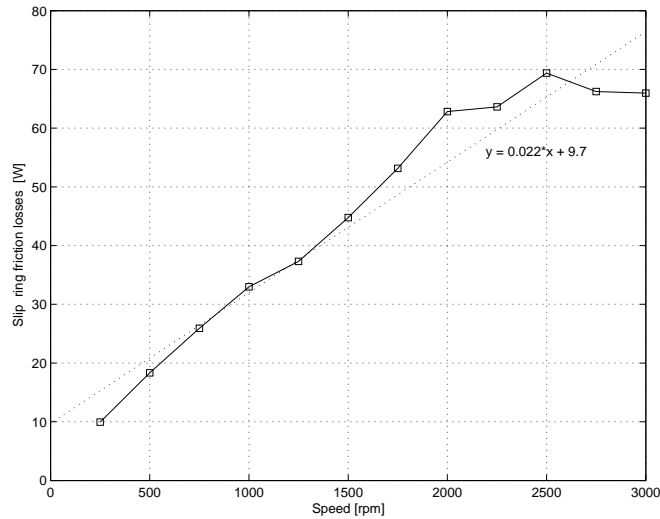


Fig. 6.16 Measured slipring friction losses versus speed.

## 6.6 Efficiency tests

The efficiency of the 4QT prototype was measured at generator mode for speed and torque up to nominal load. The efficiency was calculated by measuring the input torque and speed and the output three phase power, then calculating the efficiency according to equation (6.2):

$$\eta = \frac{P_{out}}{P_{in}} \quad (6.2)$$

where  $\eta$  is the efficiency,  $P_{in}$  is the mechanical measured input power and  $P_{out}$  the three phase output power measured by a power meter<sup>1</sup>. During the tests the 4QT was electrically loaded by a resistive load bank via a rectifier, Figure 6.2.

The efficiencies of the two separate machines were plotted into efficiency maps as a function of operating speed and torque and compared to analytical efficiency calculations from [23].

### 6.6.1 Stator efficiency test

The Stator efficiency was measured at speeds up to 4000rpm and torque up to 70Nm, i.e. base speed and base torque. The results of the efficiency measurements are presented in Figure 6.17.

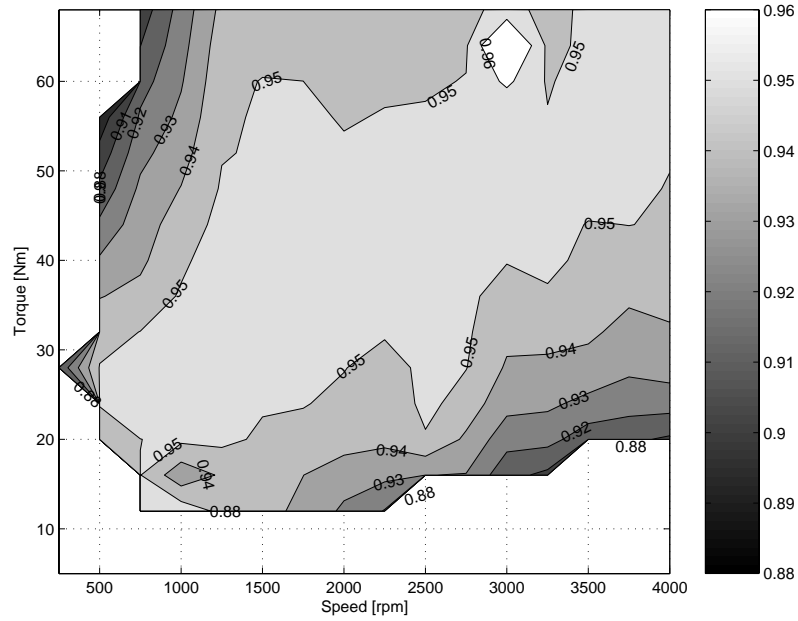
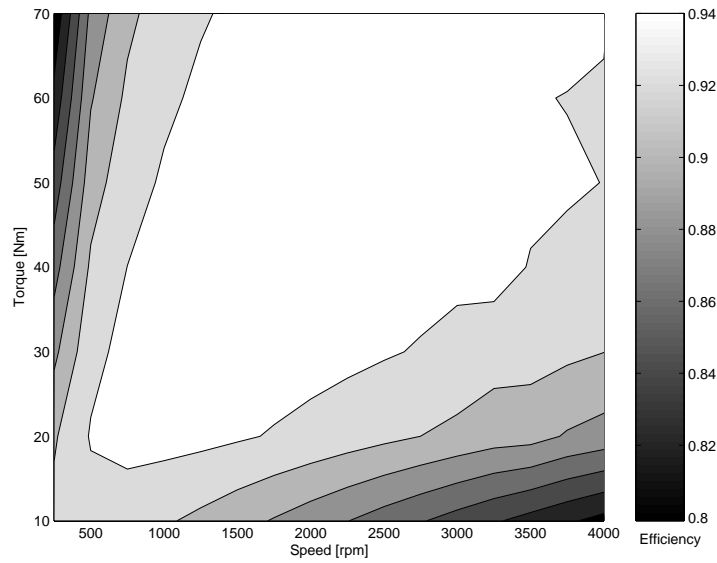


Fig. 6.17 Measured Stator efficiency map based on input and output power.

Comparing the measured efficiency for the Stator with the calculated efficiency from [23] in Figure 6.18 there is a difference of about 1 % in favour of the meas-

1. Yokogawa 1030M

ured values. The basic shapes of the efficiency maps are approximately the same with the highest efficiency in the centre of the map. Comparing the analytical calculated efficiency with the calorimetric measured values of 93.4% at nominal speed and torque (see section 6.7) shows good agreement between the measured values and the theoretical values.



*Fig. 6.18 Calculated efficiency of the Stator machine from the licentiate thesis [23].*

### 6.6.2 DRM efficiency test

The DRM efficiency was measured for speeds up to 3000rpm and torques up to 100Nm, i.e. base speed and base torque. The measured efficiency map of the DRM is presented in Figure 6.19 and the calculated efficiency map from [23] is presented in Figure 6.20. The measured and calculated efficiency maps shows similar trends and the maximum value differs by approximately one percent.

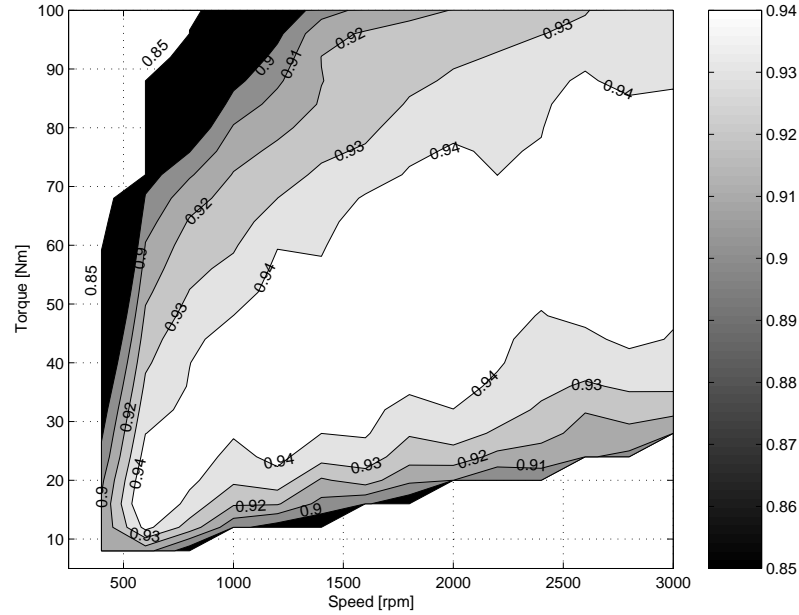


Fig. 6.19 Measured DRM efficiency map.

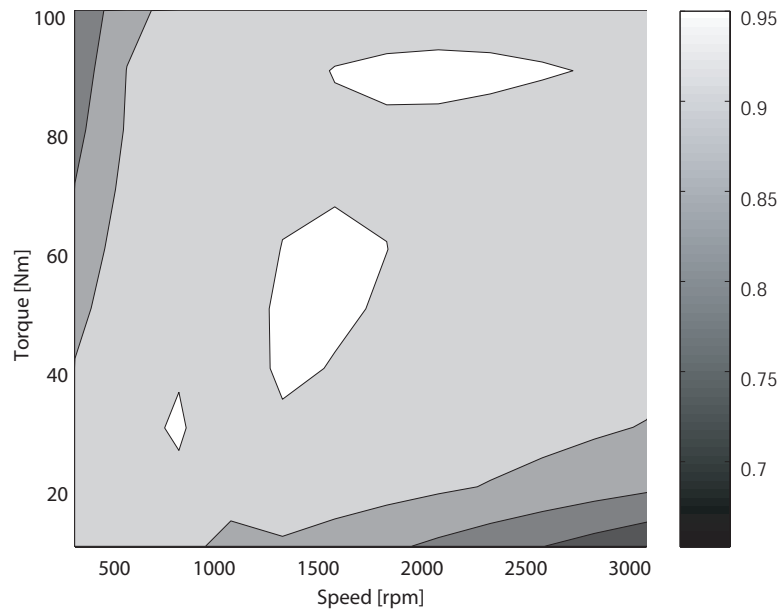
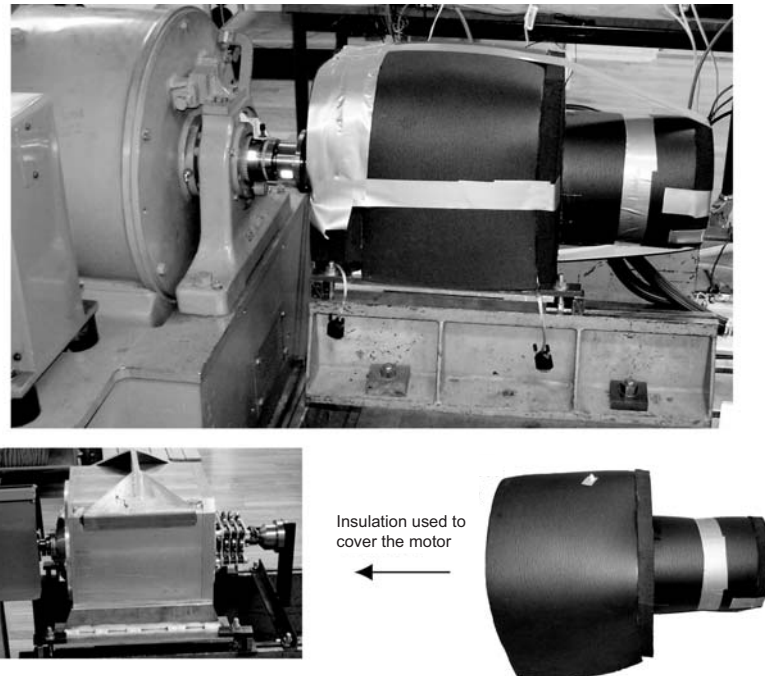


Fig. 6.20 Calculated DRM efficiency map from the licentiate thesis [23].

## 6.7 Calorimetric measurements

Calorimetric measurements are made by thermally isolating the machine from its surroundings and measuring the losses of the machine by measuring the total heat flow transferred by the cooling media. For the 4QT this was done by insulating the whole 4QT machine with closed cell foam so no or minimal thermal exchange existed between the 4QT and the surrounding environment, Figure 6.21. The inlet and outlet temperatures, and the flow of water were measured according to section 6.2.1. The hoses were insulated between the machine in/outlet and the measurements sensors, Figure 6.22.



*Fig. 6.21 Motor insulation for calorimetric measurements.*

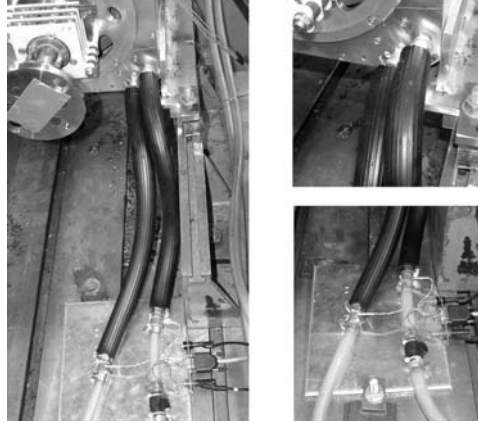


*Fig. 6.22 Insulation of water cooling hoses.*

To seal the machine, the air cooling fan was removed and the air cooling holes in the shields were sealed, Figure 6.23. These combined steps were effective in thermally sealing the machine from its surrounding, which is an essential precondition for accurate calorimetric measurements.

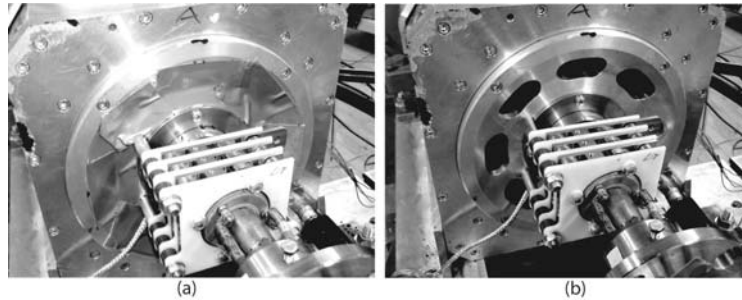


*Fig. 6.23 Air cooling holes in shields, (a) sealed air holes, (b) open air holes.*

The machine is first run as a generator until thermal steady-state conditions are reached. The water flow rate and temperatures are then measured to give the calorimetric losses. By measuring the three phase output power with a power meter both the output power and the power losses can be determined thus the efficiency can be calculated. This was done for the operating points in Table 6.6. As can be seen in the table, the efficiency for the 4QT Stator is around 93.5 and 93.4% at 90 and 95% respectively of the load torque at nominal speed. The inaccuracies of the calorimetric measured efficiencies are determined in section 6.8. Using the values of the input power from the torque meter at the drive motor, which has a reading error of 0.25 Nm, and the speed from the frequency of the current combined with the output power measured with the power meter gives an efficiency of 95%.



Table 6.6 Operating points for calorimetric loss measurements in generator mode.

Speed [rpm]	Torque [Nm]	Phase Voltage [V]	Phase current [A]	Output power [W]	Calorimetric losses [W]	Efficiency [%]
4000	62.75	85.6	104.6	25050	1733	93.5
4000	66.75	84.5	112.6	26600	1872	93.4
4000	No-load	92.9	0	0	995	-

## 6.8 Accuracy of the efficiency results

In the measurements the output power was measured with a power meter<sup>1</sup> and the inaccuracies of this power meter are shown in Table 6.7 according to a data sheet in [37]. The power meter was equipped with a current<sup>2</sup> probe with an inaccuracy of 2% in the 200 A range. The flow sensor<sup>3</sup> had an inaccuracy of 1% [39] of the reading value and the temperature sensors<sup>4</sup> had an inaccuracy according to EN60751 class B, which is 1°C of the measured temperature.

Table 6.7 Inaccuracies of the used power meter [37].

Frequency	Voltage and current	Power
45-66 Hz	0.1% rdg+0.1% rng	0.2% rdg+0.5% rng
66-1000 Hz	0.1% rdg+0.1% rng	0.1% rdg+0.1% rng

rdg = reading, rng = range

Power meter was calibrated in November -04

1. Yokogawa WT1030M
2. Prova DC/AC Current Probe CM-05
3. Swissflow SF-800-B
4. BE03, PT-100

### 6.8.1 Calorimetric efficiency accuracy

For the 4QT Stator running as a generator at an operation point determined by the 2<sup>nd</sup> row in Table 6.6, (4000rpm and 66.75Nm) the following measurement inaccuracy can be determined.

The inaccuracy for the calorimetric losses:

$$P_{\text{losses}} = C_p \Delta t_{\text{error}} \dot{m}_{\text{error}} = C_p \cdot 2 \cdot (0,041 \cdot 0,01) = 3,46 \text{ W} \quad (6.3)$$

Where  $C_p=4186\text{Ws}/(\text{kgK})$ ,  $\Delta t_{\text{error}}=2^\circ\text{C}$  ( $1^\circ\text{C}$  per temperature sensor) and  $\dot{m}_{\text{error}}=1\%$  of the measured value.

The power meter inaccuracy for the same operation point is according to Table 6.7 and using current probes<sup>1</sup> with 2 % inaccuracy:

$$P_{\text{in}} = \frac{0,1}{100} 26600 + \frac{0,1}{100} 200 \cdot 150 + \frac{2}{100} 26600 = 588,6 \text{ W} \quad (6.4)$$

Then the efficiency becomes:

$$\eta = 1 - \frac{1872 \pm 3,46}{26600 \pm 588,6} = \begin{cases} 0,931 \\ 0,928 \\ 0,931 \\ 0,928 \end{cases} \quad (6.5)$$

The mean value and the inaccuracy of the efficiency measurements then becomes  $93.0 \pm 0.2\%$ . This is a very accurate value due to the measuring method used. The inaccuracy in percentage points did not affect the accuracy of the efficiency significantly because of the division of two numbers with large numerical difference.

The accuracy is good for all the calorimetric measurements at high power while for the measurements of no-load losses the calorimetric method is less accurate. When making no-load loss measurements it is best to operate the 4QT as a motor and measure the input power via the power meter and obtain an accuracy according to Table 6.7.

---

1. Prova DC/AC Current Probe CM-05

## 6.9 Prototype parameters

The machine parameters such as inductance and resistance of the 4QT prototype were calculated and measured in [35]. The parameters and results are presented below.

### 6.9.1 Inductance measurements

The d- and q-inductances of the 4QT were measured and calculated in [35]. The measured inductances are presented in Figure 6.24. Before the inductances were measured the rotor was first aligned in the d or q direction by applying a DC current to the winding via phase A, which connected in series with phases B and C, which are connected in parallel. Then an AC current was supplied at different frequencies to phase A via phases B and C, giving the following currents in the different phases:

$$\begin{cases} i_A = \hat{i} \cos(\omega t) \\ i_B = i_C = -\frac{1}{2} \hat{i} \cos(\omega t) \end{cases} \quad (6.6)$$

Measuring the frequency  $\omega$ , current  $I_A$  (RMS), voltage  $U_A$  (RMS) and the phase angle  $\theta$  between the current and voltage, and using equation (6.7) for the q- or d-direction, gives the inductances for the windings:

$$L_{d/q} = \frac{U_A \sin \theta}{i_A \omega} \quad (6.7)$$

Using equation (6.7) the inductances of the two 4QT windings were calculated as a function of the frequency as shown in Figure 6.24 together with the calculated values from section 5.4. The calculated and measured values show good agreement. The second and third points for the inductance measurements show deviant values and should be disregarded. This deviations are due to mechanical vibrations (resonance phenomenon) that occurred during the measurements.

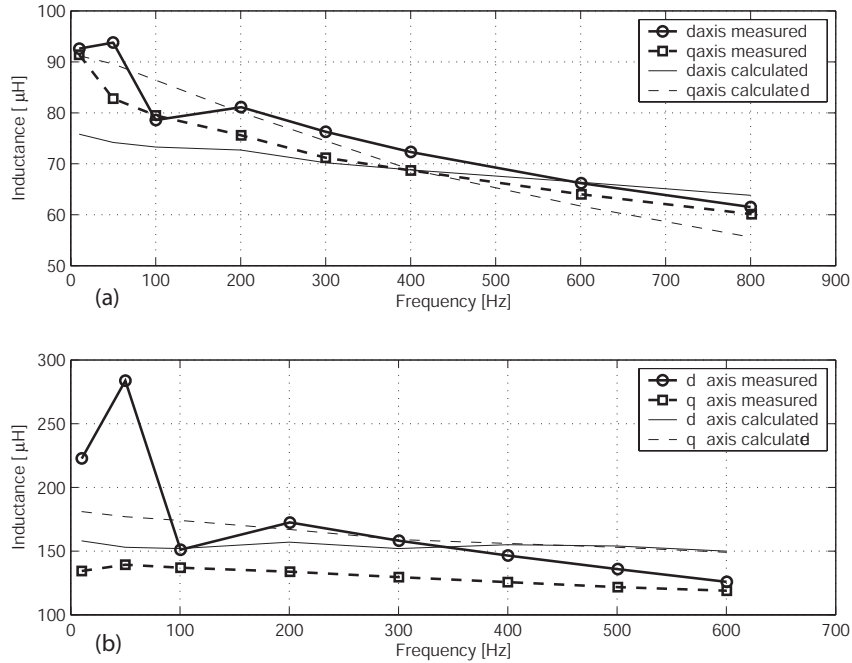


Fig. 6.24 Measured and calculated d- and q-inductances of a) the Stator b) the DRM.

## 6.9.2 Resistance measurements

The resistance of the 4QT machine was calculated and measured in [35],[40], and the values are presented in Table 6.8. These values shows good agreement between the measured and calculated values. For the Inner rotor one phase shows a minor deviant value.

Table 6.8 Measured and calculated resistances for the 4QT prototype.

	Measured resistances [ $\text{m}\Omega$ ]			Calculated resistances [ $\text{m}\Omega$ ]
	Phase A	Phase B	Phase C	
Stator	10.9	11.0	10.6	10.9
Inner rotor	14.2	15.0	13.5	14.9

## 6.10 Test of the new rotor winding

When the two rotors were rotated at different speeds after the inner rotor was redesigned a braking torque at no-load was observed. The braking torques at different speeds and operation conditions are shown in Table 6.9.

Table 6.9 Braking torque at no-load tests of the 4QT.

Speed [rpm]	Torque [Nm]	Power [W]	Operation specifications
400	11	461	Locked inner rotor
600	15	942	Locked inner rotor
800	16	1340	Locked inner rotor
400	10.5	440	Locked outer rotor
800	15	1257	Locked outer rotor
700	3	220	Synchronous rotating rotors

During the tests the bearing and end winding temperatures were measured. The temperature sensors on the inner bearings at each side of the outer rotor were placed as close as possible to the bearings, the sensor placement are shown in Figure 6.25. Figure 6.26 and Figure 6.27 show the temperatures of the bearings and the end windings during the tests specified in Table 6.9.

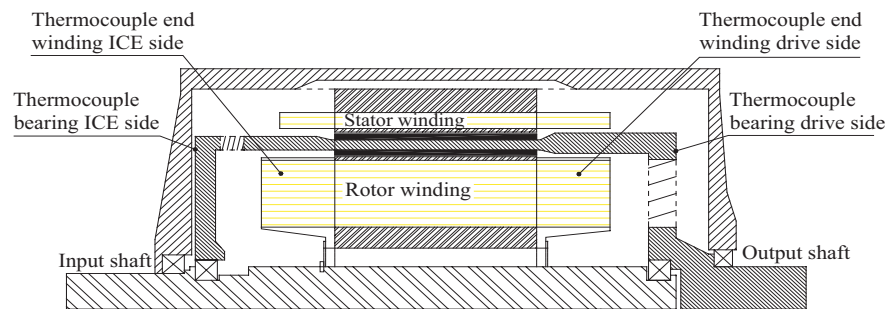


Fig. 6.25 Thermocouple placement for bearing and end winding temperature measurements.

The bearing temperatures shown in Figure 6.26 are measured when the outer rotor is locked and the inner rotor is rotated at 400 and 800rpm. As seen there is a

rapid and almost linear increase of the temperature,  $66^{\circ}\text{C/h}$  at 800rpm and  $24^{\circ}\text{C/h}$  at 400rpm. The temperature thus increase 2.8 times faster when the speed is doubled. Figure 6.27 shows the end winding temperature when the inner rotor is locked, which made it possible to access the temperature sensors in the inner rotor. During this test the initial temperature rises are  $204^{\circ}\text{C/h}$  at 800rpm and  $52^{\circ}\text{C/h}$  at 400 rpm. The temperature rise is almost 4 times faster when the speed is doubled. Since the temperature rise is much faster for the winding than the bearings it is probable that the losses are located in the inner rotor windings. The losses could be due to circulating currents in the windings or short circuits between the phases in the windings. Insulation tests made earlier on the windings did not indicate any earth fault between the inner rotor winding to the laminations or the shaft. Since the measured phase resistance of the three phases are equal as shown in Table 6.10 the possibility of a short circuit between the phases in the inner rotor is small.

Analysis of the measured temperatures at the inner rotor showed that the temperature increase was almost 4 times faster for 800rpm than for 400rpm. Doubling the speed will also double the induced voltage. If we assume a constant resistance in the circuit the current will also be double. Since the power loss is the product of the voltage and the current the power loss will increase by a factor of 4 when the speed is doubled. This implies that the heating power in the inner rotor is generated through the induced voltage. It is therefore very likely that the fault originates from circulating currents or short circuit in the windings. The circulating currents are further investigated by FE simulations in section 8.6.

Table 6.10 Phase to phase resistances of the inner rotor [40].

Phases	Applied DC current [A]	Measured voltage [V]	Resistance [ $\Omega$ ]
L1-L3	10	0.283	0.028
L1-L2	10	0.298	0.030
L3-L2	10	0.292	0.029

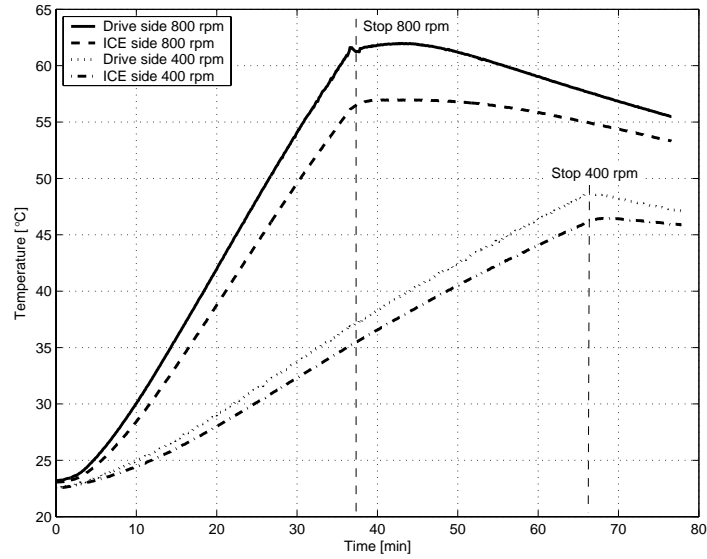


Fig. 6.26 Bearing temperatures at 400 and 800 rpm between the rotors. The outer rotor was locked during the test.

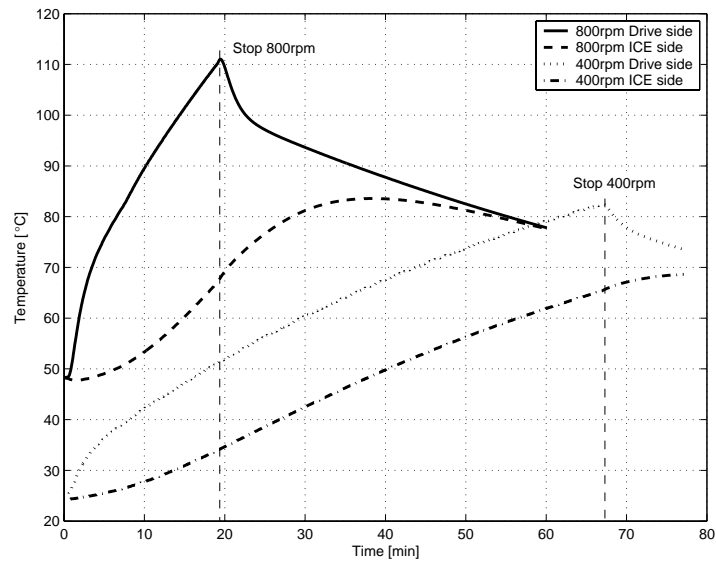
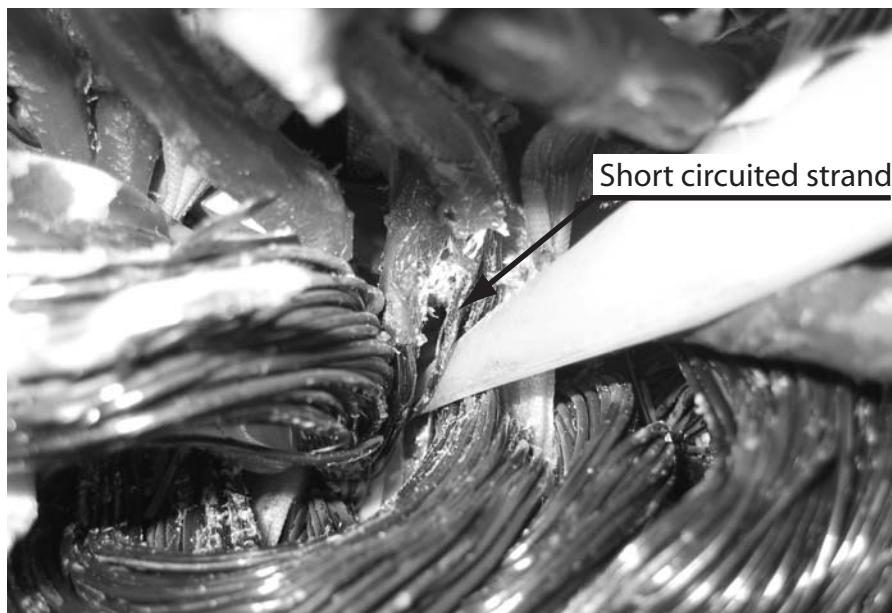


Fig. 6.27 End winding temperatures at 400 and 800 rpm between the rotors. The inner rotor was locked during the test.

After dismantle of the 4QT prototype it was discovered that short circuit between the phases had occurred in the inner rotor winding. One strand of one phase from one of the turns of one phase was connected to another phase, as shown in Figure 6.28. Due to this manufacturing fault a one-strand short circuit between two phases occurred which introduced power losses that burned the insulation and heated up the inner rotor.

Another fault that had occurred was that the end windings at the ICE side of the inner rotor winding were bent outwards due to centrifugal forces and touched the outer rotor. This happened because of the bad or non existing bandaging of the inner rotor end windings. A picture of the bent end windings are shown in Figure 6.29.

A simulation of the short circuit current through the strand can be performed according to the method described in section 8.5 for circulating currents, by short circulating coil number 75 in Figure 8.9 down to the point in the circuit between coil 116 and 121. The simulated short circuit current is shown in Figure 6.30 and has a RMS value of 182 A. This large FEM simulated short circuit current at no-load implies that a one-strand short circuit between two phases will give a significant short circuit current even when the machine is operating at no-load conditions.



*Fig. 6.28 One strand short circuit between two phases in the inner rotor winding.*



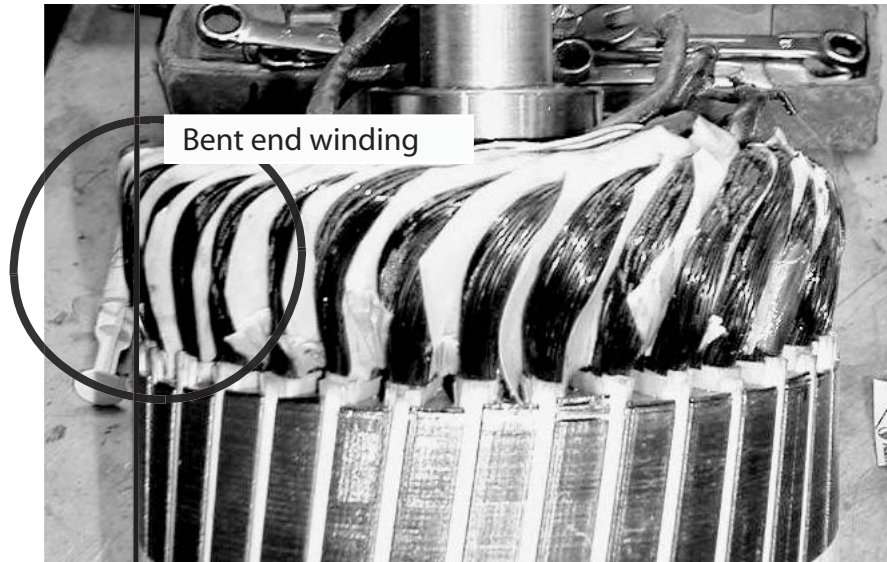


Fig. 6.29 End winding bent outwards due to centrifugal forces and lack of sufficient bandaging.

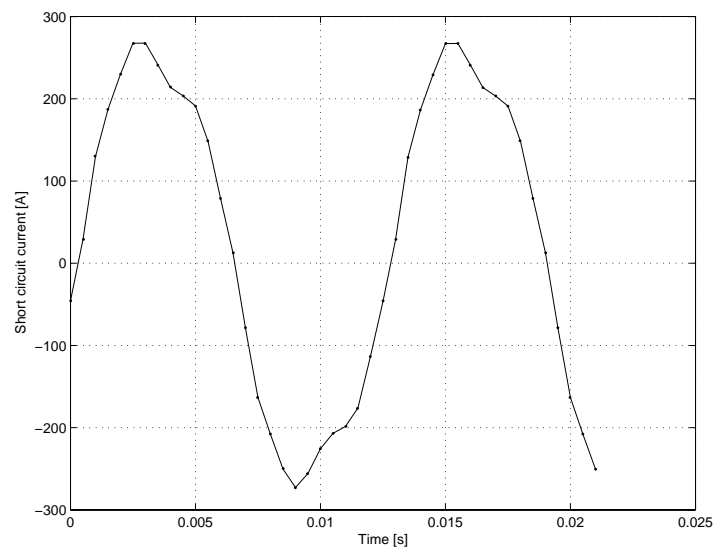


Fig. 6.30 FEM simulated short circuit current in one strand phase to phase short circuit.

## **6.11 Conclusions**

The 4QT prototype has been tested both at no-load and at load conditions. The machine gives the rated torque at rated speed and current. Induced voltage for the machines are according to calculations.

The thermal performance of the machine were both better and worse than expected. The Stator thermal performances are good and the water cooling is effective. The inner rotor cooling was at the beginning not sufficient so the rotor windings failed due to high temperature. After a redesign of the windings a unwanted braking torque between the rotors was discovered and thus no testing at load or at speeds over 800rpm was possible. When a second rewinding of the inner rotor was done it was possible to test it, then the DRM showed efficiency close to the predicted but the temperature of the winding was too high at load conditions. Better cooling of the inner rotor is required to achieve the desired performance.

The efficiencies of the Stator and DRM are close to the analytically calculated efficiencies from [23].

## 7 Thermal modelling

Thermal modelling is used to predict the thermal design of the machine and to investigate possible design improvements. The modelling of the 4QT prototype has been performed by lumped circuit modelling in order to achieve high calculation speed and flexibility for small design changes in the thermal system. This model is then verified by FE modelling and by measured values from generator tests of the prototype.

The FE modelling has been made for a 2D geometry of the 4QT prototype, with no consideration taken to the axial heat flow out of the machine and no modelling of the end windings of the Stator and the inner rotor. In the lumped circuit model, the end winding, the heat flows in the axial direction through the shaft, and the convection in the end regions of the machine are included as simple models.

### 7.1 Lumped circuit modelling, steady-state

To make a lumped circuit model of the 4QT, a quarter of the axial cross section was chosen. When performing electromechanical FE modelling of the 4QT only one pole was chosen, but in the thermal analysis a quarter of the machine is needed to achieve thermal symmetry. The quarter of the 4QT cross section is further divided into layers and sections as shown in the example of a 90 degree circle sector in Figure 7.1. In this figure the circle sector is divided into four layers and three sections which gives twelve network pieces with a network node in the centre of each piece. The lumped circuit is then modelled between the nodes, in this case with twelve nodes, the thermal network consists of seventeen thermal resistances. To calculate the thermal resistances between the nodes equation (7.1) are used.

$$R_{th} = \frac{l}{A \cdot \lambda_c} \quad (7.1)$$

Where  $l$  is the distance between the nodes,  $A$  is the area between the nodes taking into account the axial length of the machine and  $\lambda_c$  is the thermal conductivity. The thermal network is solved iteratively by using equation (7.2) [22] for each node until the desired accuracy is reached. It is also possible to make a transient thermal analysis if adding the thermal capacitance in each node [50].

$$t_i = \frac{q_i + \sum_j \frac{t_j}{R_{ij}}}{\sum_j \frac{1}{R_{ij}}} \quad (7.2)$$

In equation (7.2) the thermal source  $q_i$  is the losses in the specific node  $i$ ,  $t_j$  is the temperature in node  $j$  where  $j$  is the number of one of the adjacent nodes and  $R_{ij}$  is the thermal resistance between nodes  $i$  and  $j$  where  $i$  is the node of which the temperature is to be calculated. Solving equation (7.2) for all nodes gives the temperatures at steady-state for all the nodes in the thermal lumped circuit.

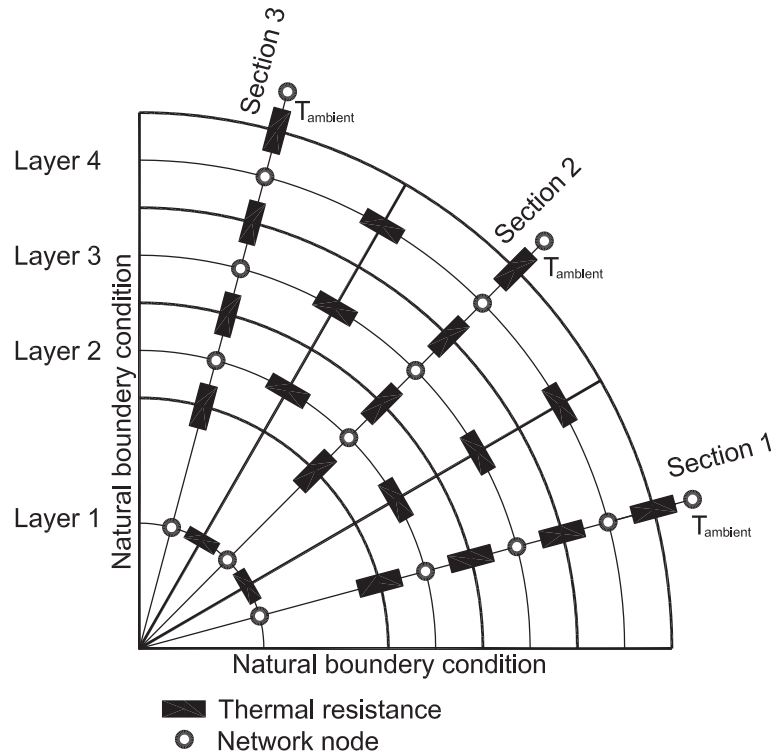


Fig. 7.1 Example of a thermal lumped circuit network of a circle sector of 90degrees.

The thermal network used for the 4QT machine is a bit more complicated than the example shown above. This is because the complex 4QT geometry which consists of slots, air and water cooling channels etc., makes it necessary to use

between 2 and up to 72 sections for each layer. The 4QT is made up of 14 different layers according to Table 7.1. The 4QT network model is shown in Figure 7.2. The model network in Figure 7.2 consists of 331 different network pieces and the model will thus contain 331 nodes. One extra node is also added for the external air so the total sum of nodes becomes 332. The model contains even more thermal resistances but many of them have the same value so there are only about 50 different thermal resistance values in the model. The thermal network for the part of the 4QT which is an axial symmetry is shown in Figure 7.3.

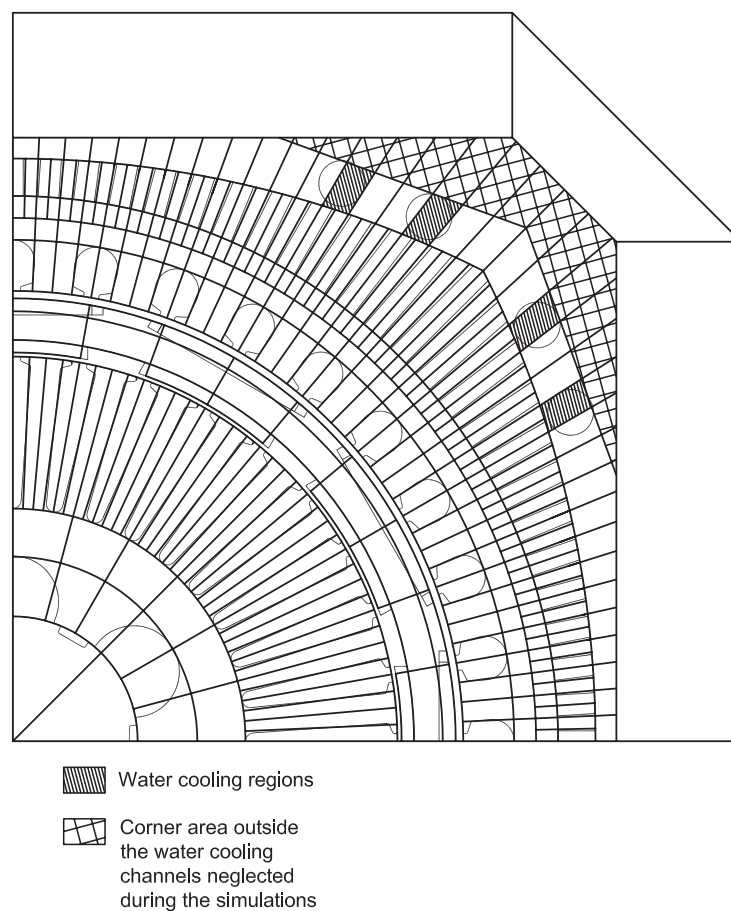
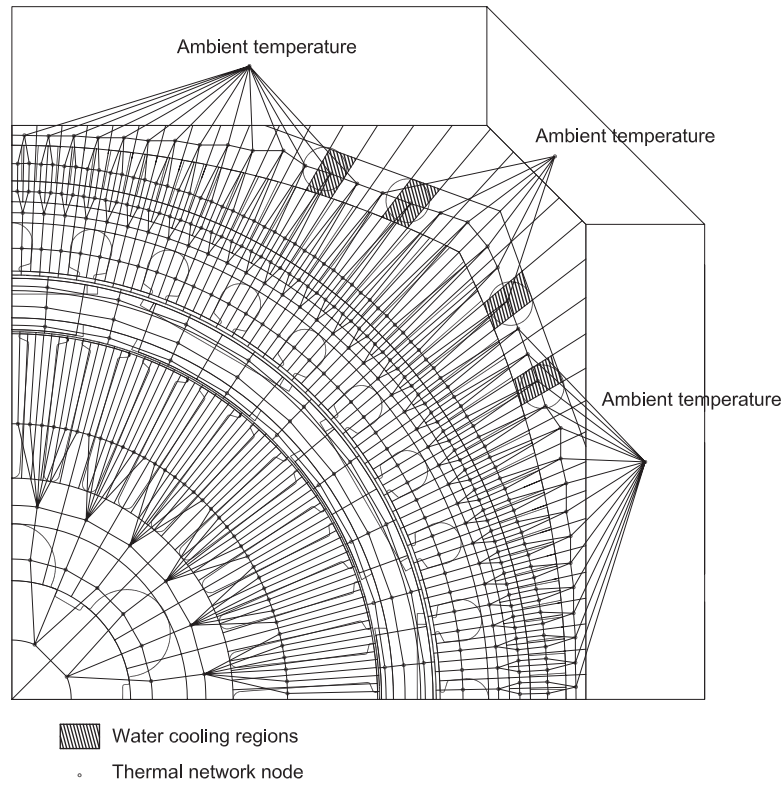


Fig. 7.2 4QT machine geometry divided into rectangular network for thermal modelling.

*Table 7.1 Layer description for the 4QT thermal model.*

Layer	Description	Number of nodes
1	Shaft	2
2	Rotor lamination with axial air cooling channels	6
3	Rotor Laminations	6
4	Rotor slots and laminations	36
5	Inner air gap	1
6	Inner magnets with intermediate air	9
7	Outer rotor steel tube	9
8	Outer magnets with intermediate steel	9
9	Outer air gap	1
10	Stator slot and laminations	36
11	Stator back laminations	36
12	Second stator back lamination	72
13	Housing with air cooling channels	72
14	Housing aluminium with water cooling channels	36
Outer air	Constant outer air temperature layer	1 (divided into 3 for the circuit figure)



*Fig. 7.3 Thermal network with lumped circuit for the 4QT machine.*

To model the slots of the 4QT machine a method, which is a modification of the method used in [32], is introduced. The slot models are shown in Figure 7.4 for the Stator and the inner rotor. The insulation thermal coefficient was chosen according to [32] to  $0.0735 \text{ W/m}^2\text{C}$ . Then the different copper layers in the slot model are connected by thermal resistances and inserted in the model for the complete machine. The copper loss in each slot is distributed within the different copper layers in proportion to the area of each layer.

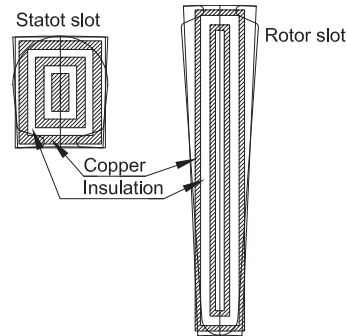


*Fig. 7.4 Slot models for the 4QT thermal lumped circuit model.*

The axial modelling was carried out by assuming symmetry at the axial centre and modelling only half the length of the 4QT and assuming no thermal exchange between the halves. The end windings need then only to be modelled on one side of the machine and they were only modelled with one node for each slot. The end winding thermal resistance was calculated by using the model in Figure 7.5 where the length and cross section area are presented.

The convection resistance to the surrounding air was modelled with the total outer area of the model in Figure 7.5 and a chosen convection heat transfer coefficient according to [32] and [33].

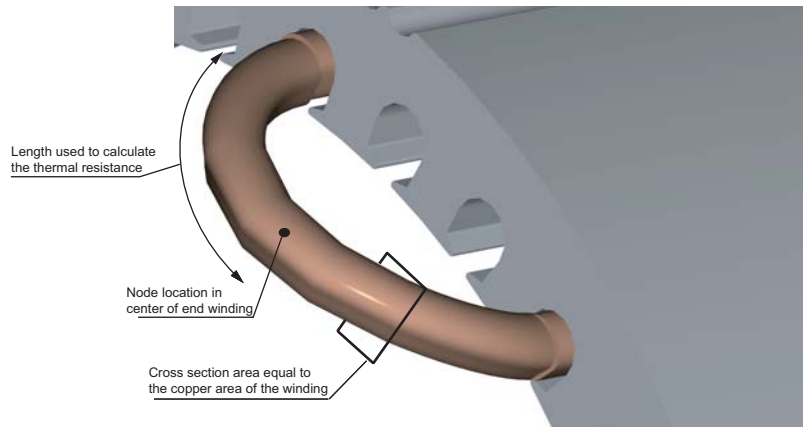


*Fig. 7.5 End winding model used for thermal resistance calculations.*



## 7.2 Results from the lumped circuit modelling

The results at full load in both the Stator and the DRM are shown in Figure 7.6. The losses in the model are taken from analytical calculations while the air temperature is taken from measurements made in the comparing test. The cooling water temperature is changing throughout the water cooling channels. To use the Newton's law of cooling in the model a mean temperature value has to be used. The generally accepted method is to use the logarithmic mean temperature difference (LMTD) defined in equation (7.3). Using the values of the inlet and outlet cooling water temperature from measurements during the load test, this value becomes 12.8°C.

$$t_{\text{LMTD}} = \frac{t_{\text{in}} - t_{\text{out}}}{\ln(t_{\text{in}}/t_{\text{out}})} \quad (7.3)$$

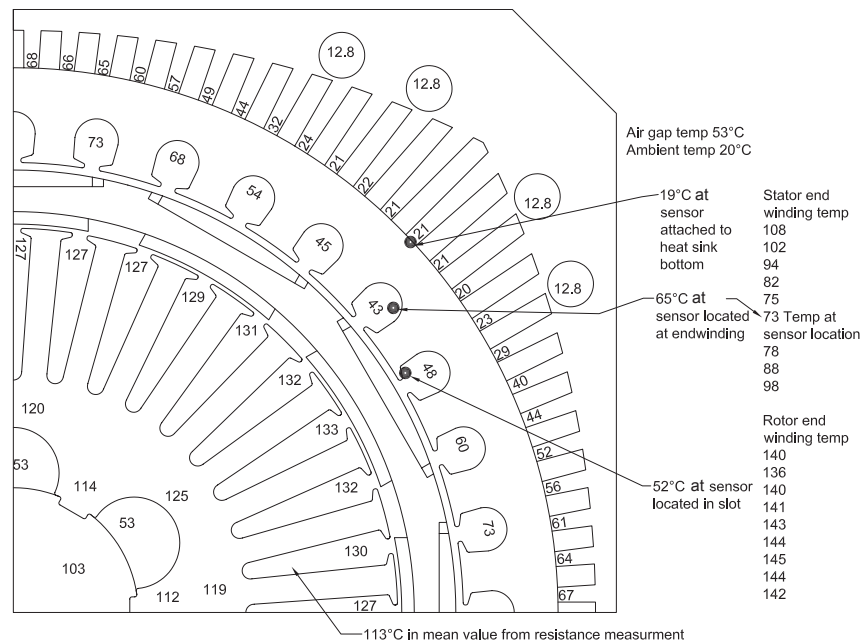


Fig. 7.6 Measured and simulated values of the temperature distribution at full load in the 4QT machine.

*Table 7.2 Simulated and measured values of the temperature in the 4QT.*

	Simulated [°C]	Measured [°C]	Difference [%]
Stator slot	48	52	-8
Stator end winding	65	73	-12
Heat Sink	21	19	+10
Inner rotor winding	129	113	+14

As can be seen in Figure 7.6 the simulated and the measured values at the full load test show good agreement. Table 7.2 presents a comparison between the simulated and the measured values at some selected positions in the 4QT machine and it can be seen from the table that the difference is between 8 to 14 % which can be considered to be good enough for evaluating the impact of the design changes on the cooling system.

One warning which can be interpreted from the simulations is the inner rotor end winding temperature. The maximum simulated value is 145 °C and with an error equal to the maximum error for the simulations which is 14 %, this becomes 165 °C. This lies at the limit of the maximum winding temperature, allowing for unaccounted hot spots the maximum temperature can be much higher which can lead to an insulation breakdown of the machine. Sadly this was also the case and as a very unfortunate timing, the present simulations were performed after the machine breakdown.

To decrease the inner rotor end winding temperature, different cooling methods can be used, a number of them are shown later in this chapter, including the method of forced air cooling using an external fan which was also implemented in the new design of the 4QT prototype.

### **7.3 Different cooling options**

As can be seen from tests and simulations the most challenging part of the 4QT is to cool the inner rotor and specially the inner rotor winding. To improve the cooling of the 4QT four different ways were investigated:

- Modified water cooling channels
- Fluid cooling in the shaft
- Air cooling in the rotor slot
- Forced air cooling of the inner rotor

The first method has an impact mostly on the cooling of the Stator while the second and the third have an impact mostly on the inner rotor and the fourth has an impact the whole machine.

### 7.3.1 New water cooling channels

The water cooling of the Stator has been improved in quite a conventional way. The improvement consists of the removal of the air cooling ducts between the Stator and the housing and to modify the shape and the distribution of the water cooling ducts. This gives a shorter distance and a larger area for the heat flow from the Stator to the cooling water as shown in Figure 7.7. This change in cooling of the 4QT mostly has an impact on the cooling of the Stator.

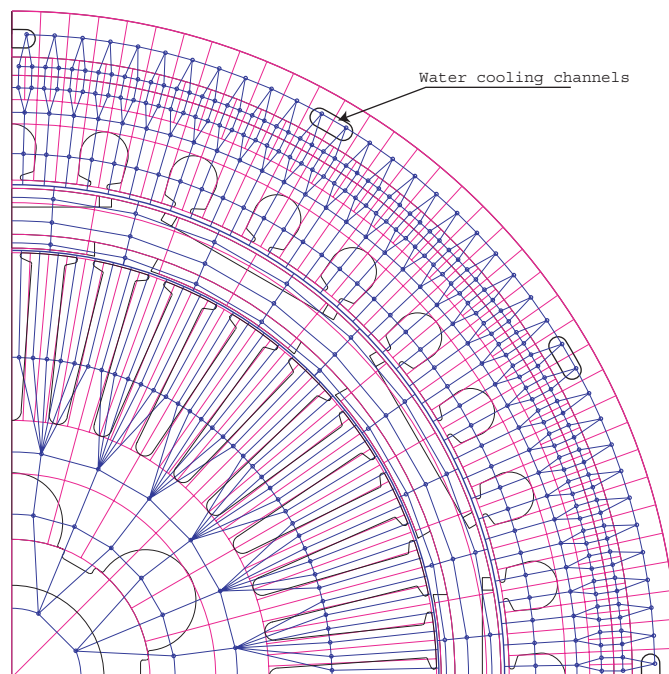


Fig. 7.7 New design with a more efficient water cooling of the Stator.

This design change give a better cooling of the Stator and reduced the temperature from 73 to 50 °C for the end winding, and from 48 to 36 °C for the stator slot temperature at full load, according to the lumped circuit model. This is because removal of the heat sink, that was primary introduced to cool the internal air flow, decreased the thermal resistance between the Stator core and the cooling water.

### 7.3.2 Fluid cooling in the shaft

The second idea was to increase the cooling of the 4QT by introducing fluid cooling in the inner shaft. If oil is used as the fluid it should be possible to lead the inlet oil through an oil pipe in the centre of the inner rotor shaft as shown in Figure 7.8. The drawback with this method is that it requires an eccentric placement of the propulsion shaft between the ICE and the 4QT in order to allow insertion of a pipe in the axial direction for the cooling fluid. It may also be possible to use a fluid “slipping” for the transfer of the cooling medium to the rotating inner rotor.

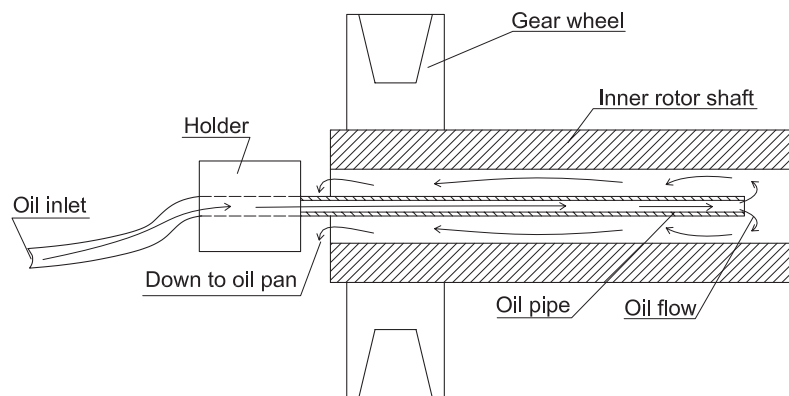


Fig. 7.8 Proposal for oil cooling system in the inner rotor shaft.

This was simulated by adding one extra layer before the first layer in Table 7.1 which is the shaft layer. The nodes of the shaft were thus connected to the node in the new oil cooling layer. Then the axial air cooling channels in the inner rotor were replaced by lamination material as the air holes do not contribute too much to the total cooling when liquid cooling is used in the shaft. The oil cooling layer consists of one node with a constant temperature of 60°C.

This gives a decrease of temperature from 145°C to 102°C in the inner rotor end windings and from 156°C down to 106°C in the inner rotor slots, according to the lumped circuit model. This is a decrease of about 30% in the rotor temperature. Using a cold fluid would decrease the temperature even further.

### 7.3.3 Air cooling of the rotor slot

The third alternative was to introduce an air cooling channel in the rotor slot, see Figure 7.9. This should reduce the winding temperature if the air is made to flow close to the winding. The large draw back is of course the reduced fill factor in the slots but this draw back should be evaluated in relation to the gain in expected improved cooling.

When evaluating this method a node was added in the rotor slots with a constant temperature and the thermal resistance was calculated from the data of air velocity, assuming a long channel, and the area of the cooling duct.

The results are shown in Figure 7.10 for different forced air cooling speeds. The temperature doesn't decrease until the air speed reaches 5 m/s, this is because below 5 m/s the air flow in the cooling channel is laminar and the temperature field is fully developed. In this case the Nusselt number is constant with constant wall temperature or constant heat flux and this gives a constant convection heat transfer coefficient [33] until the air flow becomes turbulent for air speeds above 5 m/s.

The temperature decrease by introducing the air cooling ducts in the slot are from 156°C down to 145°C for an air speed of 5 m/s and down to 126°C for an air speed of 9 m/s. This gives a decrease of 20% for the higher air speed which is lower than for the fluid cooling of the shaft. But still there is a decrease in the inner rotor winding temperature.

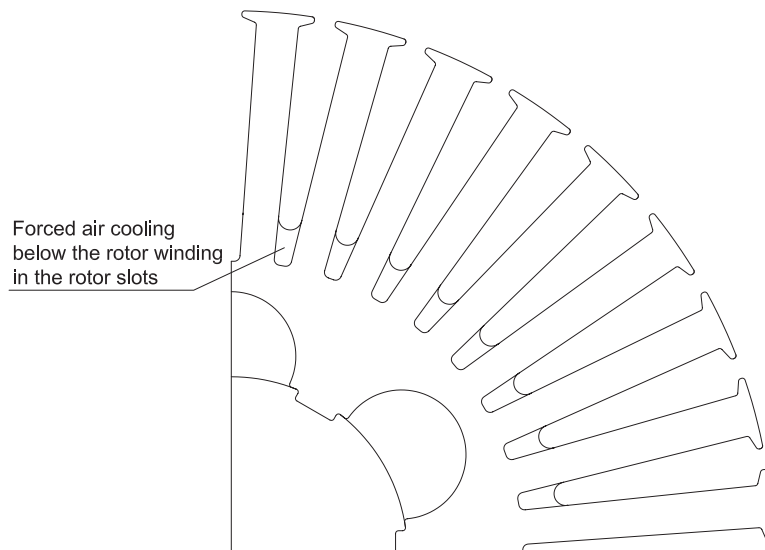


Fig. 7.9 Air cooling of the rotor slots.

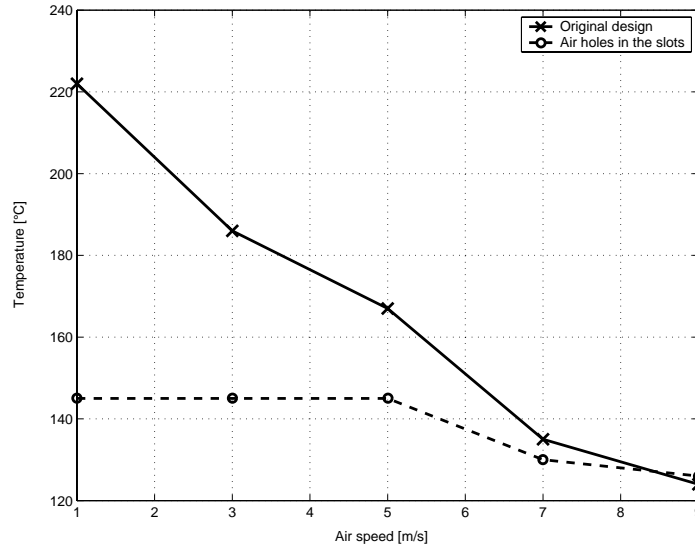


Fig. 7.10 Slot temperature at different forced air cooling speeds.

### 7.3.4 Forced air cooling of the inner rotor

Forced air cooling of the 4QT by an external fan is simulated in steps with different convection heat transfer coefficients in the axial air holes. Figure 7.12 shows the heat transfer coefficient in the axial air holes and the inner air gap as a function of the cooling air speed used in the simulation. The heat transfer coefficients were calculated analytically according to [22] [33]. The constant value of heat transfer coefficient between 1-2 m/s in the air holes and 1-5 m/s in the air gap is when the air flow is laminar and thus the Nusselt number is constant and this gives a constant heat transfer coefficient [33]. No consideration has been taken to the influence of rotation of the rotors on the heat transfer coefficients.

According to [33] the heat transfer coefficient for turbulent flow in tubes for air with an air speed between 1-10 m/s is between 10-50 W/(m<sup>2</sup>°C) and this is fulfilled in the heat transfer coefficient calculation.

As can be seen in Figure 7.11 the inner rotor winding temperature decreases from 184 down to 103 °C when the air speed is increased from 1-10 m/s. In this case the air temperature was assumed to be 30 °C. With this knowledge a suitable size of the forced air cooling fan can be chosen.

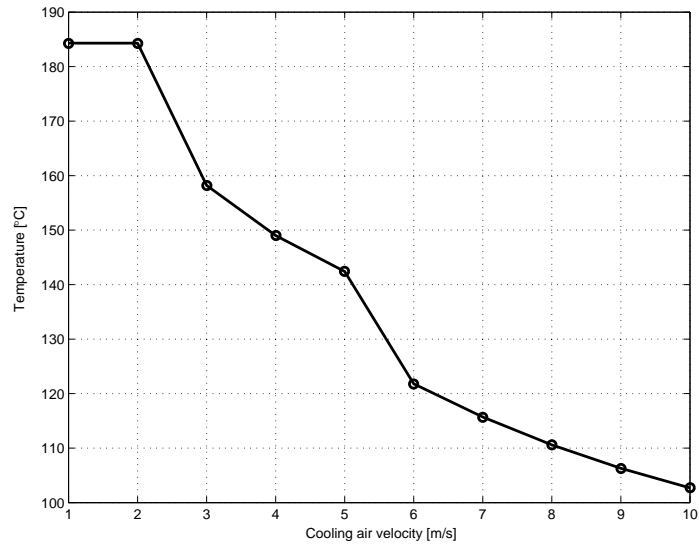


Fig. 7.11 Inner rotor winding temperature at different cooling air speeds.

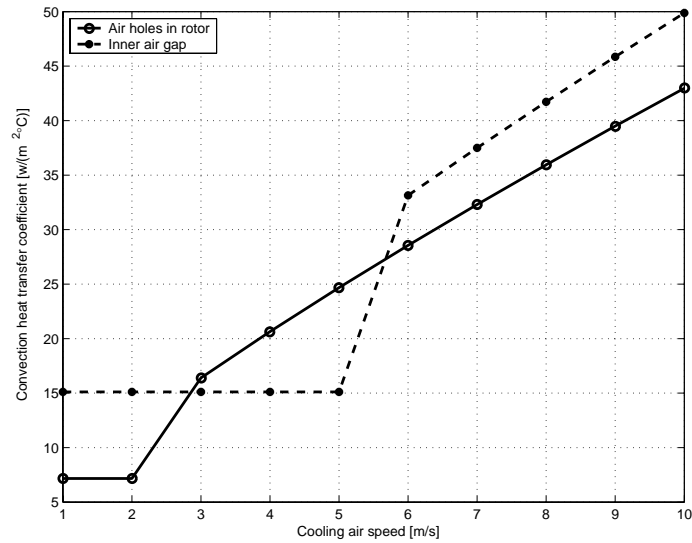


Fig. 7.12 Heat transfer coefficients in the axial air cooling holes in the inner rotor and in the inner air gap versus the cooling air speed.

## 7.4 Thermal FE modelling

Thermal FE modelling was carried out for a quarter of the 4QT machine in FEM-LAB<sup>1</sup>. The simulations was done for the geometry shown in Figure 7.13, with the same losses, heat transfer coefficients and materials as used in the thermal lumped circuit model in sections 7.1 to 7.3. Figure 7.14 shows the results from a steady-state FE simulation of the temperature distribution when loading both the Stator and the DRM with nominal load.

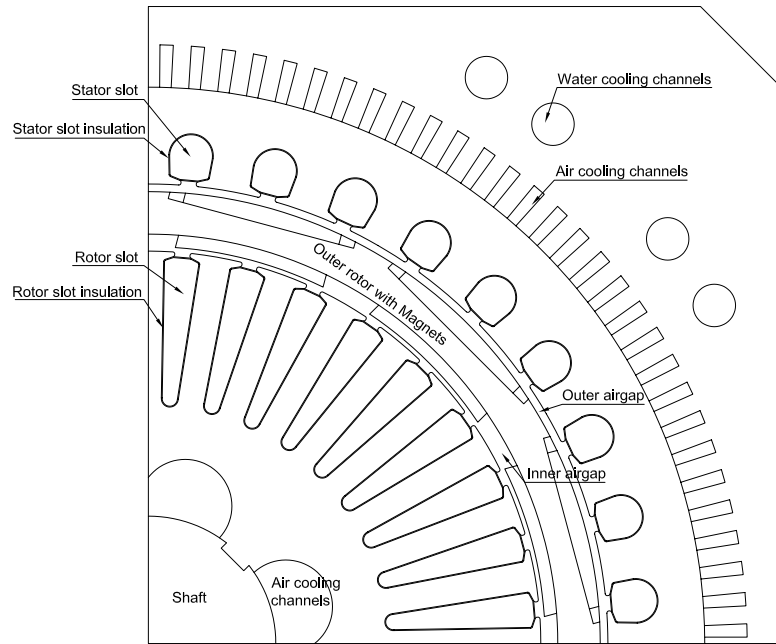


Fig. 7.13 The FE geometry used in the thermal modelling.

In the lumped circuit simulations the heat flow in axial direction through the shaft of the machine was included in the model. To include this axial heat flow in the FE model, equation (7.4) was first used to calculate the heat flow in watts through the shaft. The heat flow was thereafter added as a negative heat source on the shaft surface.

$$\Delta T = q \cdot R_{th} \quad (7.4)$$

In equation (7.4)  $\Delta T$  is the temperature difference between the centre and the end

---

1. FEM program from Comsol



of the shaft,  $q$  is the heat flow in the shaft, and  $R_{th}$  is the thermal resistance from the centre to the end of the shaft used in the lumped circuit model. Using the same approach, the heat flow in the air cooling channels of the housing were calculated.

The internal air in the simulation was set to 53 °C as in the lumped circuit modelling. In the lumped circuit modelling the air temperature was set as a fix temperature, but in the FE modelling the air temperature was set as an external boundary condition in equation (7.5) for boundaries that are facing an air surface.

$$\vec{n} \cdot (k \nabla T) = q + h(T_{inf} - T) + C_{const}(T_{amb}^4 - T^4) \quad (7.5)$$

Where  $q$  is the boundary heat flux source, which is not used in this simulation,  $C_{const}$  is the constant for the radiation heat flux, which is also not used in the simulation,  $h$  is the convection coefficient,  $T_{inf}$  and  $T_{amb}$  are the external temperatures.

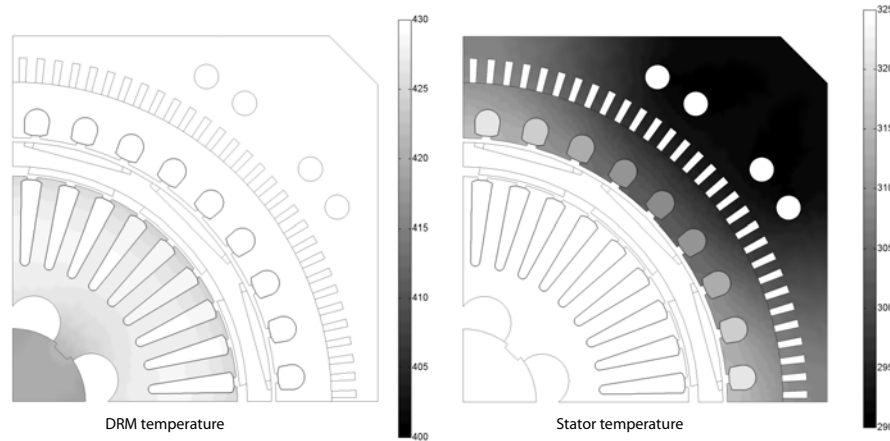


Fig. 7.14 FE simulated steady-state results of the temperature distribution in the 4QT machines, both operating at nominal load. Temperatures are given in degrees Kelvin (i.e. degrees Centigrade +273).

Figure 7.14 shows the results from the FE steady-state simulation at nominal load in both machines. The figure is separated into Stator and inner rotor temperature distribution for higher resolution. Table 7.3 shows the temperatures for the Stator and inner rotor in the 4QT machine for the FE and lumped circuit simulations. As can be seen from the table, the FE model simulates a lower value for the Stator slot temperature and a higher value for the inner rotor slot temperature. This could be because the axial cooling of the end windings has a larger impact

on the total cooling of the inner rotor windings than of the Stator windings, where the water cooling is the dominating cooling system. Table 7.3 also shows the temperatures when the heat transfer coefficients in regions with cooling air are doubled simulating forced air cooling. It is clearly seen that the DRM temperature is strongly correlated to the air cooling while the Stator temperature is almost only dependent on the water cooling.

The simulated values are dependent of the coefficients in the models and this will give some differences between the values calculated from the FE and lumped circuit model. The lumped circuit model takes the axial heat flux into consideration which the 2D FE model is not capable of doing. To make a fair comparison a 3D FE model should be used. The lumped circuit model also calculates with the contact resistance and interface gaps between the solid materials [32]. This cannot be easily implemented in the FE model.

Table 7.3 Comparison of FE and lumped circuit temperatures.

	FEM [°C]	FEM [°C] <sup>a</sup>	Lumped circuit [°C]
Stator slot	36-48	36-48	43-73
Rotor slot	156	107	127-133

a. Doubling of the heat transfer coefficient, simulating forced air cooling.

## 7.5 Conclusion

A thermal lumped circuit model has been developed for the 4QT prototype. The model has been verified by measurements and by comparison with FE modelling. The results show good agreement between simulated and measured values.

According to the model the most critical part of the construction is the inner rotor where the windings are the most sensitive part. The thermal limitations of the inner winding are nearly reached in the simulations and there is therefore a risk that some spot could reach too high temperature. This was observed in the first 4QT prototype, which failed due to an over heated inner winding.

The lumped circuit has then been used to investigate possible design improvements for the 4QT cooling system. To improve the cooling for the existing prototype the only real possibility is to use an external fan with forced air cooling. An external fan for forced air cooling has been introduced when modifying the prototype after the first breakdown.

## 8 Losses in the 4QT

The losses in the 4QT can be separated into:

- Resistive losses
- Iron losses
- Mechanical losses
- Stray losses

The resistive or copper losses are the losses due to the resistance in the windings, the iron losses are the losses due to the eddy currents and the hysteresis losses in the iron cores, the mechanical losses are losses due to friction and windage, and the stray losses are the remaining losses in the machine. Figure 8.1 shows the power flow and the different losses for the 4QT machine operating as motor and generator.

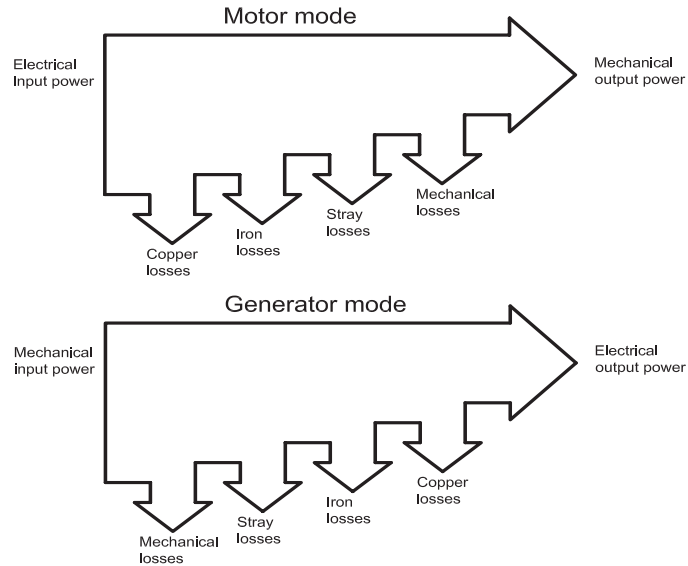


Fig. 8.1 Power flow in any one of the 4QT machines operating either in motor or generator mode.

### 8.1 Resistive losses

The resistive or copper losses can be calculated as:

$$P_{cu} = 3 \cdot R_{ph} \cdot I_{ph}^2 \quad (8.1)$$

For the 4QT the measured DC resistances are  $10.9\text{m}\Omega$  for the Stator and  $14.2\text{m}\Omega$  for the inner rotor windings at room temperature; this gives a current load dependent copper losses as shown in Figure 8.2 with  $400\text{W}$  for the Stator winding and  $795\text{W}$  for the rotor winding at nominal load and room temperature.

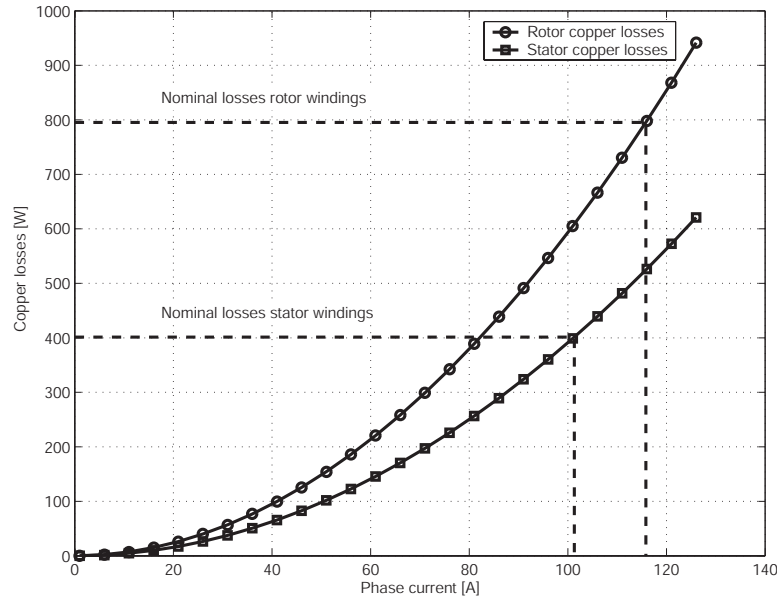


Fig. 8.2 Analytically calculated copper losses for the 4QT.

## 8.2 Iron losses

The iron losses have been calculated both analytically and with FEM. These values have then been compared with the measured values from the motor tests.

### 8.2.1 Iron losses from an analytical model

There are a number of different ways to analytically calculate the iron losses in permanent magnet machines. The basic principle is to first calculate the flux density in the core parts such as the core back and/or teeth and then together with the power loss density information at the required frequency obtained from the data sheets from the iron sheet manufacturer, calculate the iron losses for the specific amount of active iron used in the machine.

[15] gives equation (8.2) and equation (8.3) for the iron losses in the stator teeth

and in the stator back (ring):

$$P_{fet} = KBT \cdot (0,06 \cdot W_{ts} \cdot f \cdot (100 + f) \cdot B_{ts}^2 \cdot 10^{-3}) \cdot G_{ts} \quad (8.2)$$

$$P_{fer} = KBR \cdot (0,06 \cdot W_{rs} \cdot f \cdot (100 + f) \cdot B_{rs}^2 \cdot 10^{-3}) \cdot G_{rs} \quad (8.3)$$

Where  $f$  is the electrical frequency,  $KBT$  and  $KBR$  are correction factors for the teeth and the back,  $G_{ts}$  and  $G_{rs}$  are the weights of the teeth and back and  $W_{ts}$  and  $W_{rs}$  are the loss factors for the teeth and the back at a flux density of 1.5 T. Figure 8.3 shows the iron losses for the stator and DRM back, teeth and the total losses. The total losses at nominal frequencies 400 and 300 Hz are 739 W and 490 W for the Stator and DRM respectively.

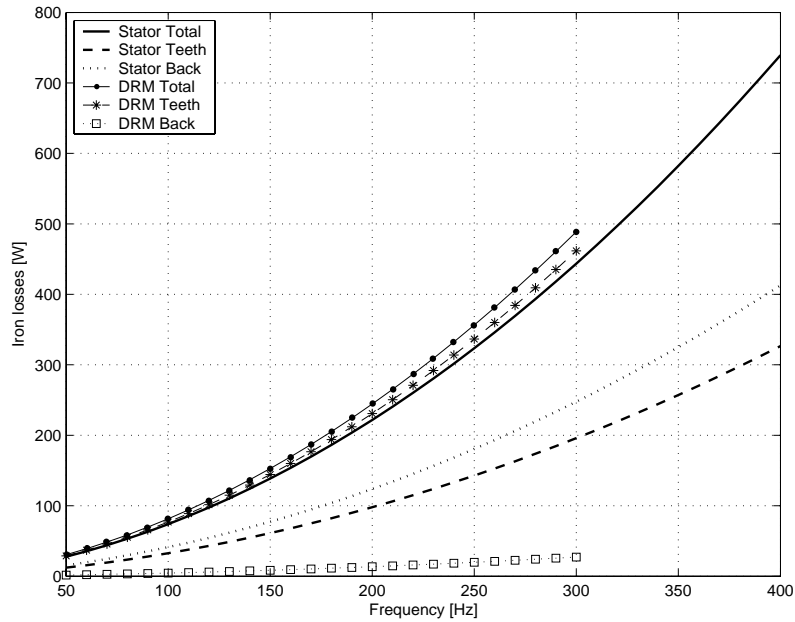


Fig. 8.3 Iron losses in the Stator and the DRM calculated using an analytical model.

## 8.2.2 Iron losses using FEM

The iron losses can be calculated for the magnetic core region by the program FLUX2D if some parameters are known. These parameters are  $k_h$  the hysteresis losses coefficient,  $k_e$  the excess loss coefficient, the conductivity  $\sigma$ , the stacking factor  $k_f$ , and the lamination thickness  $l$ . These parameters are combined into

equation (8.4) from [48],[49] to determine the iron losses of a certain material. Coefficients  $k_h$  and  $k_e$  can be obtained from the data sheet of the magnetic steel lamination.

$$\frac{1}{T} \int_0^T dP_{\text{tot}}(t)dt = k_h B_m^2 f k_f + \int_0^T \left[ \sigma \frac{\lambda^2}{12} \left( \frac{dB}{dt}(t) \right) + k_e \left( \frac{dB}{dt}(t) \right)^{3/2} \right] k_f dt \quad (8.4)$$

Using a time stepping FE simulation over one electric period for each speed of the 4QT gives the speed dependent iron losses that are shown in Figure 8.4. In this figure the inner rotor iron loss curve is obtained by rotating the inner rotor, and the Stator iron loss curve is obtained by rotating the inner and outer rotors synchronously in the FE simulation program.

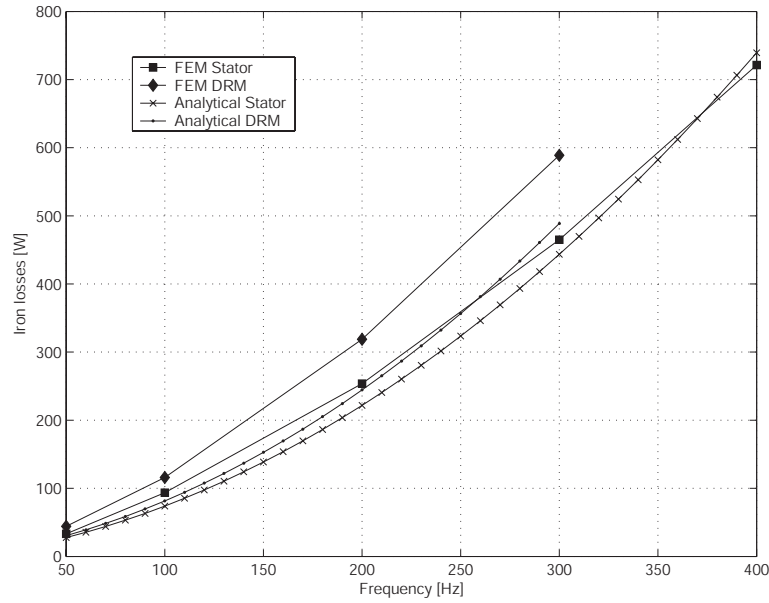


Fig. 8.4 FE simulated of the Stator and of the DRM iron losses versus electrical frequency compared to analytical values.

Figure 8.4 shows the iron losses for the Stator and the DRM both FE simulated and analytically calculated. The FE and analytical iron losses for the Stator machine show good agreement, while for the DRM the FE simulated values are slightly higher than the analytical values.

### 8.3 Mechanical losses

The mechanical losses are the mechanical friction losses, mostly in the bearings, and the air friction losses due to the two cooling fans integrated in the outer rotor, and the windage losses of the rotors.

In a PM machine the mechanical friction losses are difficult to measure due to the influence of cogging and the iron losses from the magnetic flux of the permanent magnets, which are present at no-load. To measure the friction losses a rotor without magnets can be manufactured and used for friction measurements. This has however not been done for the 4QT prototype. The friction losses can be predicted analytically with equation (8.5) and equation (8.6) from [41]:

$$T_0 = 10^{-7} f_0 (vn)^{2/3} d_m^3 \quad (8.5)$$

where  $T_0$  is a friction torque independent of the bearing load and which is the dominating friction torque at low loads,  $f_0$  is a factor dependent on the bearing type and the lubrication method,  $v$  is the kinematic viscosity of the lubricant,  $n$  the rotational speed and  $d_m$  the mean diameter of the bearing:

$$T_1 = f_1 P_1^a d_m^b \quad (8.6)$$

where  $T_1$  is a bearing load dependent friction torque,  $f_1$  is a factor dependent of the bearing type and load,  $P_1$  the bearing load force and  $a$  and  $b$  exponents dependent of the bearing type. In the case of no-load tests of the Stator with the inner and outer rotors rotating at the same speed,  $P_1$  is made up of only the gravitation force from the inner and outer rotor, neglecting any magnetic forces caused by rotor eccentricities. Solving these equations for no-load of the Stator with the inner and outer rotor rotating at the same speed gives the friction torque as in Figure 8.5.

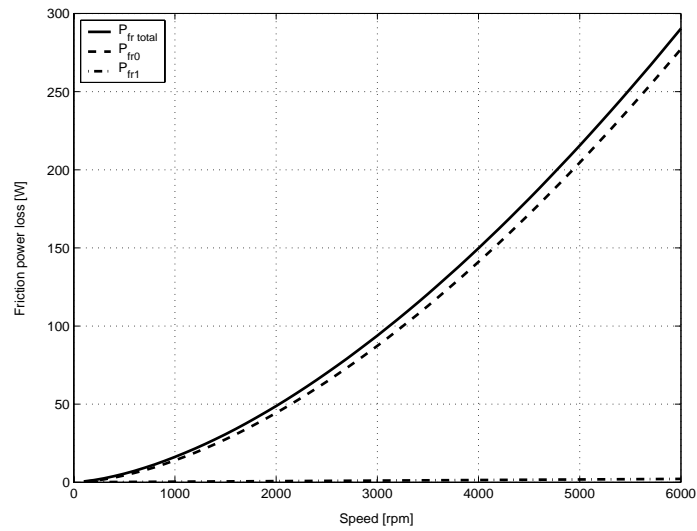


Fig. 8.5 Calculated bearing friction losses of the Stator.

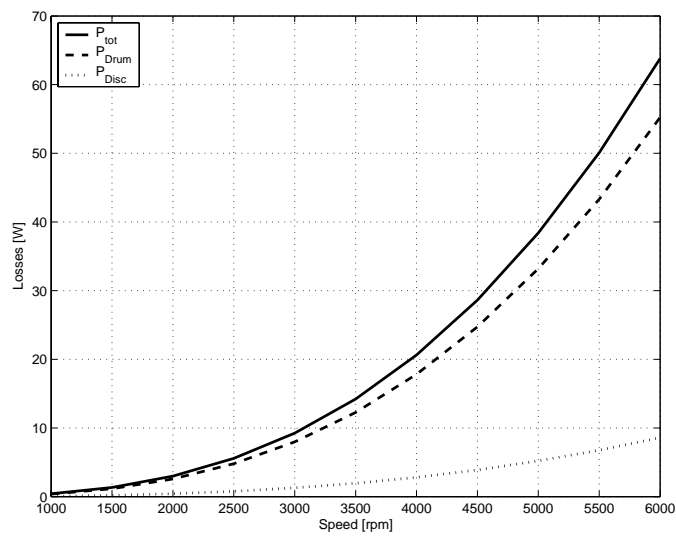


Fig. 8.6 Calculated windage losses of the outer rotor from [36].

The windage loss of the outer rotor of the 4QT can be estimated as the windage losses [36] of a drum of the same size as the 4QT rotor. The windage losses of



the outer rotor of the 4QT are shown in Figure 8.6. As can be seen from this figure the windage losses are small compared to the other losses at these low speeds. At twice the speed, i.e. 12000rpm, the total windage losses are 440 W. At such high speeds, these losses can no longer be neglected.

For the 4QT prototype there are two internal fans that will increase the windage losses, which means that the windage losses in Figure 8.6 are an underestimation.

The calculated windage loss is for a drum of the same size as the outer rotor, this is an ideal case since the geometry of the outer rotor when rotating synchronously with the inner rotor is in fact not an ideal drum but consists of a complex geometry with two fans and air holes as shown in Figure 8.7 below.

The windage losses of the inner rotor will be even smaller than of the outer rotor due to the lower rotational speed, the smaller radius and the shorter axial length. Performing windage calculations of the inner rotor using the same method as for the outer rotor gives windage losses at 3000rpm which are less than 3 W, these have no significant impact on the efficiency calculation for the machine.



Fig. 8.7 A detailed layout of the two rotors of the 4QT prototype.

## 8.4 Stray losses

The stray losses are in short the remaining losses of the total losses when subtracting the copper, iron, friction and windage losses. According to IEEE Std 112 [43] the stray losses are defined as shown in equation (8.7) and equation (8.8).

$$P_{\text{stray}} = \underbrace{(P_{\text{input}} - P_{\text{output}})}_{\text{Total losses}} - P_{\text{conventional}} \quad (8.7)$$

$$P_{\text{conventional}} = P_{\text{Copper}} + P_{\text{Iron}} + P_{\text{Mechanical}} \quad (8.8)$$

The stray losses are losses caused by leakage flux and/or by space harmonic flux components [13]. According to [44] stray losses are made up of losses in the stator teeth and yoke iron due to the axial fringing flux, losses in the frame and other structural parts caused by leakage flux and losses from constructional sources such as core piling, core segment joints, rotor eccentricity and other manufacturing variations.

For the 4QT prototype the stray losses will be defined as described by IEEE Std 112 [43].

## 8.5 Circulating currents in the windings

To avoid circulating currents between the strands of the winding in an electric machine the winding is usually transposed. This reduces the difference in induced voltage between the parallel strands of the winding. This voltage has its origin from magnetic flux that is linked with the different strands. Using deep narrow slots in the machine such as these used in the DRM of the 4QT, the leakage flux across the slots will make the amount of flux linked with the strands different for strands placed at different depths in the slot.

FE analysis was carried out using the geometry shown below in Figure 8.8 assuming different placement of the conductors and strands in the two slots containing each side of the coil.

- Case 1: Straight connections between conductors and strands in the slots
- Case 2: Straight connections of the conductors but transposed strands
- Case 3: Crossed connections of conductors but straight connection of strands
- Case 4: Crossed connections of conductors and transposed strands

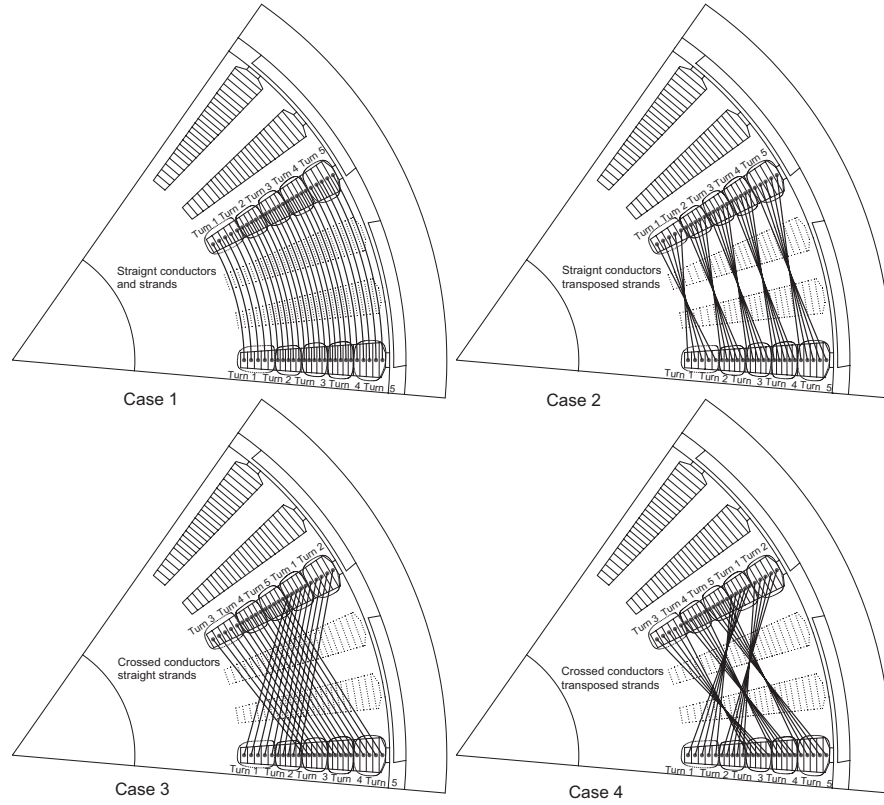


Fig. 8.8 Connections for the FE simulation of circulating currents in the inner rotor winding.

As seen in the figure, each slot is divided into 25 different regions, each region represents a strand in the winding and 5 regions representing one turn. The real inner rotor has 25 strands in each turn but to reduce the size and complexity of the problem only 5 strands were used to simulate each turn. All regions representing strands are connected to a coil conductor<sup>1</sup> that is placed in the circuit shown in Figure 8.9 containing a circuit layout of the whole inner rotor winding. The circuit contains a total of 150 coil conductors and two resistances R1 and R2 that are small resistances used to investigate the current between the phases.

During the FE analysis the inner rotor is rotated at the desired speed thus inducing voltage in each strand/region. The voltage in each coil conductor in the cir-

1. Function used in Flux 2D for coupling between a geometry and an external circuit.

cuit will depend on the position of the strand/region in the slot. By connecting the strands in different ways as in Figure 8.8 different currents will be produced by the difference in induced voltage of the different strands.

It is then possible to calculate the losses in each coil conductor and by adding them together it is possible to calculate the total losses in the machine with different connections and to see how the winding method influences on the losses caused by circulating currents.

The circulating currents induced in the strands placed at different positions in the radial direction are shown in Figure 8.10. It is clearly seen that the currents are drastically reduced when transposing the strands inside each turn while the crossed connections between the turns have no significant effect.

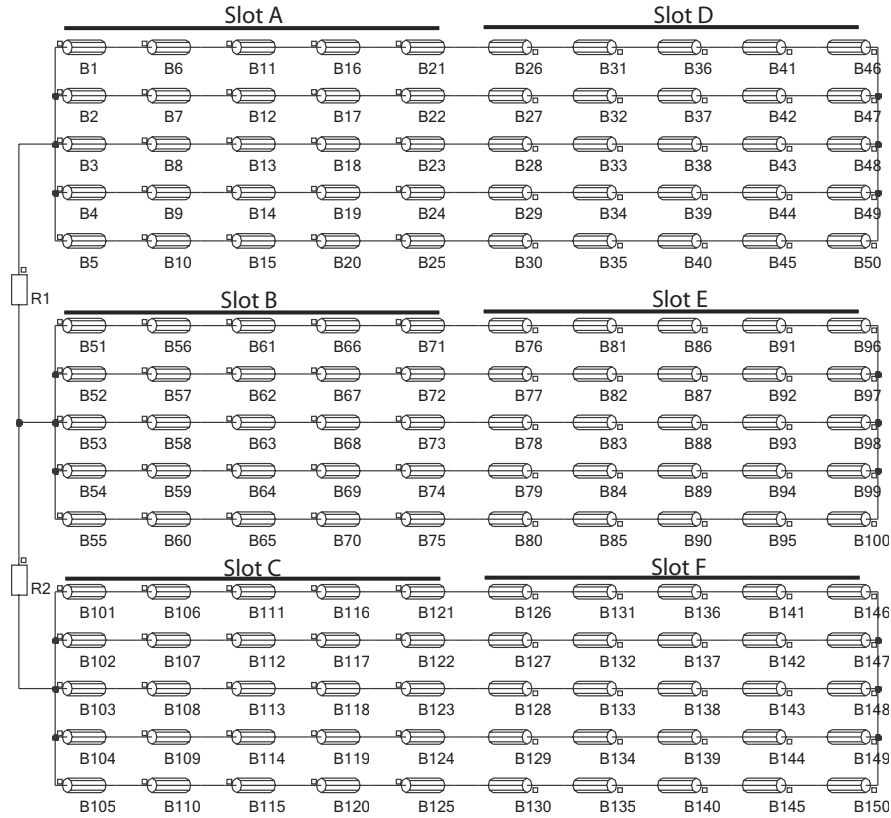


Fig. 8.9 Circuit used for the FE analysis of circulating currents in the 4QT.

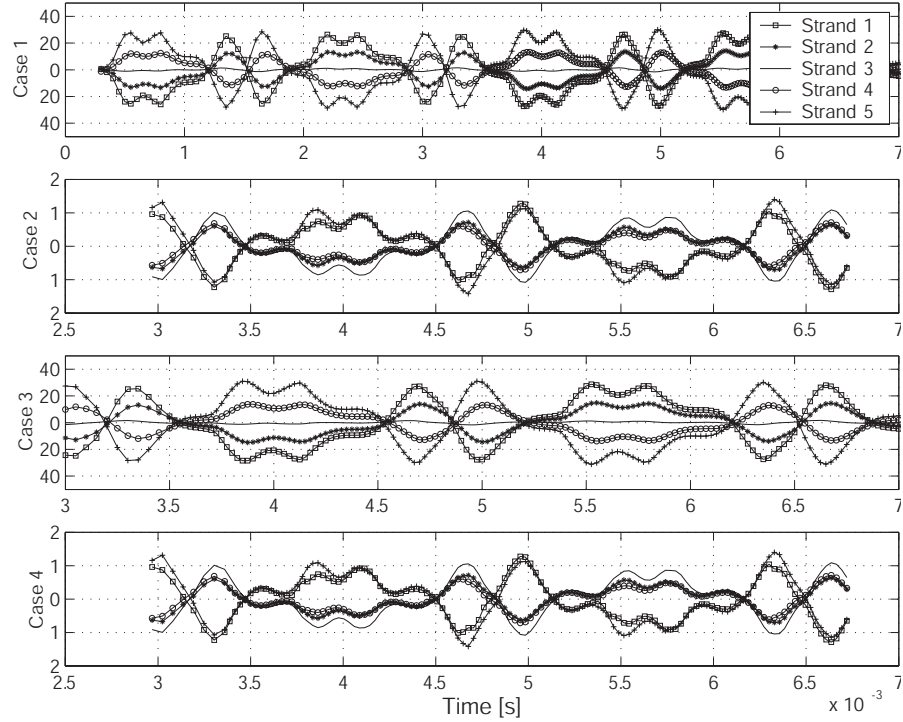


Fig. 8.10 Circulating current [A] in the phases for each of the four cases described earlier. The currents are separated in the five different strands in one turn.

The power losses due to these currents are shown in Figure 8.11. The losses show the same behaviour as the currents. As can be seen when comparing the mean power losses for case 2 and case 4 in Figure 8.11, the difference is almost zero while the difference between cases 1 and 2 and cases 3 and 4 are significant. This indicates that the significant parameter for the reduction of the circulating currents is the transposition of the strands inside each turn. The mean power for cases 2 and 4 is 564 W which is a relatively high value and could be dependent on the 5 times larger area used for each strand as can be seen in Figure 8.8. To minimize this error each strand has to be modelled, which means modelling 125 strands in each slot which gives a total of  $125 \cdot 6 = 750$  coil conductors in the geometry in Figure 8.9. To make this simulation possible it is necessary to reduce the size of the problem. This simulation will of course give more accurate results, but the most important conclusion from the simulation which is the significant decrease in losses when transposing the strands can be derived from the simplified model using 25 strands per slot. The above results indicate the importance of correctly transposition of the strands when the windings are placed in

deep slots. This result could be used for all PM machines and could be one of the sources of a unwanted constant braking torque at no-load which was observed on the 4QT prototype after it was repaired.

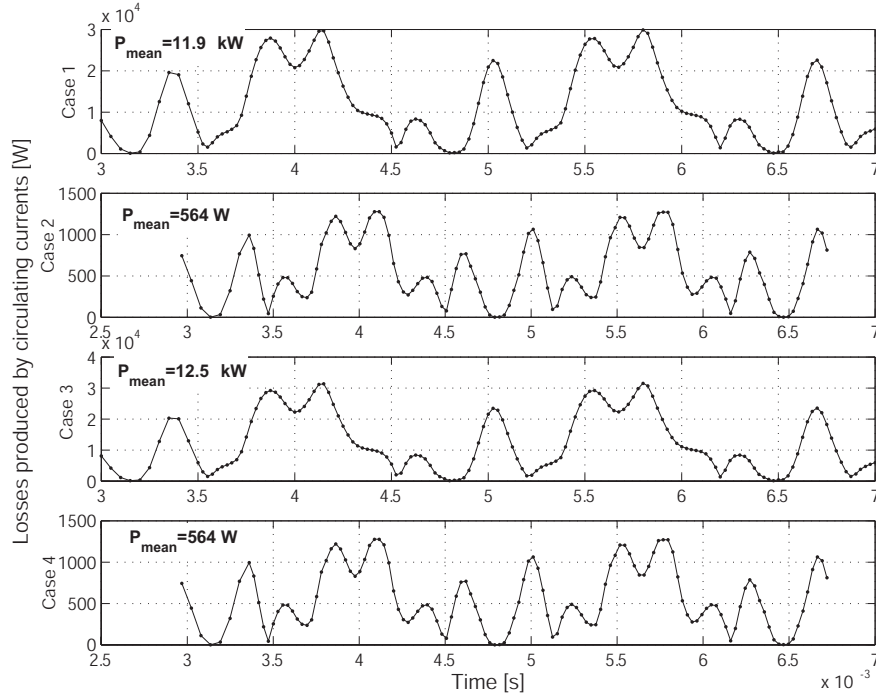


Fig. 8.11 Power losses due to circulating currents in the different strands.

## 8.6 Measured and calculated losses

The losses have been separated into copper, iron, mechanical and stray losses. The mechanical losses are the friction and the windage losses combined. Copper, iron, and mechanical losses have been calculated while the total losses have been measured using the calorimetric method. The difference between the measured and the calculated losses is defined as stray losses. This has been done both at no-load and load conditions operating the 4QT Stator as a generator.

### 8.6.1 No Load

The losses has been measured calorimetrically to 995 W at 4000rpm when rotating the outer and inner rotor synchronously. At no-load there are no resistive

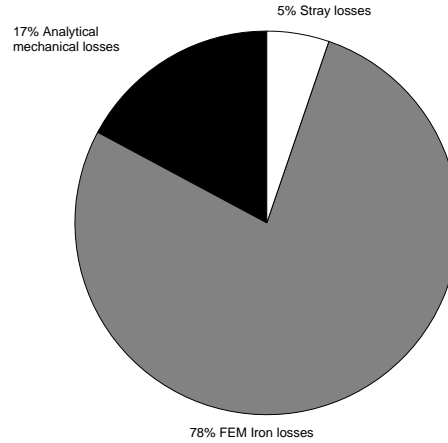


*Fig. 8.12 Losses at no-load operation, 4000 rpm. Both rotors rotating synchronously.*

losses since no current is applied to the windings in the generator mode of operation. The existing losses, which are iron losses, mechanical losses and stray losses have been separated in Figure 8.12.

At no-load operation the dominating losses are the iron losses, while the mechanical and stray losses are low in comparison.

### 8.6.2 Load

During almost nominal load at 4000 rpm, 66.75 Nm, with a load current of 112.6 A and a three phase output power of 26600 W, the total measured calorimetric losses of the 4QT prototype machine was 1872 W. Using theoretical values for the copper, iron, and the mechanical losses for this operating point gives a loss distribution as shown in Figure 8.13.

As seen in Figure 8.13 the dominating losses at nominal load are the stray losses which are 38% of the total losses or 2.7% of the output power. For an induction motor with ratings 1-90 kW the stray losses are approximately 1.8% of the rated load [43]. The stray losses are high in the 4QT Stator at load, the complex geometry of the machine is one of the explanations. The end windings of the 4QT Stator, are situated between the aluminium heat sink and the solid steel outer rotor, Figure 8.14, induces stray losses both in the heat sink and in the outer rotor. In a conventional machine the rotor have the same axial length as the stator, thus the magnetic flux from the end windings will not interact with any extended outer rotor causing losses.

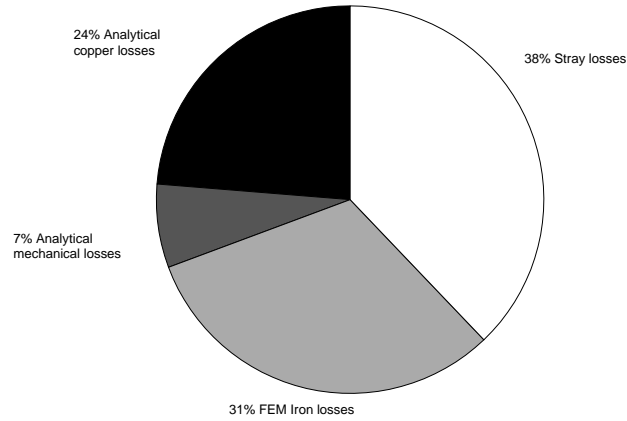


*Fig. 8.13 Load loss distribution, nominal load at 4000 rpm.*

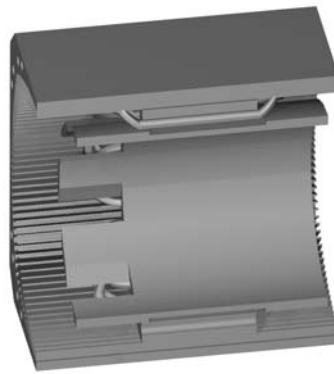


*Fig. 8.14 Stator end winding placement between housing heat sink and outer rotor.*

## **8.7 Conclusions**

The different losses in the 4QT have been calculated analytically and with FE methods. The losses have been separated into different loss components and show high stray losses at load for the 4QT machine.

An investigation about the impact on the losses from circulating currents in the inner rotor windings due to winding method has been performed. The results indicate the importance of correctly transposing the strands when the windings are placed in deep slots.



## 9 Conclusion and future work

### 9.1 Conclusions

This thesis describes the novel 4QT (Four-Quadrant Transducer) system with its advantages and disadvantages. The main purpose of the system is to decrease the fuel consumption and emissions of road vehicles. The 4QT system has been simulated for a 12-ton vehicle using the FTP75 drive cycle and the results show a decrease of fuel consumption of about 30%. At constant speed operation there is no significant difference in the fuel consumption. Figure 9.1 shows the fuel consumption for the 12-ton vehicle both with and without a 4QT hybrid system for two different auxiliary loads. The lower power is for the electrical load of a vehicle and the higher load is for a truck equipped with a freezer.

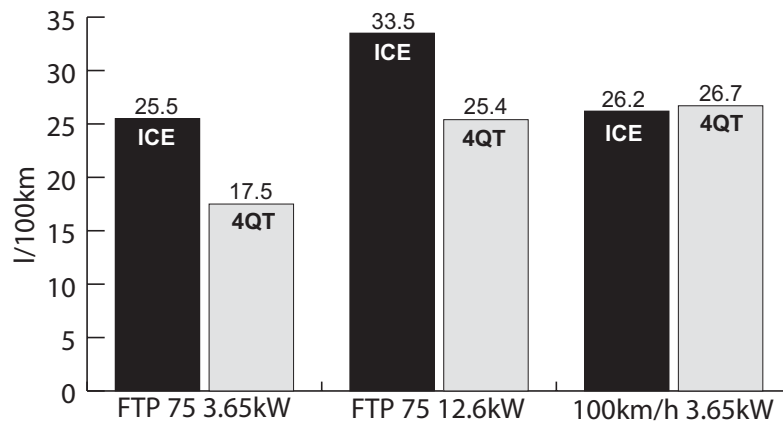


Fig. 9.1 Comparison of the fuel consumption for hybrid (4QT) and conventional 12-ton vehicles.

A 4QT system is also dimensioned for a 12-ton vehicle, both for one equipped with a gearbox and one with only a constant gear. The use of a gearbox gives a smaller Stator but it does not significantly affect the size of the DRM since it is mostly dependent on the ICE torque output.

A prototype of a radial-radial flux 4QT transducer has been designed and manufactured. The prototype is scaled to fit the testing facilities at the electric machines laboratory at KTH. The 4QT is divided into two different machines; the DRM with rated torque and base speed equal to 100Nm and 3000rpm respective-

ly, and the Stator with rated torque and base speed equal to 70Nm and 4000rpm respectively. The prototype is presented together with some initial measurements which show good agreement with the designed values.

In the machine design FEM has been used both for the electromagnetic and thermal calculations. The thermal FEM show that the hot-spot in the machine is in the bottom of the inner rotor slots. The electromagnetic values such as the back-EMF show good agreement with the measured values. The 4QT Stator is thermally easy to cool via the water cooling system, while the DRM has shown to be more difficult to cool so a forced air cooling system has been introduced to make the cooling of the inner rotor more efficient.

## **9.2 Future work**

### **9.2.1 Drive system simulation of the 4QT system**

A special test bench has been developed for the 4QT system [20],[21] and it should be used to test the complete 4QT system in different driving and fault situations. Preferably the 4QT prototype should replace the two machine now acting as DRM and Stator in Figure 9.2.

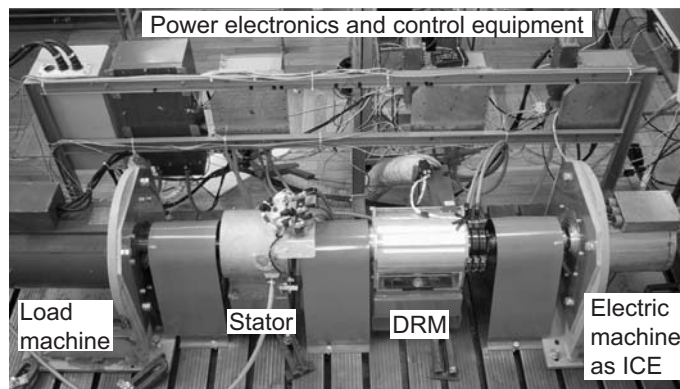


*Fig. 9.2 4QT system test bench.*

### **9.2.2 The slipring-less double rotor machine**

During a visit to the technical museum in Munich, a cut-up of a brush less car alternator gave an idea on how to make a double rotor machine without sliprings for the 4QT application.

The machine should be a 3-phase claw pole machine with two air gaps as in Figure 9.3. The machine has coils as shown in Figure 9.4. These coils produce a magnetic flux that propagates axially through the centre core up the laminated side parts and then across the first airgap into the claw foot. Thereafter the magnetic flux crosses the next airgap from the top of the claw into one magnet and then circumferentially through the outer rotor back to the next magnet and once again across the outer airgap into the next claw and back through the claw foot across the inner airgap and into the next side part. The flux has now travelled around a closed loop linking the winding and the active parts of the machine. Combining three phases in the axial direction as shown in Figure 9.5 with a 120 electrical degree phase shift in space between them a three phase machine can be realised that will produce a three phase travelling flux wave in the outer air gap. If the claws are connected to the input shaft the rotating magnetic field will rotate relative to the speed of the claws. In this way it is possible to change the speed between the inner and outer rotor which is the main function of the double rotor machine.

A complete 4QT system without sliprings can be realised by adding magnets on the outer side of the outer rotor and a Stator for additional torque production.

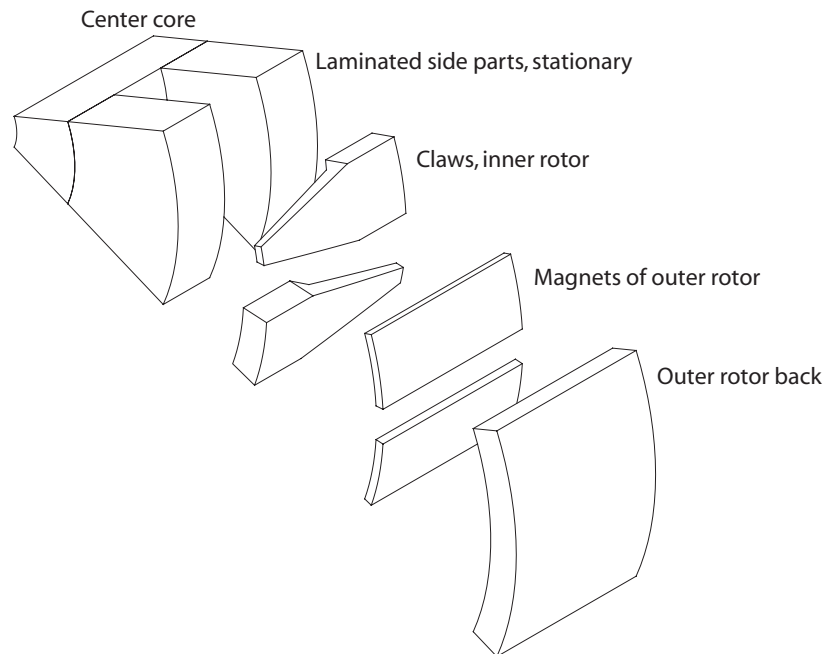
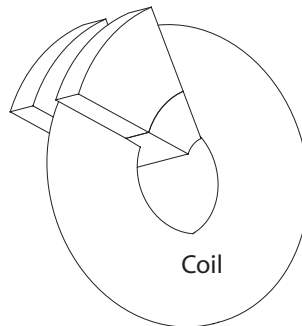
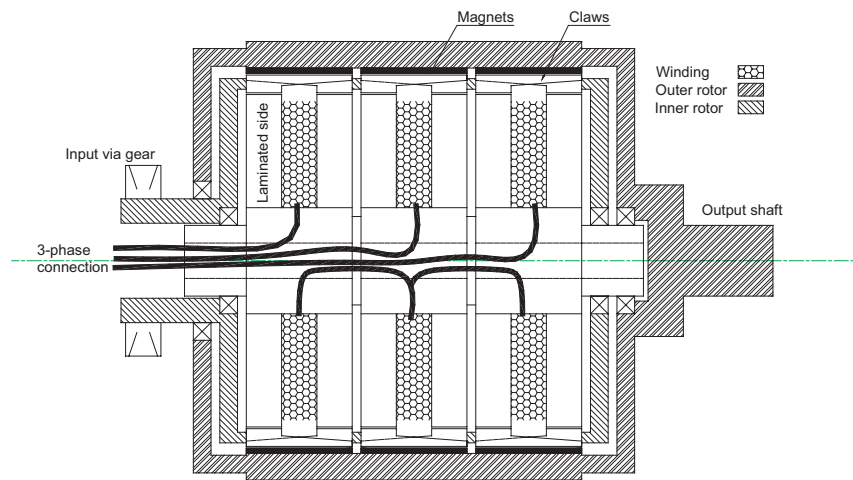


Fig. 9.3 Exploded view of a 45 degrees section of one phase of the slipring-less double rotor claw pole machine.



*Fig. 9.4 Coil placement of the slipring-less double rotor claw pole machine.*



*Fig. 9.5 Axial view of the double rotor claw pole machine.*

As shown in Figure 9.5 the coils are connected to the voltage source through a hollow shaft. To access the connections a side displacement of the input shaft is necessary.

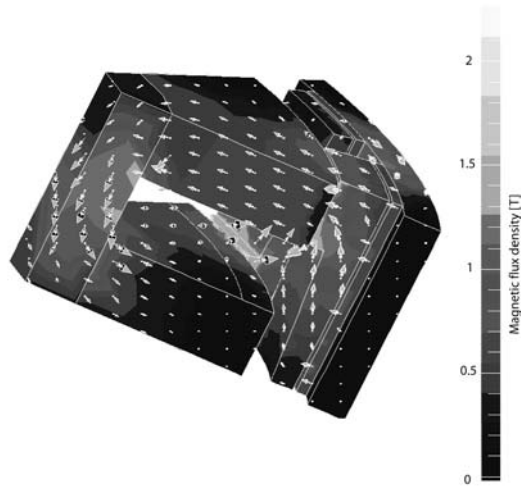


Fig. 9.6 Flux density and direction of the flux for a 45 degree piece of one phase of the slipring-less double rotor claw pole machine.

Preliminary calculations to see if it is possible to build a machine with this configuration has been done by 3D time stepped FEM<sup>1</sup>. The geometry is shown in Figure 9.6, and the results show that the concept are interesting for further work.

Since sliprings in the 4QT system are a part that need maintenance it is desirable to construct a 4QT system without them. This section of the thesis shows that it could be possible to do so. Even though much more work is needed on such a double rotor claw pole machine it has been shown that this design could be interesting for future work on the 4QT system.

---

1. Flux 3D, Cedrat



---

## References

- [1] Robert Bosch GmbH, “Avgasteknik för ottomotorer” Technical information.
- [2] Robert Bosch GmbH, “Automotive Handbook” 4th edition, October 1996.
- [3] T. Bäckström, “Integrated Energy Transducer Drive for Hybrid Electric Vehicles”, Doctor’s thesis, Royal Institute of Technology, Stockholm, June 2000, ISBN 91-7170-571-6, ISSN 1404-8248.
- [4] J. Kümpers, “Lithium Ion Batteries for Hybrid Vehicles and New Vehicle Power Supply Systems”, Presented at EVS18, Berlin, 2001.
- [5] T. Matsumoto, N. Watanabe, H. Suguira, T. Ishikawa, “Development of a Fuel-Cell Hybrid Vehicle”, Toyota motor corporation, Japan, Presented at EVS18, Berlin, 2001.
- [6] Patent. PAT NR: 9804261-7 “Energy converter with double rotors and double windings”.
- [7] Orchard T.M. Smokers, Serve Ploumen, Mario Conte, Leo Buning and Carl Meier-Engel, “Test methods for evaluating energy consumption and emissions of vehicles with electric, hybrid and fuel cell power trains”, October 2000.
- [8] N. Takeda, Y. Horii, N. Kumagai, A. Motooka, Y. Susuki, “Lithium-ion Batteries for Heavy Duty Hybrid Vehicles”, Mitsubishi motor corporation (MMC), Japan, Presented at EVS18, Berlin, 2001.
- [9] P. Thelin, J. Soulard, H.-P. Nee, and C. Sadarangani, “Comparison Between Different Ways to Calculate the Induced No-load Voltage of PM Synchronous Motors using Finite Element Methods”, *4th International Conference on Power Electronics & Drive System, 2001, PEDS’01*, Bali, Indonesia.
- [10] E. Wennerström, “Fordonsteknik” 8:e Uppl 1999, Course compendium Ground Vehicle Engineering, Basic Course, KTH., Stockholm, Sweden
- [11] A. Brooks, T. Gage, “Integration of Electric Drive Vehicles with the Electric Power Grid -- a New Value Stream”, Presented at EVS18, Berlin, 2001.
- [12] “Brushless Permanent Magnet Motor Tutorial”, Flux 2D version 7.5, Cedrat, Mars 2001.
- [13] O. Aglén, “Calorimetric Measurements of Losses in Induction Motors” Licentiate thesis, Royal Institute of Technology, Stockholm, 1995, ISSN 1100-1631.
- [14] E. Nordlund and C. Sadarangani, “Four-Quadrant Energy transducer”, Published in the Proceedings of the 37th Industrial Application Society Meeting, IAS 2002, Pittsburgh, USA, October 2002
- [15] C. Sadarangani, “Electrical Machines -Design and Analysis of Induction and Permanent Magnet Motors”, Royal Institute of Technology, 2000, ISBN 91-7170-627-5, ISSN 1404-8248.

- 
- [16] N. Bianchi, S. Bologani, and B. Chalmers, "Salient-Rotor Synchronous Motors for an Extended Flux-Weakening Operation Range", *IEEE Transactions on Industry Applications*, Vol. 36, No. 4, July/August 2000.
  - [17] N. Bianchi, S. Bologani, "Parameters and Volt-Ampere Ratings of a Synchronous Motor Drive for Flux-Weakening Applications", *IEEE Transactions on Power Electronics*, Vol. 12, No 5, September 1997.
  - [18] L. Maquet "Internal report on the dimension of a 4QT system for a medium sized car". Royal Institute of Technology, Stockholm, Sweden
  - [19] K. Thoreborg, "Power Electronics -in Theory and Practice", 1993, Studentlitteratur, Lund, ISBN 91-44-38091-7.
  - [20] S. Châtelet, C. Sadarangani, "Four-Quadrant Transducer Test Bench", Presented at EVS-19, Busan, Korea 2002
  - [21] S. Châtelet, C. Sadarangani, "Test Bench for Electromagnetic Energy Transducers in Hybrid Vehicles ", Presented at NORpie, Stockholm, Sweden 2002.
  - [22] Alan J. Chapman, Fundamentals of Heat Transfer, ISBN 0-02-321600-x.
  - [23] Nordlund E. "Simulation and Design of a Radial-Radial Four-Quadrant Transducer for Hybrid Vehicles", licentiate thesis presented in Feb 2003 at Royal institute of Technology, KTH, Stockholm.
  - [24] Data supplied by Volvo.
  - [25] F. Magnussen, E. Nordlund, S. Châtelet, C. Sadarangani, "Measurements on Slip Ring Units for Characterization of Performance", Presented at 6th International Power Engineering Conference (IPEC), Singapore, 27-29 November 2003.
  - [26] E. Nordlund, F. Magnussen, G. Bassilious, P. Thelin, "Testing of Silver-, Copper-, and Electro-Graphite Brush Materials for Slip Ring Units", Presented at Nordic Workshop on Power and Industrial Electronics (NORpie), Trondheim, Norway, 14-16 June 2004.
  - [27] T. Ishikawa, G. R. Slemon, "A method of reducing Ripple Torque in Permanent Magnet Motors without Skewing", *IEEE Transaction on Magnetics*, Vol 29, NO 2, March 1993.
  - [28] M. S. Islam, S. Mir, T. Sebastian, "Issues in Reducing the Cogging Torque of Mass-Produced Permanent-Magnet Brushless DC Motor", *IEEE Transactions on Industry Applications*, Vol 40, No 3 May/June 2004.
  - [29] N. Bianchi, S. Bolognani, "Design Techniques for reducing the Cogging Torque in Surface-Mounted PM Motors", *IEEE Transactions on Industry Applications*, Vol 38, No 5 September/October 2002.
  - [30] J. F. Gieras, "Analytical Approach to Cogging Torque Calculation of PM Brushless Motors", *IEEE Transactions on Industry Applications*, Vol 40, No 5 September/October 2004.
-



- 
- [31] Functional Requirements for Retarder Performance for City Buses, Volvo, Sweden.
  - [32] D. Stanton, A. Boglietti, A. Cavagnino, "Solving the More Difficult Aspects of Electrical Motor Thermal Analysis"
  - [33] B. Palm, "Short Notes on Heat Transfer", Course material for Cooling of Electronics, Course at KTH (Royal Institute of Technology) in Stockholm Sweden
  - [34] P. Zheng, P. Thelin, E. Nordlund, S. Eriksson, C. Sadarangani, "Consideration of Skewed Slots in the Performance Calculation of a Four-Quadrant Transducer", IEEE Vehicular Power and Propulsion Symposium, VPP 04, Paris, France, 6-8 October 2004.
  - [35] P. Zheng, P. Thelin, A. Chen, E. Nordlund "Measurements and Calculations of Inductances of a 4QT Hybrid Electric Vehicle Prototype Machine", IEEE Vehicular Power and Propulsion Symposium, VPP 04, Paris, France, 6-8 October 2004.
  - [36] K. R. Pullen. "Spread sheet on windage losses".
  - [37] Yokogawa, "User's Manual WT1030/WT1030M", IM253620-01E, 3rd Edition.
  - [38] Prova instruments INC, "DC/AC Current Probe CM-05 Users Manual".
  - [39] Swissflow, Company homepage: "<http://www.swissflow.com>"
  - [40] J. Timmerman, "Resistance measurements and Insulation test of the 4QT prototype, June 2004.
  - [41] SKF Huvudkatalog, SKF Sverige AB, 1997.
  - [42] M. J. Hoeijmakers, M. Rondel, "The Electrical Variable Transmission in a city bus", 35th Annual IEEE Power Electronics Specialists Conference, Aachen, Germany, 2004.
  - [43] IEEE Std 112<sup>TM</sup>-2004, "IEEE Standard Test Procedure for Polyphase Induction Motors and Generators"
  - [44] H.C. Karmaker, "Stray Losses in Large Synchronous Machines", IEEE Transactions on Energy Conversion, Vol 7, No 1, March 1992.
  - [45] N. Urasaki, T. Senjyu, K. Uezato, "An Accurate Modelling for Permanent Magnet Synchronous Motor Drives", APEC, 2000.
  - [46] Vacuumschmelze, "Rare-Earth Permanent Magnets Vacodym Vacomax", Edition 2000, Permanent magnets manufacturer catalogue
  - [47] W. M. Arshad, "A Low-Leakage Linear Transverse-Flux Machine for a Free-Piston Generator" ISBN 91-7283-535-4, Doctoral Thesis, KTH 2003.
  - [48] F. Fiorillo, A. Novikov, "An Improved Approach to Power Losses in Magnetic Laminations under Nonsinusoidal Induction Waveform, IEEE Transactions on magnetics, Vol 26, NO 5, September 1990.
-

- 
- [49] Flux 2D, Version 8.1, Finite Element Software, Cedrat, France.
- [50] E. Nordlund, S. Tsakok, “Lumped Circuit Model of an Axial Flux Motor”, Published in the Proceedings of the 21st Worldwide Battery, Hybrid and Fuel Cell Electric Vehicle Symposium & Exhibition, EVS-21, Monaco, 2-6 April, 2005.

## List of symbols and abbreviations

### List of symbols

A	Area	[m <sup>2</sup> ]
b	Slot width	[m]
B <sub>δ</sub>	Airgap flux density	[T]
B <sub>m</sub>	Maximum flux density in airgap over magnet	[T]
c <sub>f</sub>	Carter factor	[-]
C <sub>p</sub>	Specific heat coefficient	[J/kgK]
d <sub>m</sub>	Mean diameter	[m]
D	Diameter	[m]
f	Frequency	[Hz]
I <sub>ph</sub>	Phase current (RMS)	[A]
I <sub>x</sub>	Current (x= a,b,c dependent of phase)	[A]
i <sub>x</sub>	Current (x= d or q-axis)	[A]
L	Length	[m]
L <sub>x</sub>	Inductance (x= q or d-axis)	[H]
L <sub>ys</sub>	Length of end winding	[m]
k <sub>skew</sub>	Skewing factor	[-]
$\dot{m}$	Mass flow	[kg/s]
n	Rotational speed	[rpm]
N <sub>s</sub>	Number of conductors	[-]
P	Power	[W]
P <sub>Cu</sub>	Copper losses	[W]
P <sub>Fe</sub>	Iron losses	[W]
P <sub>in</sub>	Input power	[W]
P <sub>out</sub>	Output power	[W]
P <sub>stray</sub>	Stray losses	[W]
q	Number of slots per pole per phase	[-]
$\dot{q}$	Power	[W]
q <sub>i</sub>	Power source number i	[W]
Q <sub>r</sub>	Number of slots	[-]
R <sub>th</sub>	Thermal resistance	[K/W]
S	Current Density	[A/m <sup>2</sup> ]
t <sub>LMTD</sub>	Logarithmic mean temperature difference	[°C]

$t_i$	Temperature of node number i	[°C]
$t_{in}$	Inlet temperature	[°C]
$t_m$	Magnet thickness	[m]
$t_{out}$	Outlet temperature	[°C]
$\Delta T$	Temperature Difference	[°C]
$U_x$	Voltage (x= a,b,c dependent of phase)	[V]
$u$	Voltage	[V]
$U_{ll}$	Line-line voltage (RMS)	[V]
$\alpha$	Half a magnet pole angle	[rad]
$\delta$	Airgap length	[m]
$\delta_e$	Equivalent airgap length	[m]
$\eta$	Efficiency	[-]
$\lambda_c$	Thermal conductivity	[W/mK]
$\lambda_m$	PM flux linkage	[Vs]
$\mu_r$	Relative permeability	[-]
$\nu$	Kinematic viscosity	[m <sup>2</sup> /s]
$\tau_s$	Slot pitch	[m]
$\Psi_x$	Flux linkage (x= d or q-axis)	[Vs]
$\omega$	Angular speed	[rad/s]

### Abbreviations

2D	Two Dimensions	HEV	Hybrid Electric Vehicle
3D	Three Dimensions	ICE	Internal Combustion Engine
4QT	Four Quadrant Transducer	IET	Integrated Energy Transducer
CVT	Continuous Variable Transmission	ISG	Integrated Starter Generator
DC	Direct Current	LMTD	Logarithmic Mean Temperature Difference
DRM	Double Rotor Machine	OOL	Optimal Operation Line
EMF	Electro Motive Force	RMS	Root Mean Square
EV	Electric Vehicle	SOC	State Of Charge
FC	Fuel Cell		
FE	Finite Element		
FEM	Finite Element Method		
FTP	Federal Test Procedure		
GPB	General Purpose Interface Bus		

---

## Index

### **A**

Air gap flux density 56

### **B**

Back EMF 58

Bandage 69

### **C**

Calorimetric measurements 95

Cogging 61

Cooling 71

Curb weight 29

### **D**

Drag coefficient 29

DRM test 85

### **E**

ECE15 33

Electric vehicle 13

EV 13

EV range 29

### **F**

Field weakening 67

Friction losses 90

Front area 29

FTP72 33

FTP75 33

Fuel cell 12

Fuel consumption measurement 43

### **G**

Gearbox 31

Generator test 77

Grade ability 29, 35

Gross vehicle weight 29

### **I**

IET 12

Inductance 65, 99

Integrated energy transducer 12

Integrated Starter Generator 11

---

---

Iron losses	124
ISG	11
<b><i>L</i></b>	
Lumped circuit	107
<b><i>M</i></b>	
Maximum speed	29, 36
Mean weight	29
Measurement sensors	78
Mechanical losses	127
<b><i>N</i></b>	
No load losses	89
<b><i>O</i></b>	
Optimal operation line	16
<b><i>P</i></b>	
Parallel Hybrid	10
Payload	29
Pole number	50
Prototype layout	74
Prototype parameters	99
<b><i>R</i></b>	
Resistance	100
Resistive losses	123
Retarder	27
Rolling radius	29
Rolling resistance	29
<b><i>S</i></b>	
Series hybrid	9
Slot dimensions	55
Start ability	29, 34
Stator efficiency	92
Stator test	82
Stray losses	130
<b><i>T</i></b>	
Temperature sensor placement	81
Temperature sensors	78
Thermal resistances	107

---